Lamy, F., Winckler, G., Alvarez Zarikian, C.A., and the Expedition 383 Scientists
Proceedings of the International Ocean Discovery Program Volume 383
publications.iodp.org

https://doi.org/10.14379/iodp.proc.383.105.2021

Site U1541[1]

G. Winckler, F. Lamy, C.A. Alvarez Zarikian, H.W. Arz, C. Basak, A. Brombacher, O.M. Esper, J.R. Farmer, J. Gottschalk, L.C. Herbert, S. Iwasaki, V.J. Lawson, L. Lembke-Jene, L. Lo, E. Malinverno, E. Michel, J.L. Middleton, S. Moretti, C.M. Moy, A.C. Ravelo, C.R. Riesselman, M. Saavedra-Pellitero, I. Seo, R.K. Singh, R.A. Smith, A.L. Souza, J.S. Stoner, I.M. Venancio, S. Wan, X. Zhao, and N. Foucher McColl[2]

Keywords: International Ocean Discovery Program, IODP, *JOIDES Resolution*, Expedition 383, Dynamics of the Pacific Antarctic Circumpolar Current, Site U1541, Southern Ocean, South Pacific, Chilean margin, paleoceanography, Antarctic Circumpolar Current, oceanic fronts, Circumpolar Deep Water, Antarctic Intermediate Water, marine carbon cycle, dust, biological productivity, iron fertilization, southern westerly winds, Patagonian ice sheet, West Antarctic ice sheet

Contents

Background and objectives

Site U1541 (Proposed Site CSP-1A) is located in the central South Pacific at 54°12.756′S, 125°25.540′W, ~1830 nmi west of the Strait of Magellan, at 3604 m water depth (Figure **F1A**). The site sits on the western flank of the southernmost East Pacific Rise (EPR), ~50 nmi north of the Eltanin-Tharp Fracture Zone and ~160 nmi from the modern seafloor spreading axis. Site U1541 is underlain by oceanic crust formed at the EPR between ~6 and 8 Ma (Eagles, 2006), and assuming overall constant seafloor half-spreading rates of ~4.5 cm/y (Pitman and Heirtzler, 1966), the plate tectonic backtrack path moves the site eastward. This translates to an early Pliocene position ~100 nmi closer to the crest of the EPR at a water depth several hundred meters shallower than the modern value of 3604 m. At a smaller scale, the site is located in a NNE–SSW oriented trough, ~4 nmi wide, that parallels the orientation of the EPR. The adjacent ridges rise to ~3400 m water depth southeast of the site and to ~3500 m water depth northwest of the site (Figure **F1B**).

Site U1541 is located on Multichannel Seismic (MCS) Line AWI-201000014 at the intersection with Line AWI-2010000016 (Figure **F2A**) (Gersonde, 2011). The seismic cross-lines indicate ~180 m thick sediments above oceanic basement. Sediments are mostly well stratified and have flat-lying, slightly irregular reflectors. Low to moderately reflecting layers become stronger below ~120–140 m sediment depth. Sediment echo sound (Parasound) profiles (Gersonde, 2011) reveal moderate penetration (~80 m) and distinct layering (Figure **F2B**), suggesting a succession of fine-grained soft sediments with varying lithologic composition.

A ~14 m long gravity core (PS75/059-2) that covers the past ~475 ky close to Site U1541 primarily contains calcareous ooze with some more diatom-rich intervals (~50–95 wt% $CaCO_3$, ~5–25 wt% opal, and ~5–40 wt% siliciclastics). Sedimentation rates calculated over the length of Core PS75/059-2 average ~3 cm/ky, and maxima reach ~6 cm/ky between 390 and 420 ka (Marine Isotope Stage 11) (Ullermann et al., 2016).

Site U1541 lies in the pathway of the Subantarctic Antarctic Circumpolar Current (ACC), ~100 nmi north of the modern mean position of the Subantarctic Front (SAF). In this ACC sector, the associated fronts are strongly steered by the topography of seafloor spreading systems (Udintsev and Eltanin-Tharp Fracture Zone systems).

Sea-surface temperatures (SSTs) seasonally vary between ~3°C (July–September) and ~7°C (January–March). The area is located west of the main Antarctic Intermediate and Mode Water formation regions in the Southeast Pacific. The water depth of 3604.2 m places Site U1541 within Lower Circumpolar Deep Water (LCDW) (Figure **F3**).

[1] Winckler, G., Lamy, F., Alvarez Zarikian, C.A., Arz, H.W., Basak, C., Brombacher, A., Esper, O.M., Farmer, J.R., Gottschalk, J., Herbert, L.C., Iwasaki, S., Lawson, V.J., Lembke-Jene, L., Lo, L., Malinverno, E., Michel, E., Middleton, J.L., Moretti, S., Moy, C.M., Ravelo, A.C., Riesselman, C.R., Saavedra-Pellitero, M., Seo, I., Singh, R.K., Smith, R.A., Souza, A.L., Stoner, J.S., Venancio, I.M., Wan, S., Zhao, X., and Foucher McColl, N., 2021. Site U1541. *In* Lamy, F., Winckler, G., Alvarez Zarikian, C.A., and the Expedition 383 Scientists, *Dynamics of the Pacific Antarctic Circumpolar Current*. Proceedings of the International Ocean Discovery Program, 383: College Station, TX (International Ocean Discovery Program). https://doi.org/10.14379/iodp.proc.383.105.2021

[2] **Expedition 383 Scientists' affiliations.**

MS 383-105: Published 18 July 2021

Figure F1. Oceanographic and bathymetric setting, Site U1541. A. Marine geological features and oceanic fronts. EPR = East Pacific Rise, FZ = fracture zone, SAF = Subantarctic Front, PF = Polar Front (after Orsi et al., 1995). B. Detailed bathymetry with seismic lines and shotpoints.

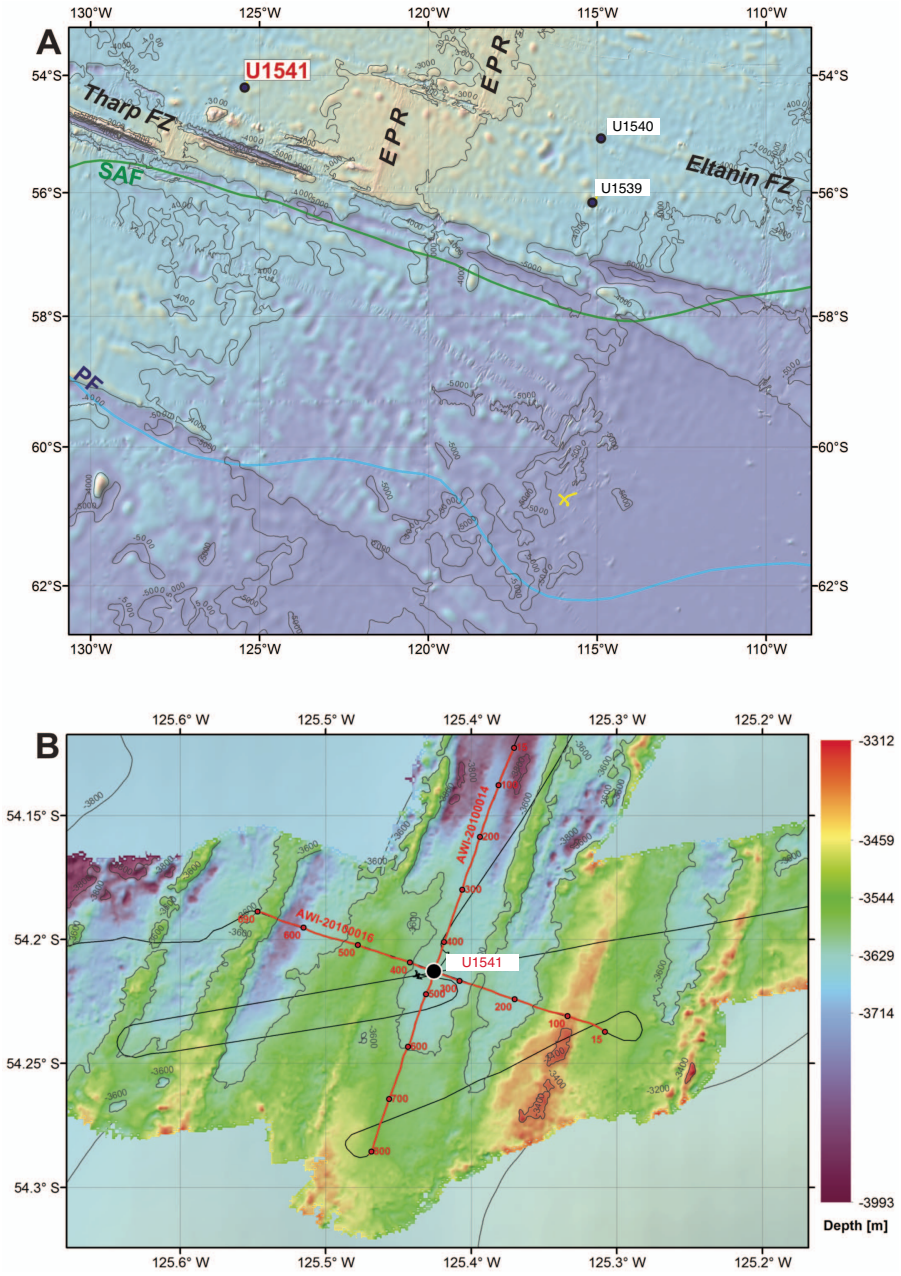

Scientific objectives

The main objectives at Site U1541 were to

- Recover a moderate resolution Subantarctic Miocene–Quaternary sediment record close to the SAF;
- Fully document the stratigraphy of calcareous and, subordinately, siliceous oozes, allowing for a wide range of paleoceanographic reconstructions;
- Reconstruct high-amplitude Subantarctic SSTs based on multiple proxies;
- Investigate long-term changes in dust input;
- Provide a record of LCDW and potential influence of glacial Antarctic Bottom Water (AABW);
- Reconstruct productivity (biogenic silica versus carbonate), nutrient distribution, and dust-productivity coupling; and
- Recover a potential far-field record of West Antarctic Ice Sheet variability.

Figure F2. (A) Multichannel seismic (MCS) and (B) Parasound profiles across Site U1541. TWT = two-way traveltime.

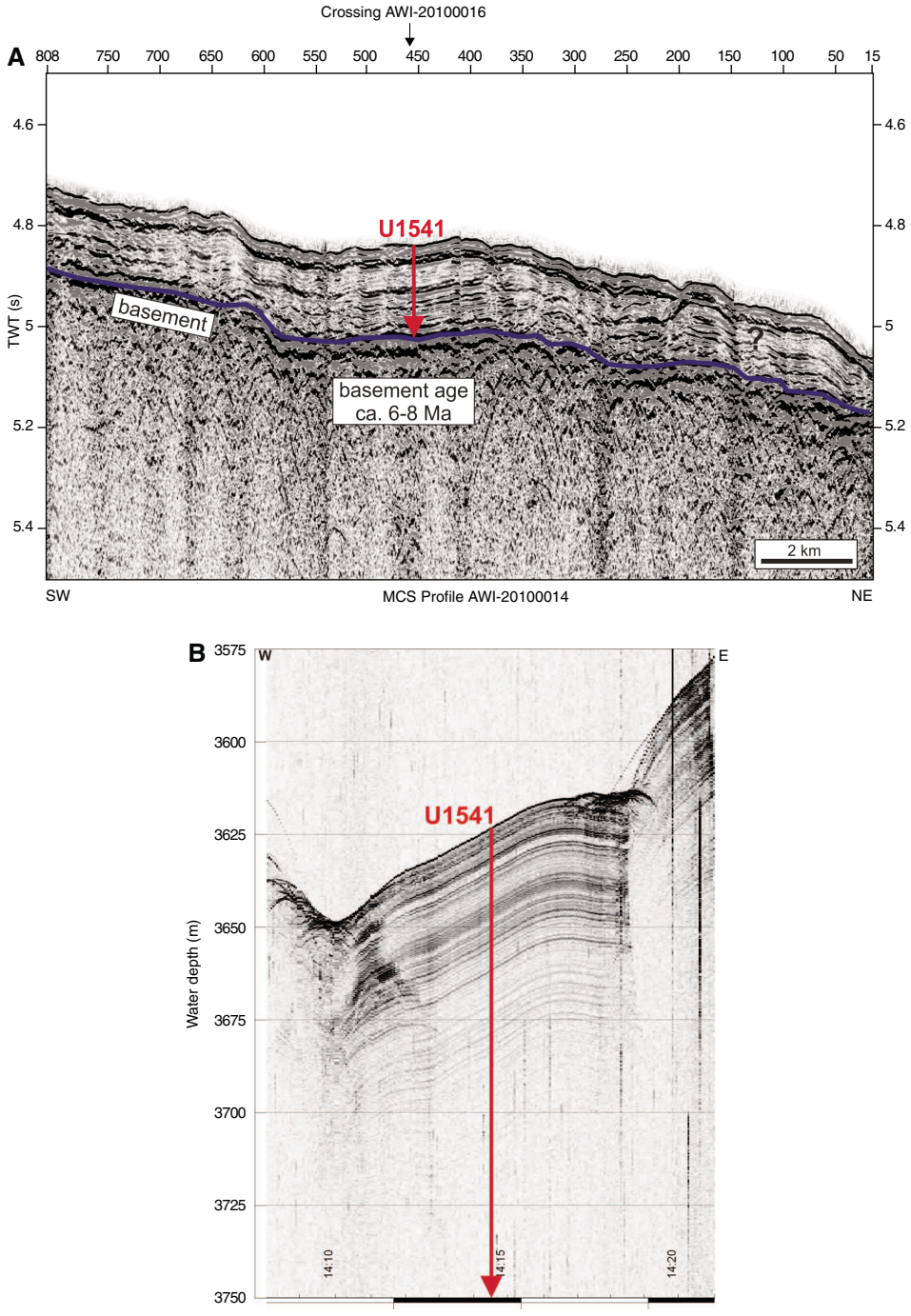

Figure F3. Modern salinity (black lines) and oxygen (colors) distributions in the central South Pacific used to visualize major water masses. SAF = Subantarctic Front, APF = Antarctic Polar Front, NPDW = North Pacific Deep Water, LCDW = Lower Circumpolar Deep Water, AABW = Antarctic Bottom Water.

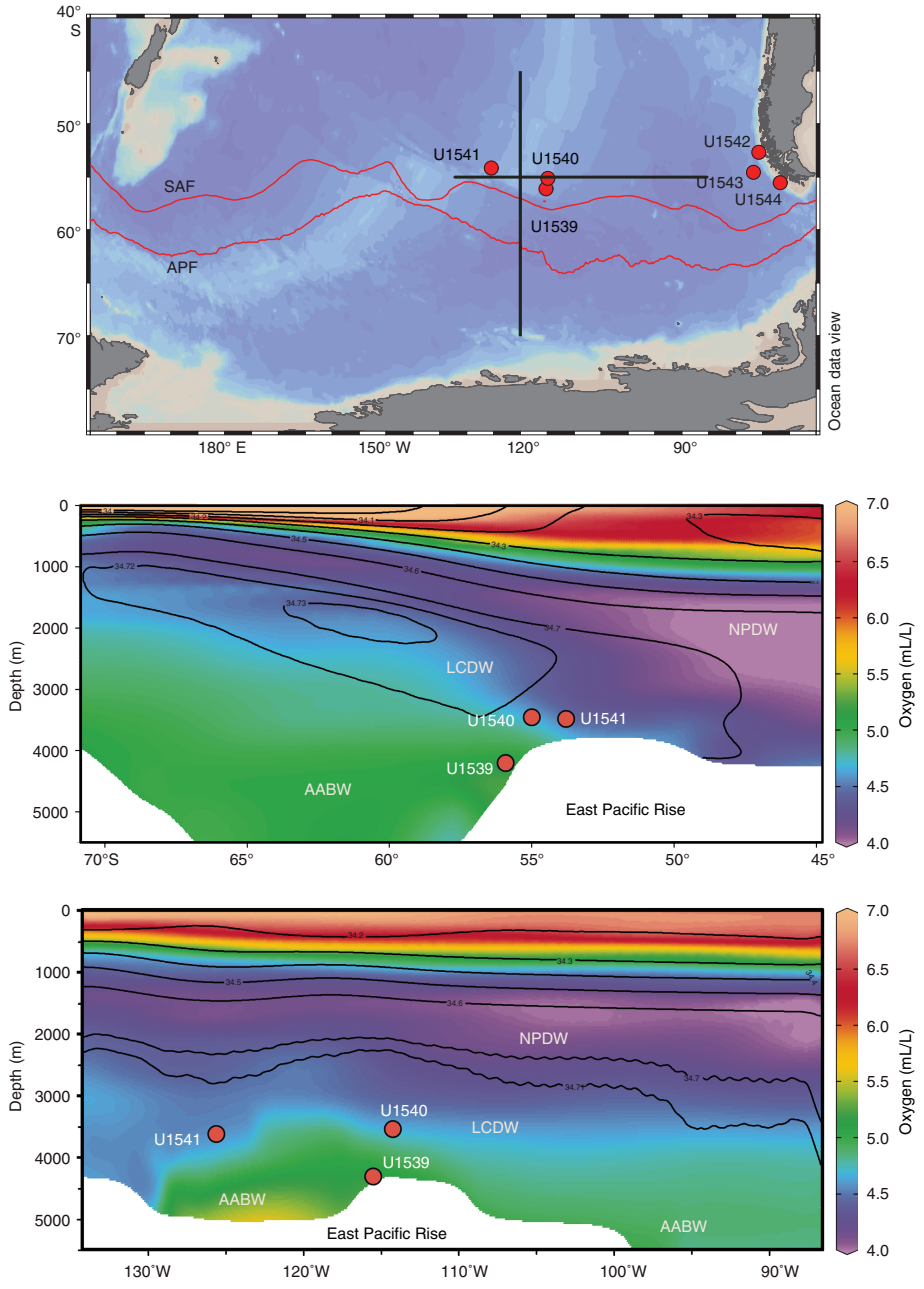

Operations

Three holes were cored at Site U1541 using the full-length advanced piston corer (APC) system. Hole U1541A was cored to 9.5 m core depth below seafloor, Method A (CSF-A) (9.67 m recovered; 101.8%). Hole U1541B was cored to 138.5 m CSF-A (129.27 m recovered; 93.3%). Hole U1541C was cored to 118.1 m CSF-A (100.37 m recovered; 85%) (Table **T1**).

Transit to Site U1541

During the transit to Site U1541, rough weather systems moved in and caused high seas at the site location. Therefore, upon reaching the site coordinates at ~2300 h on 15 June 2019, the vessel continued at reduced speed on a 245°SW weather avoidance course for another ~100 nmi past the site. At 2105 h on 16 June, the sea state had sufficiently calmed to turn the ship around and head back. We completed the transit and arrived at Site U1541 at 0736 h on 17 June. We lowered the thrusters, and the vessel was placed over the site coordinates and on dynamic positioning mode by 0820 h. Soon after, the drill crew started to build the APC/extended core barrel (XCB) bottom-hole assembly and to lower the drill pipe to the seafloor.

Site U1541

Hole U1541A

By 1815 h, the drill bit had been lowered to 3597 meters below rig floor (mbrf), 5 m above the seafloor depth calculated from the precision depth recorder reading. Core 383-U1541A-1H was at-

Table T1. Hole and coring summary, Site U1541. DRF = drilling depth below rig floor, DSF = drilling depth below seafloor, CSF = core depth below seafloor. APC = advanced piston corer, HLAPC = half-length APC, XCB = extended core barrel, RCB = rotary core barrel. Core type: H = APC, F = HLAPC, X = XCB, numeric = drilled interval. **Download table in CSV format.**

Hole: U1541A	**Hole: U1541B**	**Hole: U1541C**
Latitude: 54°12.7560′S	Latitude: 54°12.7553′S	Latitude: 54°12.7566′S
Longitude: 125°25.5480′W	Longitude: 125°25.5431′W	Longitude: 125°25.5288′W
Water depth (m): 3606.32	Water depth (m): 3603.72	Water depth (m): 3602.62
Date started (UTC, h): 17 Jun 2019 1115	Date started (UTC, h): 18 Jun 2019 0300	Date started (UTC, h): 19 Jun 2019 0400
Date finished (UTC, h): 18 Jun 2019 0300	Date finished (UTC, h): 19 Jun 2019 0400	Date finished (UTC, h): 20 Jun 2019 0500
Time on hole (days): 0.66	Time on hole (days): 1.04	Time on hole (days): 1.04
Seafloor depth DRF (m): 3617	Seafloor depth DRF (m): 3614.4	Seafloor depth DRF (m): 3613.4
Seafloor depth est. method: mudline core	Seafloor depth est. method: mudline core	Seafloor depth est. method: mudline core
Rig floor to sea level (m): 10.68	Rig floor to sea level (m): 10.68	Rig floor to sea level (m): 10.78
Penetration DSF (m): 9.5	Penetration DSF (m): 138.5	Penetration DSF (m): 118.1
Cored interval (m): 9.5	Cored interval (m): 138.5	Cored interval (m): 118.1
Recovered length (m): 9.67	Recovered length (m): 129.27	Recovered length (m): 100.37
Recovery (%): 101.79	Recovery (%): 93.34	Recovery (%): 84.99
Drilled interval (m):	Drilled interval (m):	Drilled interval (m):
Drilled interval (*N*): 0	Drilled interval (*N*): 0	Drilled interval (*N*): 0
Total cores (*N*): 1	Total cores (*N*): 16	Total cores (*N*): 13
APC cores (*N*): 1	APC cores (*N*): 15	APC cores (*N*): 13
HLAPC cores (*N*): 0	HLAPC cores (*N*): 0	HLAPC cores (*N*): 0
XCB cores (*N*): 0	XCB cores (*N*): 1	XCB cores (*N*): 0

Core	Top depth drilled DSF (m)	Bottom depth drilled DSF (m)	Interval advanced (m)	Recovered length (m)	Curated length (m)	Top depth cored CSF (m)	Bottom depth recovered (m)	Core recovery (%)	Time on deck (UTC h)	Sections (*N*)
383-U1541A-										
1H	0.0	9.5	9.5	9.67	9.67	0.0	9.67	102	18 Jun 2019 0300	8
383-U1541B-										
1H	0.0	7.1	7.1	7.06	7.06	0.0	7.06	99	18 Jun 2019 0420	6
2H	7.1	16.6	9.5	8.55	8.55	7.1	15.65	90	18 Jun 2019 0525	8
3H	16.6	26.1	9.5	8.29	8.29	16.6	24.89	87	18 Jun 2019 0635	7
4H	26.1	35.6	9.5	9.63	9.63	26.1	35.73	101	18 Jun 2019 0805	8
5H	35.6	45.1	9.5	9.60	9.60	35.6	45.20	101	18 Jun 2019 0915	8
6H	45.1	54.6	9.5	8.86	8.86	45.1	53.96	93	18 Jun 2019 1020	8
7H	54.6	64.1	9.5	7.10	7.10	54.6	61.70	75	18 Jun 2019 1205	6
8H	64.1	73.6	9.5	8.05	8.05	64.1	72.15	85	18 Jun 2019 1320	7
9H	73.6	83.1	9.5	9.44	9.44	73.6	83.04	99	18 Jun 2019 1435	8
10H	83.1	92.6	9.5	8.37	8.37	83.1	91.47	88	18 Jun 2019 1600	8
11H	92.6	102.1	9.5	9.49	9.49	92.6	102.09	100	18 Jun 2019 1740	8
12H	102.1	111.6	9.5	9.50	9.50	102.1	111.60	100	18 Jun 2019 1900	8
13H	111.6	121.1	9.5	9.01	9.01	111.6	120.61	95	18 Jun 2019 2020	7
14H	121.1	130.6	9.5	8.81	8.81	121.1	129.91	93	18 Jun 2019 2135	7
15H	130.6	138.0	7.4	7.45	7.45	130.6	138.05	101	18 Jun 2019 2310	6
16X	138.0	138.5	0.5	0.06	0.06	138.0	138.06	12	19 Jun 2019 0205	1
383-U1541C-										
1H	0.0	4.1	4.1	4.06	4.06	0.0	4.06	99	19 Jun 2019 0700	4
2H	4.1	13.6	9.5	6.47	6.47	4.1	10.57	68	19 Jun 2019 0825	6
3H	13.6	23.1	9.5	7.32	7.32	13.6	20.92	77	19 Jun 2019 0930	6
4H	23.1	32.6	9.5	9.25	9.25	23.1	32.35	97	19 Jun 2019 1035	7
5H	32.6	42.1	9.5	6.73	6.73	32.6	39.33	71	19 Jun 2019 1145	6
6H	42.1	51.6	9.5	9.20	9.20	42.1	51.30	97	19 Jun 2019 1255	7
7H	51.6	61.1	9.5	7.53	7.53	51.6	59.13	79	19 Jun 2019 1400	6
8H	61.1	70.6	9.5	9.13	9.13	61.1	70.23	96	19 Jun 2019 1515	7
9H	70.6	80.1	9.5	3.02	3.02	70.6	73.62	32	19 Jun 2019 1625	3
10H	80.1	89.6	9.5	8.82	8.82	80.1	88.92	93	19 Jun 2019 1735	8
11H	89.6	99.1	9.5	9.57	9.57	89.6	99.17	101	19 Jun 2019 1840	8
12H	99.1	108.6	9.5	9.47	9.47	99.1	108.57	100	19 Jun 2019 1950	8
13H	108.6	118.1	9.5	9.80	9.80	108.6	118.40	103	19 Jun 2019 2105	8

tempted, but it came up empty. Three more attempts followed with the bit at 3602, 3607, and finally 3617 mbrf before we successfully recovered any sediment. Hole U1541A was finally spudded at 2330 h on 17 June 2019. Core 1H recovered 9.5 m of sediment, indicating a missed mudline, and the hole was terminated at that point. The time spent in Hole U1541A was 15.75 h.

Hole U1541B

The bit was raised to 3612.0 mbrf, and Hole U1541B was spudded at 0055 h on 18 June 2019. Based on the recovery in Core 383-U1541B-1H, the seafloor was calculated at 3614.4 mbrf (or 3603.7 meters below sea level [mbsl]). Coring continued without incident until a partial stroke was recorded on Core 15H. When the core was

recovered, the advanced piston corer temperature (APCT-3) tool cutting shoe showed damage; therefore, the driller pulled back the following APC core barrel before it arrived at the bottom. An XCB core barrel was dropped to attempt Core 16X. After drilling for 45 min and advancing only 0.5 m, the barrel was pulled back on board. Core 16X retrieved three large pebble-sized basalt pieces (2–5 cm in diameter) in the core catcher. The bit was pulled out of the hole, clearing the seafloor at 0100 h and ending Hole U1541B.

A total of 16 cores were taken in Hole U1541B. The APC system was used for 15 of these, reaching 138.0 m CSF-A before APC refusal and recovering 129.3 m (94%). The XCB system was used for one core, advancing 0.5 m and recovering 0.06 m of basalt (12%). The APCT-3 tool was used on Cores 383-U1541B-4H, 7H, 11H, and 15H. Misfires were recorded on Cores 1H, 4H, and 6H, and a partial stroke was registered on Core 15H. A total of 25 h were spent in Hole U1541B.

Hole U1541C

The vessel was offset 20 m east of Hole U1541B, the bit was raised to 3608.0 mbrf, and Hole U1541C was spudded at 0325 h on 19 June 2019. The full-length APC system was used to core the hole to 118.1 m CSF-A (Cores 383-U1541C-1H through 13H) before coring was terminated at 1805 h on 19 June to allow the vessel to evade approaching heavy weather.

The bit was pulled to the surface, clearing the rotary table at 0140 h on 20 June. The drill collars were laid out and the rig floor was secured for transit at 0204 h on 20 June, ending Hole U1541C and Site U1541. A total of 13 APC cores were taken over a 118.1 m interval with a recovery of 100.4 m (85%). Formation temperature measurements were not taken.

At 0236 h on 20 June, the vessel began a transit northeast of Site U1541 to avoid heavy weather headed toward the operational area. By midnight on 23 June, the vessel had traveled 772 nmi.

Sedimentology

Site U1541 is located north of the SAF at 54°12.76′S, 125°25.54′W, at approximately 3604 m water depth 160 nmi west of the EPR mid-ocean ridge and 370 nmi west of Site U1540. The basement age at Site U1541 is estimated at between 6 and 8 Ma. Site U1541 completes a set of three pelagic sites drilled in the open-ocean central South Pacific during Expedition 383 (Sites U1539–U1541) and will be used to reconstruct physical, chemical, and biological changes in the Pacific Southern Ocean from the Miocene to present. Site U1541 is particularly well suited to address the long-term evolution of past changes in the ACC and the southern high-latitude carbon cycle along with their climate implications.

The three holes (U1541A–U1541C) occupied at Site U1541 provide the basis for a composite ~146 m thick sedimentary sequence containing Holocene to Miocene sediments (see **Stratigraphic correlation**). Hole U1541B recovered the deepest sediments at 138.5 m CSF-A, but it was abandoned after APC refusal and when subsequent XCB drilling (Core 383-U1541B-16X) retrieved only three large pebble-sized rock fragments. Relatively high seas during drilling operations occasionally caused APC misfires, which led to incomplete strokes of the piston corer (see **Operations**) and caused fall-in and suck-in coring disturbances at the top and base of sediment cores, respectively (e.g., Core 383-U1541B-4H). The identification and classification of sediments disturbed by drilling operations is outlined in **Sedimentology** in the Expedition 383 methods chapter (Winckler et al., 2021a) and is largely based on disturbance described by Jutzeler et al. (2014). Severe drilling-disturbed sediments were classified as mixed biogenic oozes in the visual core descriptions (VCDs) and hole summaries (Figure **F4**), and examples are found in Sections 383-U1541B-4H-1 through 4H-7, 6H-1, and 383-U1541C-12H-1. Despite these difficulties, the composite stratigraphy developed from Holes U1541A–U1541C provide a near-complete and continuous sedimentary sequence from the Miocene to Holocene (see **Biostratigraphy** and **Stratigraphic correlation**).

Lithofacies description

Four lithofacies were identified at Site U1541 (Table **T2**). The numbering of the facies is based on all facies documented for Expedition 383, but only lithofacies documented at Site U1541 are described and discussed here. All lithofacies defined at Site U1541 (Lithofacies 2, 3, 4, and 6) can be represented in a ternary diagram with diatom ooze, nannofossil ooze, and clay as end-members (Figure **F5**). Beds of carbonate-bearing to carbonate-rich diatom ooze (Lithofacies 2) (Figure **F6**) and clay-bearing and clayey biogenic ooze (Lithofacies 6) compose a minor proportion of the sedimentary sequence at Site U1541 (about 8% and 9%, respectively). Site U1541 sediments are dominated by diatom-bearing to diatom-rich calcareous or nannofossil ooze (Lithofacies 3; 55%) (Figure **F7**) and essentially pure nannofossil ooze with no major modifying or accessory components (Lithofacies 4; 28%) (Figure **F8**).

Lithofacies 2

Lithofacies 2 is light greenish gray (10GY 7/1) to gray (N 6/) carbonate-bearing to carbonate-rich diatom ooze (Figure **F6**) that exhibits moderate to heavy bioturbation and may show wavy and/or discontinuous centimeter-scale bedding. Minor modifying components (10%–49%) are calcareous in nature and include nannofossils, foraminifers, and calcareous debris (mostly fragmented foraminiferal shells). Accessory components (<10%) include radiolarians, silicoflagellates, and sponge spicules. Dropstones >0.5 mm, distinct millimeter- to centimeter-scale diatom mats, and distinct color mottling are associated with this lithofacies. Bed thicknesses commonly range from 0.2 to 1.4 m.

Lithofacies 3

Lithofacies 3 is light greenish/blueish gray (10G 7/1 and 5B 7/1) and very pale yellow to pale orange yellow (2.5Y 9/2 to 10YR 9.5/2) diatom- and carbonate-bearing to diatom-rich nannofossil ooze (Figure **F7**) that appears with a variety of minor and accessory components. The carbonate modifier of this lithofacies is often composed of calcareous debris mostly derived from fragmented foraminifers. The more common biosiliceous modifier is composed of diatoms with rare occurrences of radiolarians, silicoflagellates, and sponge spicules. This facies appears moderately to heavily bioturbated (see **Bioturbation**) and is sometimes mottled with darker grayish patches due to burrow infills and diagenetic overprints (e.g., the precipitation of iron sulfides). X-ray images reveal only minor abundances of dropstones. The bed thickness of this lithofacies varies from 0.1 to 15 m in the Site U1541 sediment record.

Lithofacies 4

Lithofacies 4 is characterized by nannofossil ooze that is heavily bioturbated (see **Bioturbation**) and often has a massive appearance. Its color ranges from white (N 9/) and very light gray (N 7/) to very pale brown (10YR 8/2) and pale orange yellow (10YR 9.5/2) (Figure **F8**). It is characterized by only rare occurrences of carbonate (fora-

Figure F4. A–C. Hole summaries, Site U1541. The placement of Pliocene and early Pleistocene stage boundaries in Holes U1541B and U1541C are estimated using the preliminary Site U1541 shipboard age model. GRA = gamma ray attenuation, MSP = point magnetic susceptibility, RGB = red-green-blue, NGR = natural gamma radiation, cps = counts per second. (Continued on next two pages.)

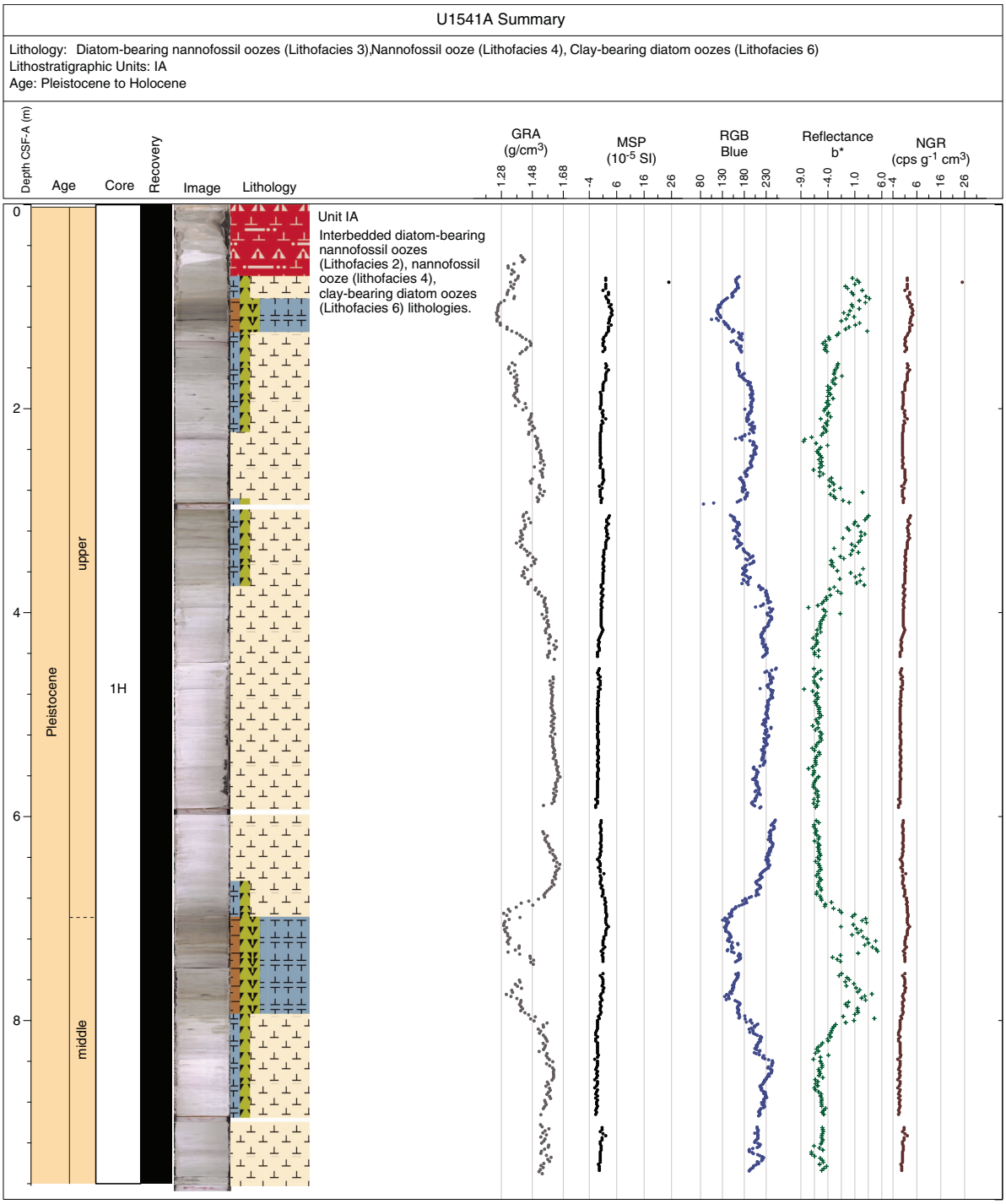

minifers) and various biosiliceous components. Mottled patches of darker grayish colors due to diagenetic iron sulfide overprints can be found in this lithofacies. The pale orange yellow variety of nannofossil oozes may show an increased abundance of Fe oxides and is dominated by two large coccolithophorid species, *Reticulofenestra pseudoumbilicus* and *Coccolithus pelagicus*. Dropstones are absent in this lithofacies. The bed thickness of Lithofacies 4 at Site U1541 varies from 0.2 to 6 m.

Lithofacies 6

Lithofacies 6 is clay-bearing to clayey biogenic ooze. It is characterized by a light greenish gray color (10Y 7/1, 10Y 6/1, or 5GY 7/1), is moderately to heavily bioturbated (see **Bioturbation**), and contains more than 10% clay-sized lithogenic components. The major lithology consists of biogenic components and may be dominated by diatoms or nannofossils. X-ray diffraction (XRD) analyses suggest a variable contribution of clay minerals and quartz to the clay-

Figure F4 (continued). (Continued on next page.)

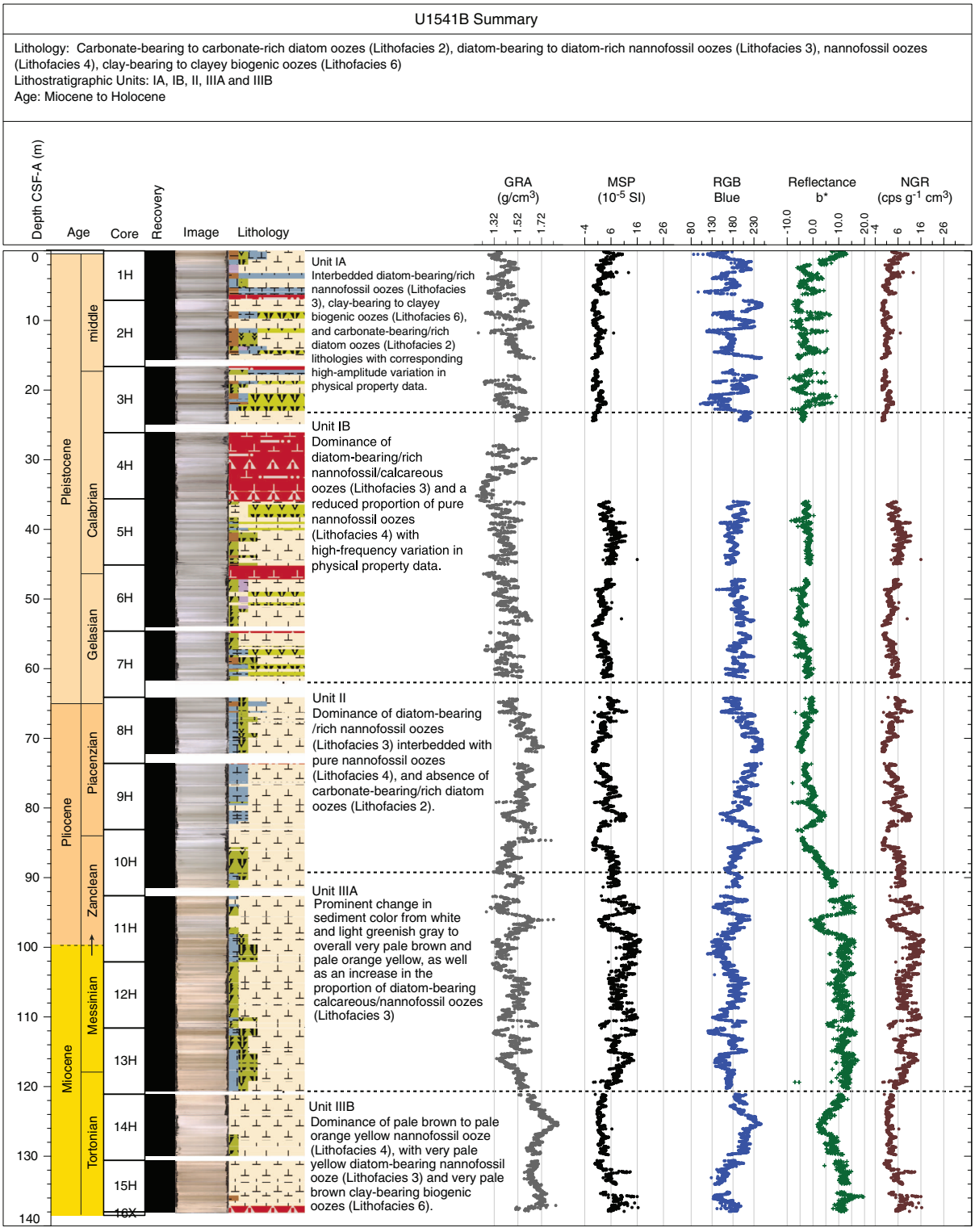

sized lithogenic fraction (see **X-ray diffraction clay mineralogy**). Accessory components (<10%) include radiolarians, silicoflagellates, and sponge spicules. X-radiographs indicate that dropstones can be present in this lithofacies in similar abundance to Lithofacies 2 and 3. The thickness of this lithofacies in the sedimentary record varies from 0.4 to 2 m.

Lithostratigraphic units

Based on the frequency and occurrence of the four lithofacies observed at Site U1541, the sedimentary sequence is divided into three lithostratigraphic units, and the youngest and oldest units are each divided into two subunits, A and B. The criteria used to define

Figure F4 (continued).

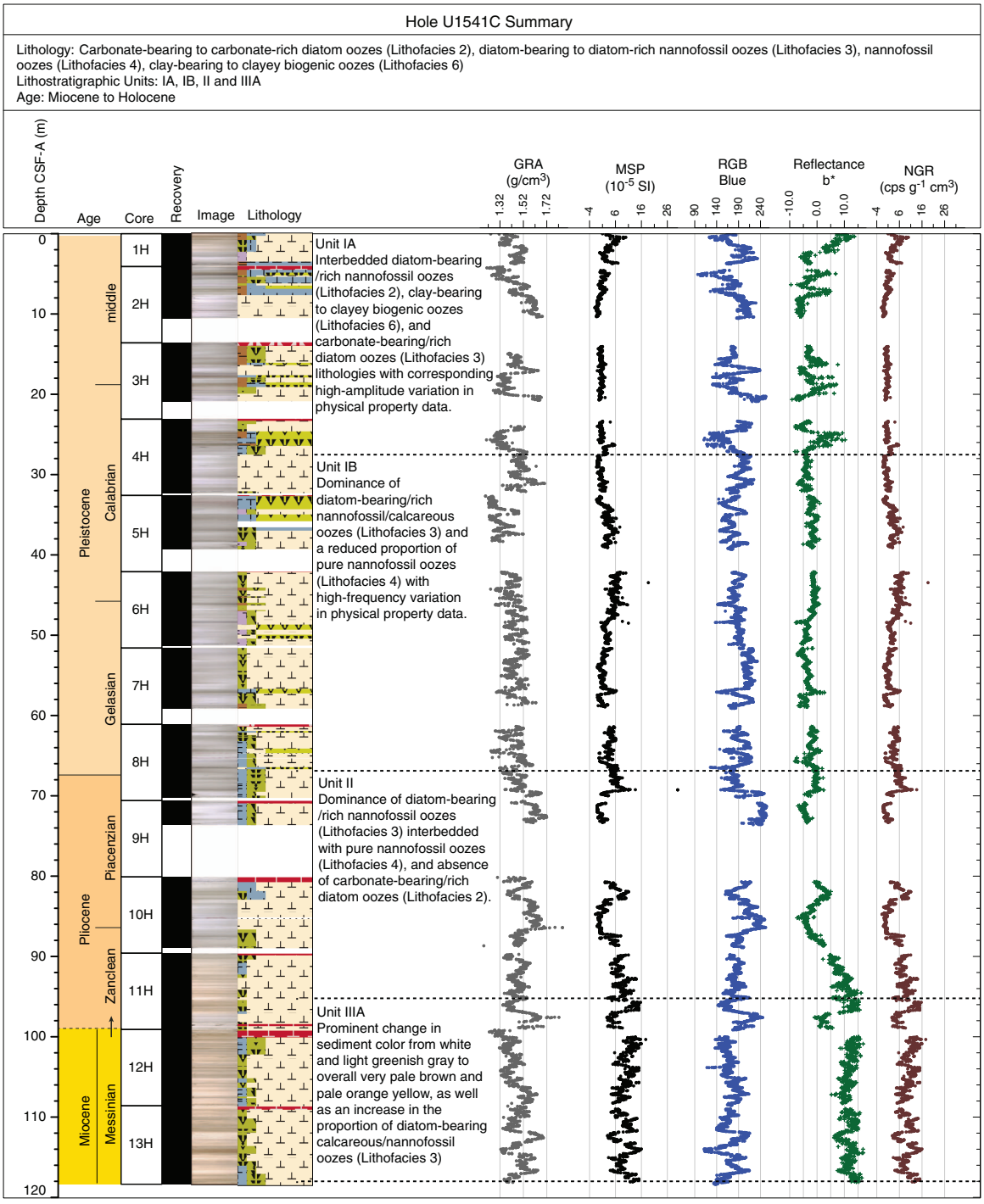

unit boundaries are discussed below and highlighted in Figure F9. Key unit characteristics, including depths within the Site U1541 sedimentary sequence and corresponding ages according to the preliminary shipboard age model, are also discussed below.

Unit I

Subunit IA

Intervals: 383-U1541A-1H-1, 0 cm, to 1H-CC, 14 cm; 383-U1541B-1H-1, 0 cm, to 3H-6, 12 cm; 383-U1541C-1H-1, 0 cm, to 4H-4, 7 cm

Depths: Hole U1541A = 0–9.67 m CSF-A, Hole U1541B = 0–23.12 m CSF-A, Hole U1541C = 0–27.69 m CSF-A, Site U1541 composite section = 0–27.34 m core composite depth below seafloor, Method A (CCSF-A)

Thickness: 27.34 m

Age: Calabrian and middle Pleistocene to Holocene (younger than 0.98 Ma)

Lithology: diatom-bearing to diatom-rich nannofossil oozes, clay-bearing to clayey biogenic oozes, carbonate-bearing to carbonate-rich diatom oozes

Table T2. Description of lithofacies, Site U1541. **Download table in CSV format.**

Type	Lithofacies	Description	Thickness (m)	Degree of bioturbation	Color	Proportion in lith. units/subunits (%)	Depositional environment
Carbonate-bearing to carbonate-rich diatom ooze	2	Carbonate-bearing to carbonate-rich diatom ooze with occasional occurrence of diatom mats; minor components (10%–49%): nannofossils and calcareous debris of mostly foraminiferal shells; accessory components (<10%): radiolarians, silicoflagellates, and sponge spicules; high abundance of dropstones >0.5 cm; frequent mottling; sporadic color banding	0.2–1.4	Moderate–heavy	Light greenish gray (10GY 7/1) to gray (N 6/)	IA: 2.6 IB: 25.5	Pelagic
Diatom-bearing to diatom-rich nannofossil/calcareous ooze	3	Diatom-bearing or diatom-rich nannofossil (and/or calcareous) oozes; weak wavy centimeter-scale bedding; minor components mainly consist of diatoms; common mottling due to diagenetic overprints; minor abundances of dropstones	0.1–15.0	Moderate–heavy	Light greenish/blueish gray (10G 7/1 and 5B 7/1) and very pale yellow (2.5Y 9/2)	IA: 27.4 IB: 53.0 II: 58.9 IIIA: 84.9 IIIB: 20.3	Pelagic
Nannofossil ooze	4	Nannofossil/calcareous ooze often with a massive and homogeneous appearance; rare foraminifers and biosiliceous components; mottling, diagentic overprinting, and color banding is frequent; absence of dropstones	0.2–6.0	Heavy	White (N 9/); very light gray (N 7/); very pale brown (10YR 8/2); pale orange yellow (10YR 9.5/2)	IA: 35.9 IB: 13.8 II: 40.3 IIIA: 15.1 IIIB: 74.7	Pelagic, hydrothermal overprint
Clay-bearing to clayey biogenic ooze	6	Clay-bearing biogenic ooze with >10% clay-sized lithogenics; major lithology either dominated by diatoms or nannofossils; variable contribution of clay minerals and quartz to the clay-sized lithogenic fraction; common mottling and color banding	0.4–2.0	Moderate–heavy	Light greenish gray (10Y 7/1, 10Y 6/1, 5GY 7/1)	IA: 34.1 IB: 7.7 II: <1 IIIB: 5.0	Pelagic

Lithostratigraphic Subunit IA spans the upper 27.34 m of Site U1541 and consists of interbedded light greenish gray diatom-bearing and diatom-rich nannofossil oozes (Lithofacies 3; 27.4% of the total unit thickness), white nannofossil oozes (Lithofacies 4; 35.9%), and light greenish gray to greenish gray clay-bearing to clayey biogenic oozes (Lithofacies 6; 34.1%). Carbonate-bearing or carbonate-rich diatom oozes (Lithofacies 2) only occur sporadically (2.6%). Sediments are moderately to heavily bioturbated, and lithologic transitions are gradational.

Subunit IB

Intervals: 383-U1541B-3H-6, 12 cm, to 7H-CC, 40 cm; 383-U1541C-4H-4, 7 cm, to 8H-4, 106 cm
Depths: Hole U1541B = 23.12–61.7 m CSF-A, Hole U1541C = 27.69–66.66 m CSF-A, Site U1541 composite section = 27.34–66.65 m CCSF-A
Thickness: 39.31 m
Age: Gelasian and Calabrian (Pleistocene) (~0.98 to ~2.58 Ma)
Lithology: (diatom-bearing/rich) nannofossil oozes, (carbonate-bearing/rich) diatom oozes, clay-bearing to clayey biogenic oozes

Lithostratigraphic Subunit IB spans 27.34–66.65 m CCSF-A and exhibits a dominance of diatom-bearing and diatom-rich nannofossil/calcareous oozes (Lithofacies 3; 53.0% of the total unit thickness) and a reduced proportion of pure nannofossil oozes (Lithofacies 4; 13.8%). At the same time, the proportion of light greenish gray to greenish gray carbonate-bearing and carbonate-rich diatom oozes (Lithofacies 2) increases to 25.5% and clay-bearing or clayey biogenic oozes (Lithofacies 6) become less abundant (7.7%). Sediments are moderately to heavily bioturbated, and in the case of pure nannofossil oozes, they can have a massive and homogeneous appearance. Lithologic transitions are generally gradational.

A reduced occurrence of pure nannofossil ooze (Lithofacies 4) demarcates this unit from Subunit IA above (Figure **F9**). Subunit IB lithologies do not exhibit a dynamic range of lithologic variation and are more muted in appearance than in Subunit IA. This observation is reinforced by the low-amplitude variations in b* and red-green-blue color space (RGB) blue intensity in Subunit IB (Figure **F4**) (see **Integrating physical property measurements with lithofacies observations**).

Unit II

Intervals: 383-U1541B-8H-1, 0 cm, to 10H-5, 37 cm; 383-U1541C-8H-6, 106 cm, to 11H-1, 63 cm
Depths: Hole U1541B = 61.07–89.39 m CSF-A, Hole U1541C = 66.66–90.23 m CSF-A, Site U1541 composite section = 66.65–93.5 m CCSF-A
Thickness: 26.85 m
Age: Zanclean and Piacenzian (Pliocene) (~2.58 to ~4.2 Ma)
Lithology: (diatom-bearing/rich) nannofossil ooze

Lithostratigraphic Unit II spans from 66.65 to 93.5 m CCSF-A and consists almost entirely of light greenish gray diatom-bearing or diatom-rich nannofossil ooze (Lithofacies 3; 58.9% of the total unit thickness) interbedded with white almost pure nannofossil ooze (Lithofacies 4; 40.3%). Sediments are heavily bioturbated to homogeneous and have a mottled appearance. Transitions between the lithologies are gradational. Carbonate-bearing and carbonate-rich diatom oozes are absent in this unit, and clay-bearing to clayey biogenic oozes (Lithofacies 6) only appear rarely (0.7%).

The downhole disappearance of diatom oozes as a dominant lithology marks the onset of Unit II at 66.65 m CCSF-A (Figure **F9**). This unit boundary also coincides with the start of a gradual shift of mean gamma ray attenuation (GRA) bulk density and RGB blue intensity to higher values (Figure **F4**).

Unit III

Subunit IIIA

Intervals: 383-U1541B-10H-5, 37 cm, to 13H-CC, 30 cm; 383-U1541C-11H-1, 63 cm, to 13H-CC, 25 cm
Depths: Hole U1541B = 89.39–120.56 m CSF-A, Hole U1541C = 95.64–118.4 m CSF-A, Site U1541 composite section = 93.5–127.51 m CCSF-A

Figure F5. Primary lithologies used to define sedimentary lithofacies, Site U1541. Pie charts show their relative contributions to Lithostratigraphic Subunits IA and IB, Unit II, and Subunits IIIA and IIIB.

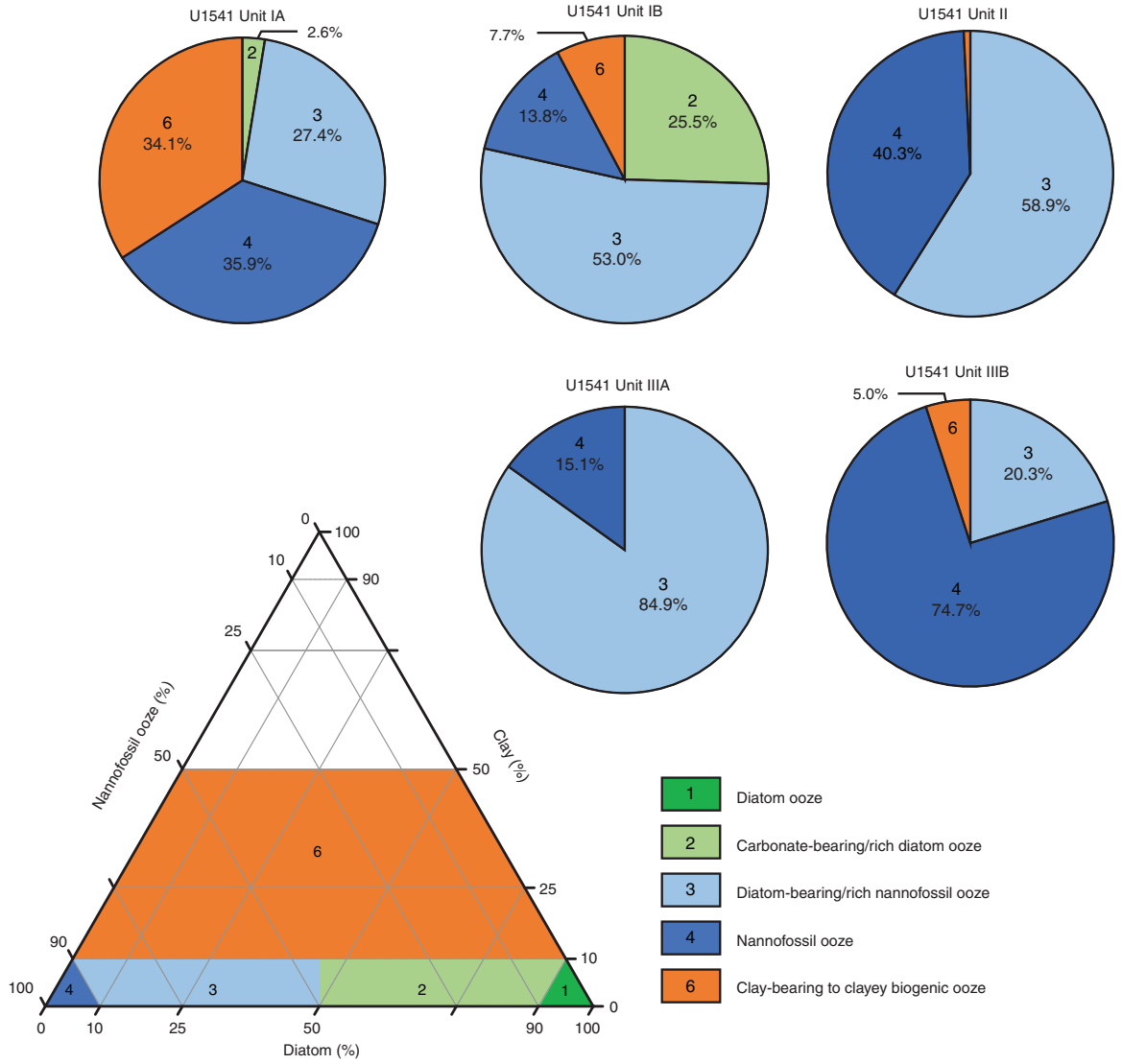

Thickness: 28.64 m
Age: Messinian and Zanclean (Miocene and Pliocene) (~4.2 to ~7.2 Ma)
Lithology: (diatom-bearing/rich) nannofossil oozes

Lithostratigraphic Subunit IIIA ranges from 93.5 to 127.51 m CCSF-A and consists entirely of very pale brown to pale orange yellow diatom-bearing calcareous/nannofossil oozes (Lithofacies 3; 84.9% of the total unit thickness) and white pure nannofossil oozes (Lithofacies 4; 15.1%). Sediments are generally heavily bioturbated and mottled by burrows, and lithologic transitions are gradational.

Subunit IIIA is distinguished from Unit II by a prominent change in sediment color from white and light greenish gray to overall very pale brown and pale orange yellow, as well as an increase in the proportion of diatom-bearing calcareous/nannofossil oozes from 58.9% to 84.9% (Lithofacies 3) (Figure **F9**). The unit boundary is also characterized by a change in b* color reflectance values and magnetic susceptibility (MS) (see **Integrating physical property measurements with lithofacies observations**).

Subunit IIIB

Intervals 383-U1541B-14H-1, 0 cm, to 15H-5, 136 cm
Depths: Hole U1541B = 121.1–137.98 m CSF-A, Site U1541 composite section = 128.55–145.93 m CCSF-A
Thickness: 17.38 m
Age: Tortonian and Messinian (Miocene) (~7.2 to ~8.5 Ma)
Lithology: nannofossil ooze with varying minor biogenic and siliciclastic components

Lithostratigraphic Subunit IIIB spans from 128.55 to 145.93 m CCSF-A and consists of dominantly pale brown to pale orange yellow nannofossil ooze with foraminifers (Lithofacies 4; 74.7% of the total unit thickness) with contributions from very pale yellow diatom-bearing nannofossil ooze with foraminifers (Lithofacies 3; 20.3%) and very pale brown clay-bearing biogenic oozes (Lithofacies 6; 5%). These oozes have a massive and homogeneous appearance and are heavily bioturbated and mottled by large burrows.

Subunit IIIB is distinguished from Subunit IIIA by the absence of diatoms and other biosiliceous components and a marked domi-

Figure F6. Representative (A) core and (B) X-ray and photomicrograph images of mineral properties of Lithofacies 2 (carbonate-bearing and carbonate-rich diatom ooze) in (C) plane-polarized light (PPL) and (D) cross-polarized light (XPL), Hole U1541C.

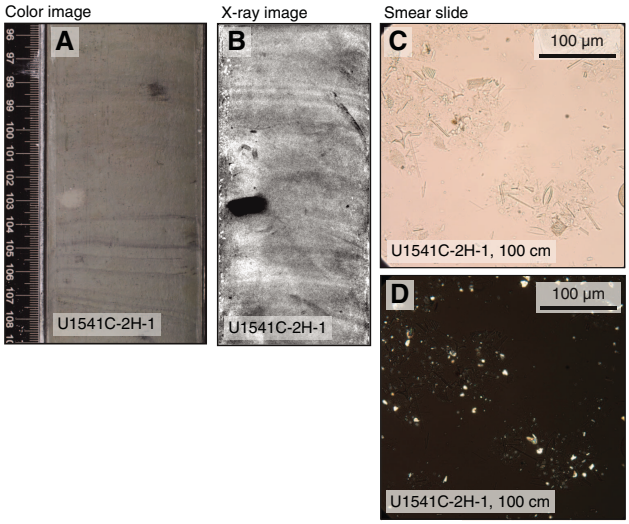

Figure F7. Representative (A) core and (B) X-ray and photomicrograph images of mineral properties of Lithofacies 3 (diatom-bearing and diatom-rich calcareous/nannofossil ooze) in (C) PPL and (D) XPL, Hole U1541C.

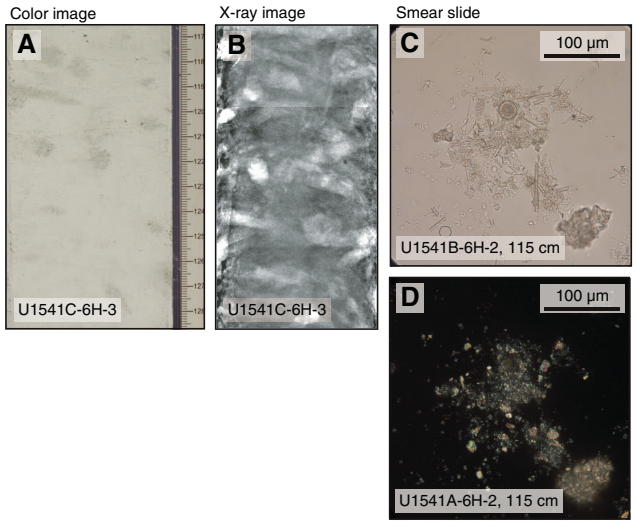

nance of nearly pure nannofossil ooze (Lithofacies 4) (Figure **F9**). In contrast to Subunit IIIA, nannofossil ooze lithofacies comprise 74.7% of the sedimentary sequence in Subunit IIIB, which is a significant increase compared to 15% in Subunit IIIA. Here, the nannofossil assemblage is composed predominantly of two large coccolithophorid species, *R. pseudoumbilicus* and *C. pelagicus* (see **Biostratigraphy**).

Complementary analyses

Petrology

Dark, glassy rock fragments of various sizes and irregular shapes were observed on the split surfaces of the section halves and in X-ray photographs in Sections 383-U1541B-15H-5 and 15H-CC (Figure **F10**). Photomicrographs of thin sections obtained from these fragments reveal phenocrysts of olivine, pyroxene, and tabular elongate plagioclase in a vitric matrix. The rock fragments are further covered by palagonite consisting of iron (hydr)oxides and clays. These observations indicate that the rock fragments at the base of Hole U1541B are volcanic glass.

Three pieces of large pebble-sized rocks (2–5 cm in diameter) were recovered in Section 383-U1541B-16X-CC. These very dark bluish (5PB 3/1) rocks are irregular and rounded in shape and have a weathered exterior. Crosscut surfaces reveal a ~0.5 mm thick vesicular chilled margin (Figure **F11**). Thin section observations indicate that microphenocrysts of pyroxene and acicular plagioclase with twinning in a fine-grained aphanitic matrix are present. The microphenocrysts show partial intergrowth. The matrix is vesicular and highly altered to brownish material, possibly iron (hydr)oxides. These observations point to the recovery of pillow basalt in Section 16X-CC. The presence of basalt rock and volcanic glass fragments at the base of Hole U1541B suggest the complete recovery of the sedimentary sequence above the basement rock.

X-ray diffraction clay mineralogy

XRD analyses were performed on 15 powdered samples obtained from Holes U1541A and U1541B to identify the mineralogy and composition of the lithogenic fraction of sediments at this site. The X-ray diffractograms reveal characteristic patterns within the individual lithostratigraphic units identified at this site.

Subunit IA shows clear peaks of detrital minerals such as quartz, feldspar (plagioclase), and phyllosilicates including illite, chlorite, kaolinite, and smectite (Figure **F12**). Samples obtained from Subunit IB often show a wide peak between 18° and 30°2θ that is associated with amorphous biogenic silica. X-ray diffractograms of samples obtained from Units II and III often reveal four characteristic calcite peaks at 26.6, 29.5, 36.1, and 39.5°2θ. Although the samples were double treated with acetic acid and agitated for 18 h (see **Sedimentology** in the Expedition 383 methods chapter [Winckler et al., 2021a]), a significant fraction of the carbonate phase remained undissolved and hence dominates the X-ray diffractograms. Additionally, samples from Units II and III show a narrow peak at 3.57 Å (24.9°2θ) that overlaps with kaolinite [002]. The amplitude of this peak is not diminished upon heating to 550°C, suggesting the presence of a well-structured crystalline mineral whose identity cannot be further characterized.

Bioturbation

Sediments at Site U1541 are moderately to heavily affected by bioturbation. Macroscopic evidence for the effects of postdepositional sediment mixing by deep-penetrating organisms at Site U1541 mostly comes from burrows observed at lithologic transitions with distinct color changes, which likely reach into the preserved "transitional layer" of the sediment column at the time of deposition (Tiers III and IV after Wetzel and Uchman, 2012) (Figure **F13**). Evidence for strong bioturbation in the homogenized bioturbation mixed layer at the time of sediment deposition (Tiers I and II after Wetzel and Uchman, 2012) was interpreted from X-radiographs. Classified in most cases as heavy bioturbation, all Site U1541 cores show various overlapping bioturbation patterns and activity of various benthic communities during different times of deposition. Traces of *Chondrites, Paleophycus, Planolites, Skolithos, Thalassinoides*, and *Zoophycos* (Gage and Tyler, 1991) can be distinguished from the X-ray images. The vertical extent of (postdepositional) sediment displacement (i.e., the bioturbation depth) is 10 cm on average and in some cases reaches as much as 40 cm.

Figure F8. A–H. Representative images and mineral properties of Lithofacies 4 (nannofossil ooze), Holes U1541A–U1541C. Upper and lower panels show the white and pale orange-yellow varieties in this lithofacies, respectively. (C, G) PPL, (D, H) XPL.

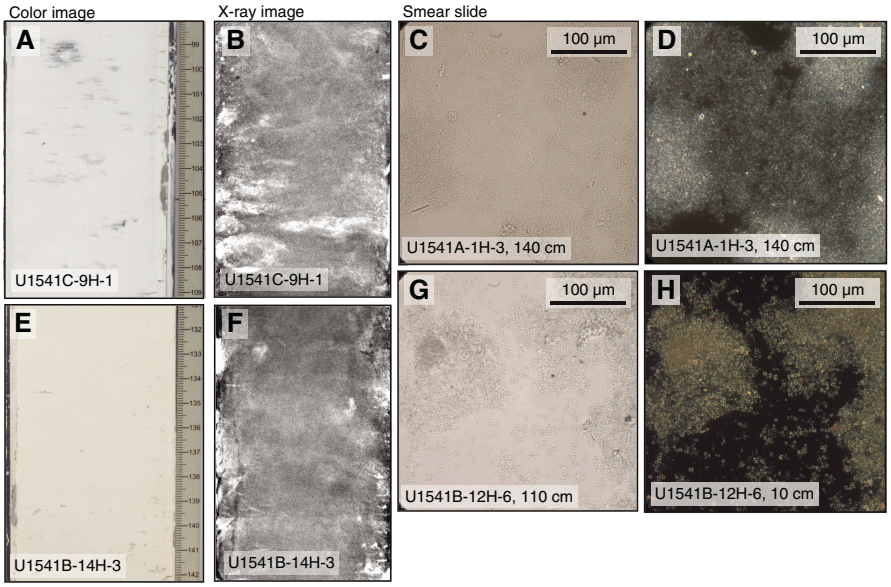

Figure F9. Summary of primary lithostratigraphic variations, Site U1541. Lithostratigraphic units were defined based on the distribution, occurrence, and composition of major lithofacies (see Lithostratigraphic units). Relative age of the units is based on the preliminary Site U1541 shipboard age model (see Biostratigraphy and Stratigraphic correlation). MSP = point magnetic susceptibility, RGB = red-green-blue.

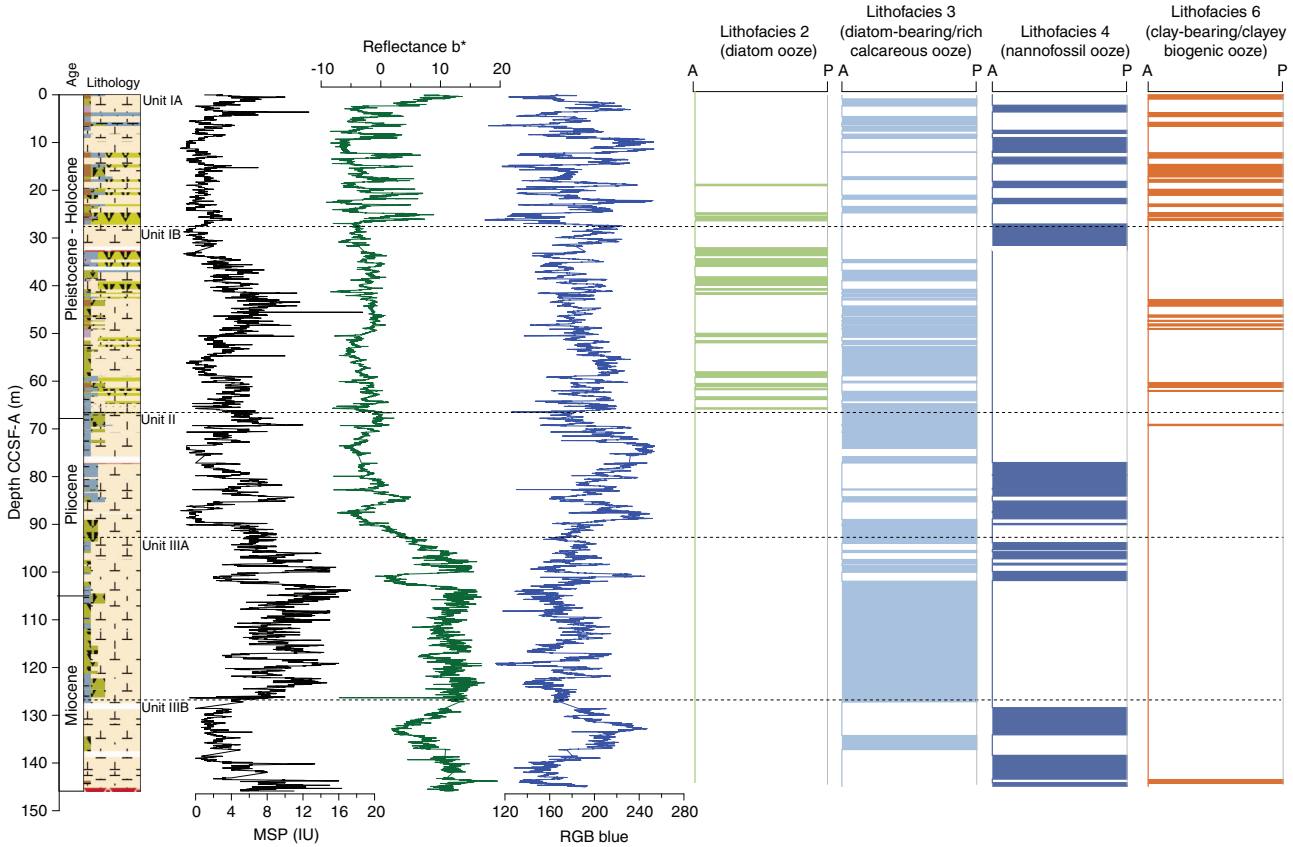

Integrating physical property measurements with lithofacies observations

The distribution of Site U1541 lithologies was compared to downcore physical property measurements including GRA bulk density, MS, natural gamma radiation (NGR), RGB blue intensity, and color reflectance b* (see **Physical Properties** in the Expedition 383 methods chapter [Winckler et al., 2021a]) to identify relation-

Figure F10. Weathered glass shards in sediment (383-U1541B-15H). A. Rock fragments found at the split surface (15H-5, 45–53 cm). B–F. Volcanic glass shard (15H-CC; C: PPL, D: XPL). Altered devitrified rim is being replaced by Fe (hydr)oxides and clay (E: PPL, F: XPL). G = glass matrix, O = olivine, Pa = palagonite, Pl = plagioclase, Px = pyroxene.

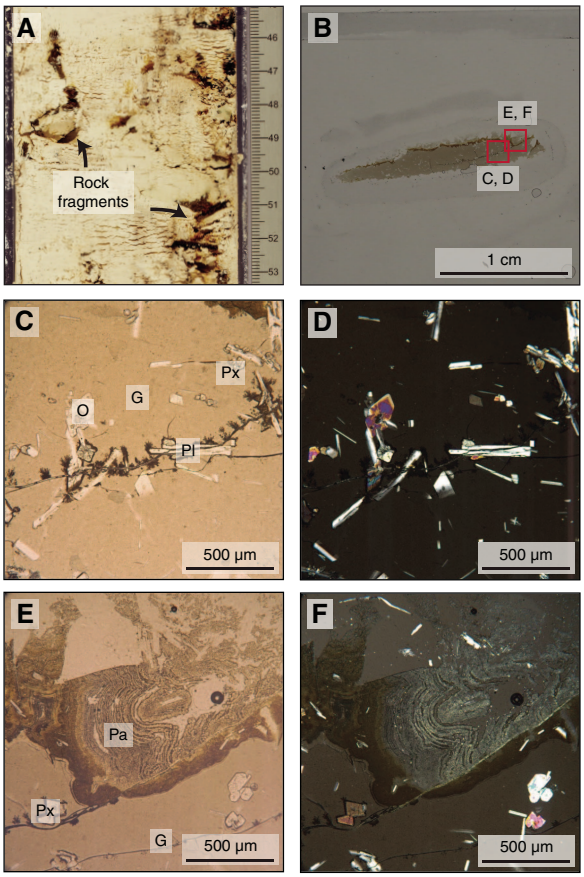

Figure F11. Rock samples (383-U1541B-16X-CC). A. Rock with 5 mm wide chilled margin at the crosscut surface. B–D. Rock specimen (C: PPL, D: XPL). G = glass matrix, Pl = plagioclase, Px = pyroxene.

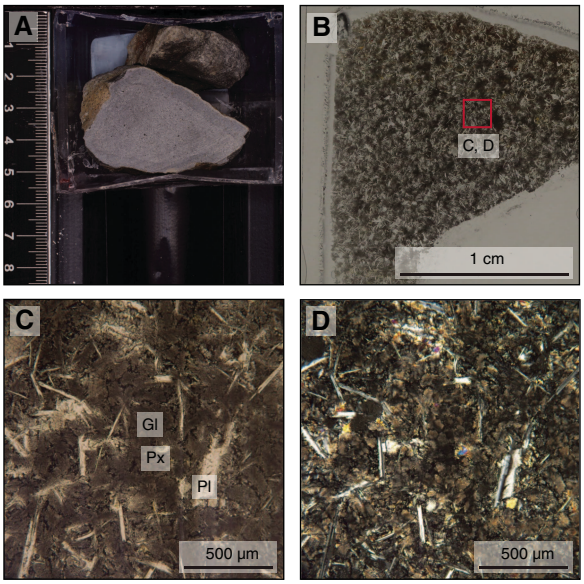

Figure F12. X-ray diffractograms of representative samples of each lithofacies, Hole U1541B. Minerals occurring in the samples include quartz (Qtz), plagioclase (Pl), and calcite (C) and phyllosilicates including illite (Il), chlorite (Chl), smectite (Sm), kaolinite (K), and their composite ("Clay").

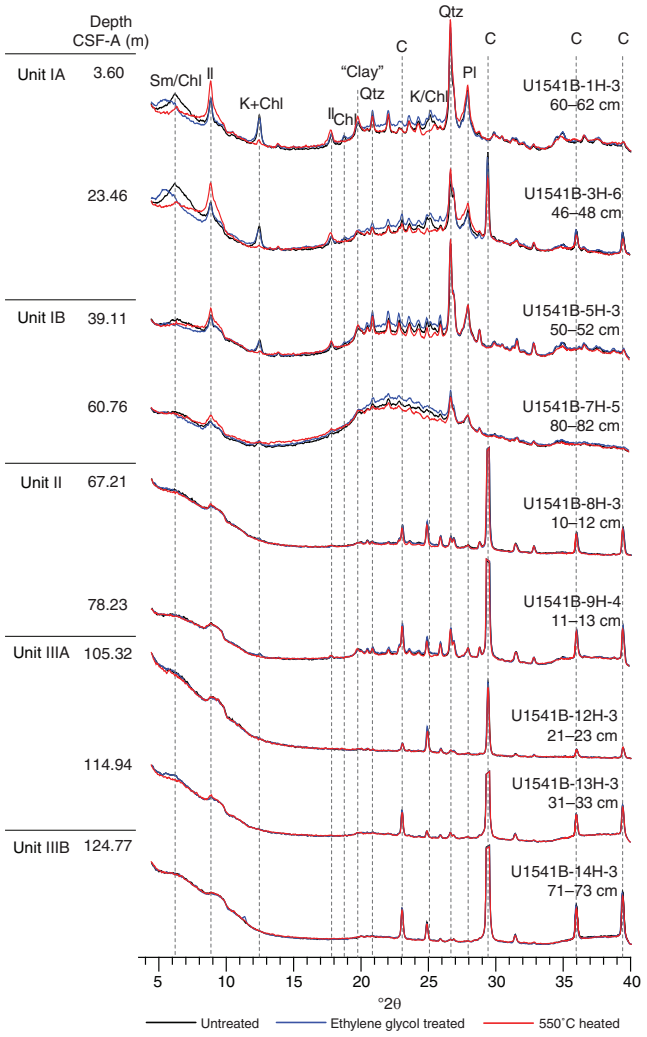

ships between lithology and measured downcore data. Five intervals display the diversity of sediment types at Site U1541 (Figure **F14**):

- Subunit IA, Cores 383-U1541B-2H and 3H (7–25 m CSF-A);
- Subunit IB, Cores 383-U1541B-6H and 7H (45–62 m CSF-A);
- Unit II, Cores 383-U1541B-8H and 9H (64–83 m CSF-A);
- Subunit IIIA, Cores 383-U1541B-12H and 13H (102–120 m CSF-A); and
- Subunit IIIB, Cores 383-U1541B-14H and 15H (121.1–138 m CSF-A).

Changes in physical properties in each lithostratigraphic unit are closely coupled to the lithofacies. In Subunit IA, generally lower GRA bulk density, lower RGB blue intensity, and higher b* values coincide with carbonate-bearing diatom oozes (Lithofacies 2) and clay-bearing biogenic oozes (Lithofacies 6). In contrast, nannofossil oozes (Lithofacies 4) show higher GRA bulk density, higher RGB blue intensity, and lower b* values. Additionally, Lithofacies 6 is associated with higher NGR and magnetic susceptibility in Subunit IA. Similar features occur in Subunit IB.

Figure F13. (A) Characteristic patterns of bioturbation across lithologic transitions and (B) selected examples of different types of bioturbation, Holes U1541B and U1541C. Ch = *Chondrites*, Pa = *Paleophycus*, P = *Planolites*, SK = *Skolithos*, TH = *Thalassinoides*, Z = *Zoophycos*. Classification follows Wetzel and Uchman (2012).

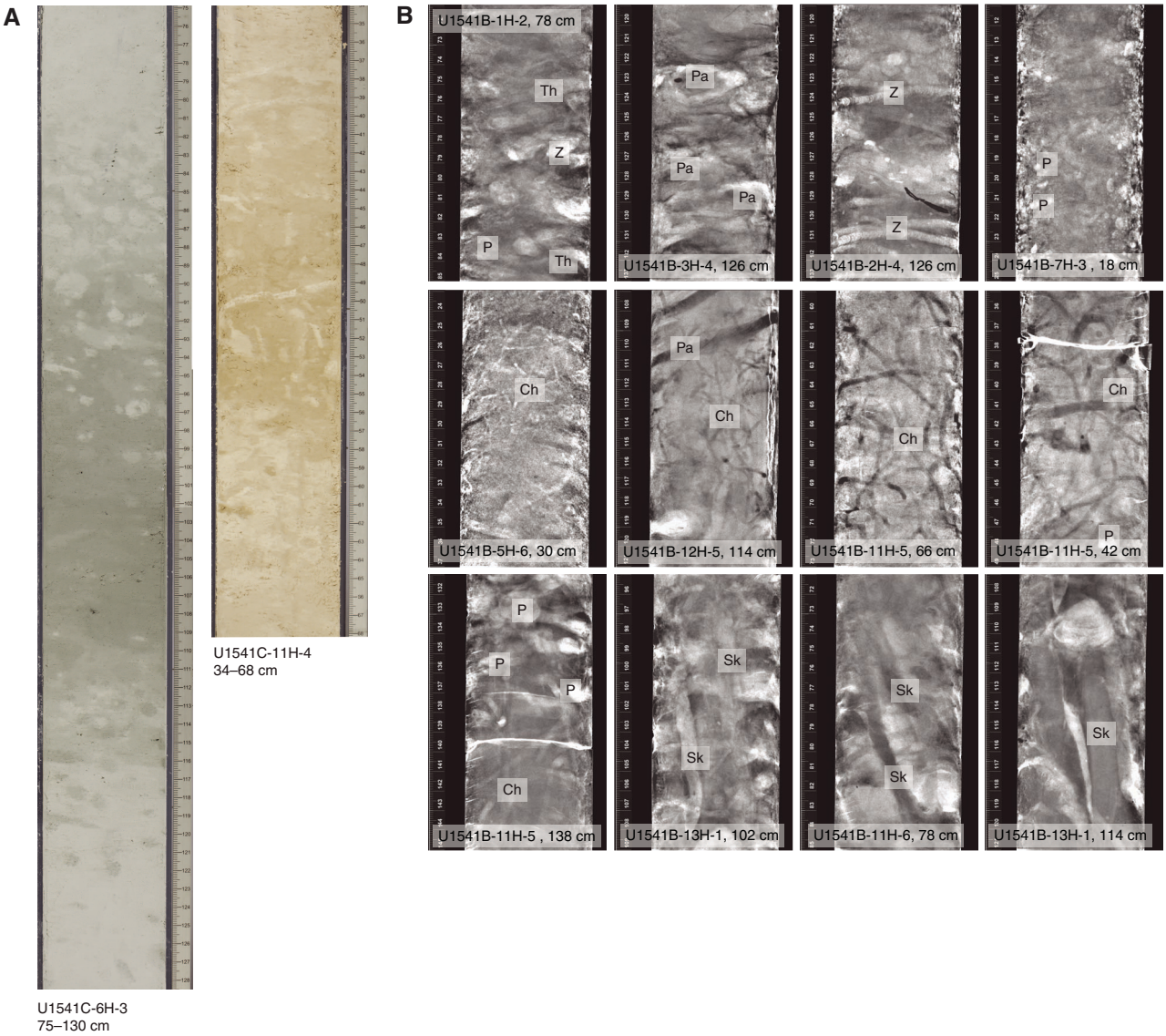

GRA bulk density values and RGB blue intensity values are generally high in Unit II, whereas b* values are generally low (Figures **F4**, **F14**). This reflects the dominance of white and light greenish gray nannofossil oozes (Lithofacies 3 and 4) and the absence of carbonate-bearing to carbonate-rich diatom oozes (Lithofacies 2). Occasional intervals of diatom-rich nannofossil oozes show opposite trends in GRA bulk density values (i.e., a decrease), RGB blue intensity values (i.e., a decrease) and b* values (i.e., an increase).

Nannofossils oozes from Subunit IIIA are characterized by high GRA bulk density values, similar to Unit II, but due to their distinct coloration (very pale brown and pale orange yellow) they show much lower RGB blue intensity values than those found in Unit II (Figure **F14**). Notable oscillations in GRA bulk density, magnetic susceptibility, NGR, and RGB blue intensity in this subunit are associated with variations between diatom-bearing and diatom-rich nannofossils/calcareous oozes. Because diatom lithologies effectively disappear in Subunit IIIB, it shows higher and less variable GRA bulk density values and RGB blue intensity values, whereas b* values can reach even lower values in Subunit IIIB compared to Subunit IIIA.

Overall, downcore changes in physical properties and spectrophotometric parameters capture alternations between lithofacies and lithologies at Site U1541 (Figure **F14**), similar to observations at Sites U1539 and U1540. This similarity is emphasized by significant positive correlations ($r^2 > 0.77$) between bulk sedimentary carbonate weight percentages and color reflectance L* intensity values, as well as RGB blue values, in Subunits IA–IIIA at Site 1541 (Figure **F15**). The insensitivity of carbonate percentage changes to variations in RGB blue intensity in Subunit IIIB, however, suggests that close to the basement at Site U1541, processes other than primary

Figure F14. A–E. Characteristic variations in major lithology and physical properties, Hole U1541B. Gray bars (A, B) = diatom ooze, light gray bars (C, D) = diatom bearing, orange bars = clay bearing. GRA = gamma ray attenuation, MS = magnetic susceptibility, NGR = natural gamma radiation, cps = counts per second, RGB = red-green-blue.

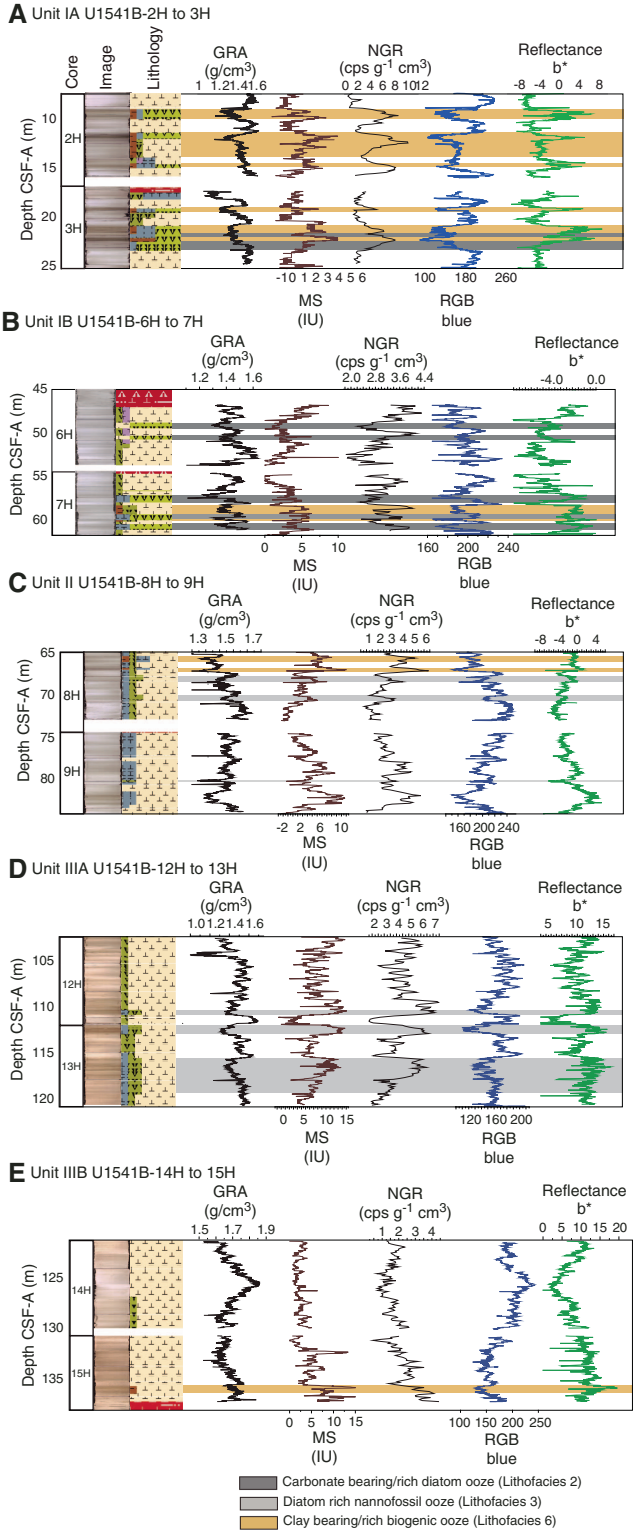

Figure F15. Relationships between bulk sedimentary carbonate content and (A) red-green-blue (RGB) blue and (B) color reflectance L*, Holes U1541A and U1541B.

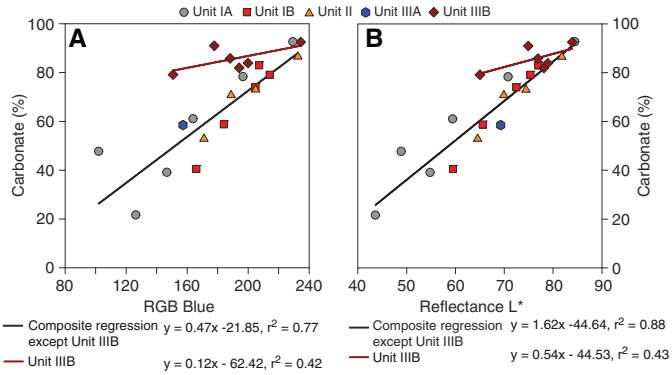

lithology control sediment color. These processes may be related to an increased abundance of authigenic Fe (hydr)oxides identified through smear slide analyses.

Summary and preliminary site interpretation

The sedimentary sequence at Site U1541 reveals marked and recurrent changes in biosiliceous and calcareous lithologies in the upper half of the core, whereas calcareous lithologies largely dominate the Pliocene/Miocene aged lower half of the core (Figures **F4**, **F5**). Recurrent alternations between (clay-bearing) biosiliceous and calcareous sediments in Subunits IA and IB (<66.65 m CCSF-A) broadly reflect glacial–interglacial changes in the export and preservation of opal and carbonate and/or the corrosiveness of bottom waters at this site. The prevalence of calcareous sediments may thus reflect increased carbonate export production and enhanced carbonate preservation at depth during interglacial climates, whereas biosiliceous lithologies suggest enhanced opal export production and/or reduced carbonate preservation at depth during glacial intervals (Figure **F9**). The change in the frequency and thickness of opal- versus carbonate-dominated sediments at the Subunit IA/IB boundary implies a transition in the pacing and duration of glacial versus interglacial periods around 1 Ma based on the Site U1541 preliminary shipboard age model (Figure **F9**) (see **Biostratigraphy**). This bears resemblance to lithologic changes at the Subunit IA/IB boundary observed at Site U1540 (see **Sedimentology** in the Site U1540 chapter [Winckler et al., 2021b]). The absence of diatom oozes in Unit II at Site U1541 (Figure **F9**) implies a warmer climate that is dominated by pelagic carbonate deposition, likely reflecting Pliocene conditions (see **Biostratigraphy**). Significantly in Unit II, sedimentation rates are ~1.3 cm/ky below ~80 m CCSF-A (~3 Ma).

The color change of carbonate-dominated lithologies at Site U1541 from white/light greenish gray to very pale brown/pale orange yellow may be due to an increased presence of Fe (hydr)oxides, possibly reflecting the proximity to basement and/or climate-related processes. The high carbonate content of Subunit IIIA and near-complete carbonate dominance in Subunit IIIB implies exceptional warmth in the Miocene–Pliocene central South Pacific region. SST reconstructions from Site U1541 sediments can thus provide important context on high-latitude Southern Hemisphere warmth over the past 8.5 My.

Average sedimentation rates based on biostratigraphy at Site U1541 above ~3 Ma are ~2.7 cm/ky on average and thus lower than at the two other pelagic central South Pacific sites drilled during Expedition 383 (Sites U1539 and U1540; see **Biostratigraphy**). With a sedimentary sequence of about 145 m CCSF-A recovered, Site U1541 sediments extend further back in time than those at Sites U1539 and U1540. Although some minor drilling gaps occur throughout the record and suck-in from contact with volcanic basement is evident at the base between 145.0 and 145.93 m CCSF-A in Hole U1541B, Site U1541 provides a near-continuous sedimentary sequence reaching back to the middle and late Miocene (~8.5 Ma). Therefore, Site U1541 may be best suited for reconstructing changes in key components of the Southern Ocean system on orbital to tectonic timescales. These components include the mean state of ACC strength and position, the latitudinal position and strength of the Southern Hemisphere westerly winds, aeolian dust supply, upwelling intensity, and the position of Southern Ocean fronts, as well as feedbacks and interactions between them. Site U1541 will thus provide a crucial Miocene-to-present perspective on the evolution of the ACC system and its climate impact and will complement higher resolution paleoclimate reconstructions based on Sites U1539 and U1540 that cover the period from the Pliocene to present.

Biostratigraphy

Core catcher samples from Site U1541 were analyzed for siliceous (diatoms, radiolarians, and silicoflagellates) and calcareous (nannofossils, foraminifers, and ostracods) microfossils. Calcareous nannofossils, planktonic and benthic foraminifers, diatoms, and silicoflagellates were also analyzed in the mudline and working-half toothpick samples. All microfossil groups of interest, diatoms, radiolarians, silicoflagellates, calcareous nannofossils, foraminifers, and ostracods, are present at Site U1541 and their abundance varies throughout the sequence. The preservation of diatoms is moderate overall. Radiolarians are generally very well preserved except for a few samples. Silicoflagellates are rare to barren throughout the core except for four samples in which they were common to abundant. Calcareous nannofossils are present throughout the sequence, and they are common to dominant in all but two of the examined samples. Planktonic and benthic foraminifers and ostracods present good to moderate preservation in the upper part of Hole U1541B and moderate preservation in the lowermost core catcher samples.

The age model at Site U1541 is mainly based on biostratigraphic analysis of Hole U1541B; additional samples from Hole U1541C were analyzed for diatoms and nannofossils. Split-core samples were taken from both holes to refine the stratigraphy in the lower half of the site. In total, 118 biostratigraphic constraints were documented, including events identified in both holes, that indicate an estimated age older than 7.95 Ma at the bottom of the sequence. The integrated biostratigraphy of diatoms, radiolarians, calcareous nannofossils, and planktonic foraminifers showed no major hiatuses at Site U1541, suggesting a continuous sequence of late Miocene–Holocene sediments with average sedimentation rates of ~1.7 cm/ky. Diatom, calcareous nannofossil, planktonic foraminifer, and radiolarian biozonations are shown in Figure **F16**. The microfossil datums recognized at this site are summarized in Table **T3** and presented as an age-depth plot in Figure **F17**. Abundances of the different microfossil groups in Hole U1541B are shown in Figures **F18** and **F19**.

Diatoms

Diatom biostratigraphy at Site U1541 is based on the analysis of 79 smear slides from 1 mudline, 15 core catcher, and 27 working-half toothpick samples taken from Hole U1541B and 36 working-half 1 cm^3 cylinder samples taken from Hole U1541C. Diatoms are common to abundant and assemblages are diverse in most samples examined (Figures **F18**, **F19**; Table **T4**); however, exceptions occur in nannofossil ooze samples where diatoms are diluted to abundances of few to barren (see **Biostratigraphy** in the Expedition 383 methods chapter [Winckler et al., 2021a] for fossil group abundance definitions). Samples with diatom abundances of few or less include 383-U1541B-1H-CC; 8H-CC; 9H-3, 50 cm; 9H-CC; 11H-1, 80 cm; 11H-3, 80 cm; 15H-1, 50 cm; 15H-CC; and 383-U1541C-2H-5, 59–60 cm. The nannofossil ooze in Samples 383-U1541B-15H-1, 50 cm, and 15H-5, 50 cm, is barren of diatoms. Preservation is moderate, and most samples exhibit low to moderate fragmentation and moderate dissolution.

The diatom assemblage compositions in both Site U1541 holes are internally consistent, and the Pliocene–recent sequence is also in good agreement with Site U1540. The diatom succession appears to record continuous accumulation from recent to the late Miocene following the Pliocene–Pleistocene diatom zonation of Zielinski and Gersonde (2002) and the Miocene zonation of Censarek and Gersonde (2002), with bottom ages approaching 8.7 Ma for Hole U1541B and older than 5.3 Ma for Hole U1541C (Table **T4**; Figure **F16**). In both holes, abundant to few occurrences of *Thalassiothrix antarctica* in the Pleistocene to early Pliocene decline to few to rare occurrences in the early Pliocene to late Miocene.

Pleistocene diatom zones

The Pleistocene sequence in the upper part of Holes U1541B (above Sample 383-U1541B-8H-2, 70 cm) and U1541C (above Sample 383-U1541C-8H-1, 90–91 cm) in the *Thalassiosira lentiginosa* Partial Range Zone is characterized by common to few *Fragilariopsis kerguelensis* and *T. lentiginosa* and few to rare *Eucampia antarctica*. The boundary between Subzones C and B, marked by the last occurrence (LO) of *Hemidiscus karstenii*, was identified in both holes in Samples 383-U1541B-1H-CC (7.00–7.06 m CSF-A) and 383-U1541C-2H-1, 59–60 cm (4.69–4.70 m CSF-A). Subzones B and A of the *T. lentiginosa* Zone, divided by the first Quaternary common occurrence of *H. karstenii*, are undifferentiated in Hole U1541B, but the boundary was identified in Hole U1541C based on the presence of *H. karstenii* in Sample 383-U1541C-2H-3, 59–60 cm (7.68–7.69 m CSF-A), and its absence in Sample 2H-5, 59–60 cm (10.27–10.28 m CSF-A). The boundary between the *T. lentiginosa* Zone and the *Actinocyclus ingens* Partial Range Zone is placed at the last common occurrence (LCO) of *A. ingens* at few or greater numbers, as observed in Samples 383-U1541B-2H-CC (15.59–15.65 m CSF-A) and 383-U1541C-3H-1, 65–66 cm (14.25–14.26 m CSF-A). In the Pleistocene sequences of both holes, *A. ingens* occurs in common to few abundance. In the *A. ingens* Zone, *Thalassiosira elliptipora* is present in Samples 383-U1541B-3H-CC (24.83–24.89 m CSF-A) and 4H-CC (35.67–35.68 m CSF-A) and discontinuously present in Samples 383-U1541C-3H-2, 65–66 cm (15.76–15.77 m CSF-A), through 5H-3, 15–16 cm (35.75–35.76 m CSF-A). Although Zielinski and Gersonde (2002) used the first abundant occurrence (FAO) of *T. elliptipora* as the boundary between Subzones C and B in the *A. ingens* Zone, the species is rare in most samples in which it occurs and has a peak abundance of few. For this reason, the two subzones have not been differentiated in the Site U1541

Figure F16. Diatom, radiolarian, calcareous nannofossil, and planktonic foraminifer zonations and biostratigraphic events, Site U1541.

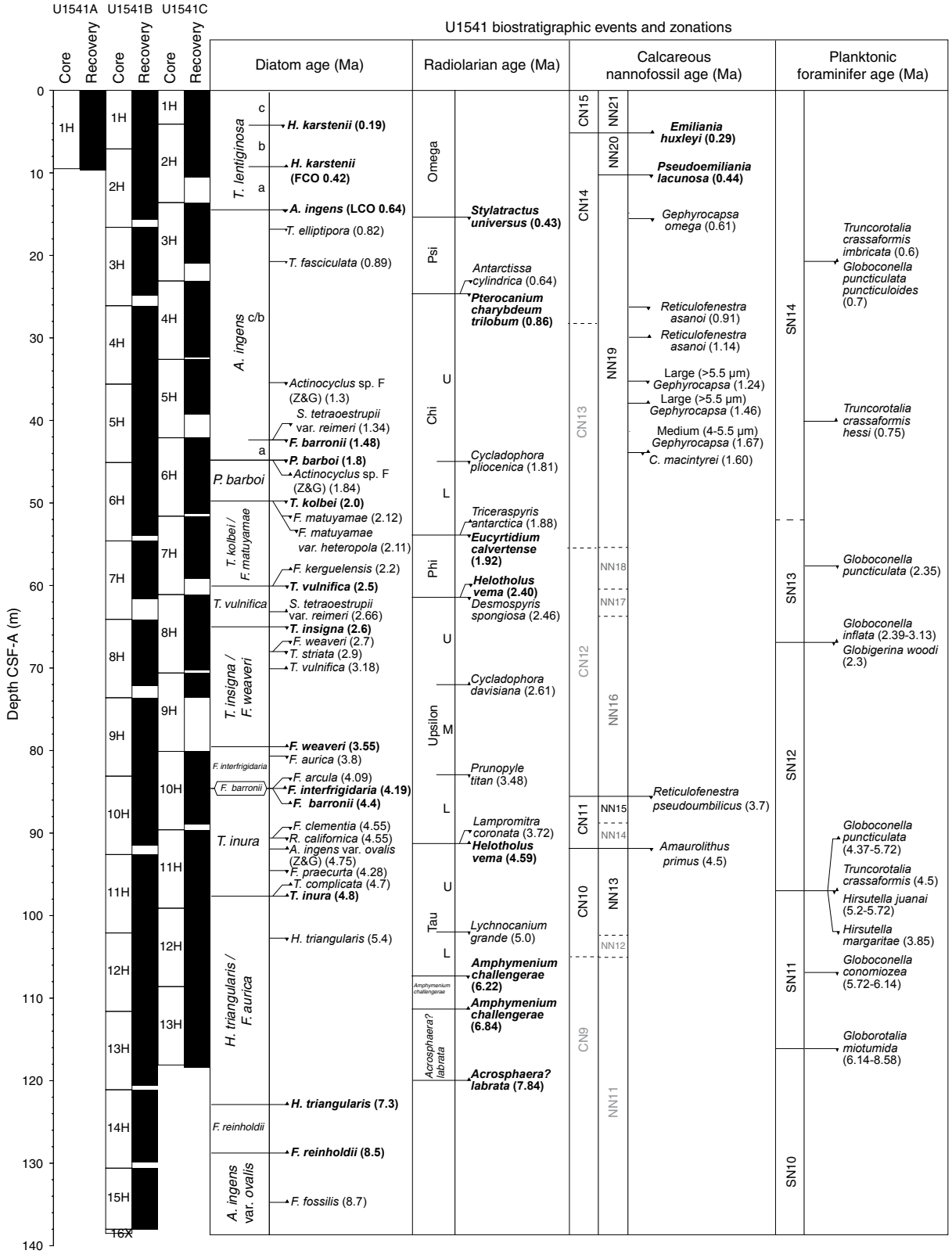

shipboard biostratigraphy and instead are combined into Subzone C/B in Figure **F16**. The LO of *Thalassiosira fasciculata* is identified in Sample 383-U1541C-4H-1, 19–20 cm (23.29–23.30 m CSF-A), but the datum is not clearly detected in Hole U1541B. The boundary between *A. ingens* Subzones B and A is defined by the LO of *Fragilariopsis barronii* and *Shionodiscus tetraoestrupii* var. *reimeri* in Samples 383-U1541B-5H-CC (45.14–45.20 m CSF-A) and 383-U1541C-6H-1, 48–49 cm (42.58–42.59 m CSF-A). The transition

from the *A. ingens* Zone to the *Proboscia barboi* Partial Range Zone is constrained by the LO of *P. barboi* in Samples 383-U1541B-5H-CC (45.14–45.20 m CSF-A) and 383-U1541C-6H-3, 48–49 cm (45.60–45.61 m CSF-A). Following the scheme of Zielinski and Gersonde (2002), the transition from the *P. barboi* Partial Range Zone to the *Thalassiosira kolbei*/*Fragilariopsis matuyamae* Concurrent Range Zone is marked by the LO of *T. kolbei* in Samples 383-U1541B-6H-2, 140 cm (48.01 m CSF-A), and 383-U1541C-7H-1, 70–71 cm (52.30–52.31 m CSF-A). The zone is further constrained by the LOs of *F. matuyamae* and *F. matuyamae* var. *heteropola* in Samples 383-U1541B-6H-CC (53.90–53.96 m CSF-A) and 383-U1541C-7H-1, 70–71 cm (52.30–52.31 m CSF-A). Long, slender varieties of *Thalassionema nitzschioides* are common to abundant in the *P. barboi* Zone and the upper portion of the *T. kolbei*/*F. matuyamae* Zone, and the LO of *F. kerguelensis* was noted in Samples 383-U1541B-6H-CC (53.90–53.96 m CSF-A) and 383-U1541C-7H-4, 90–91 cm (57.00–57.01 m CSF-A). The transition from the *T. kolbei*/*F. matuyamae* Zone to the *Thalassiosira vulnifica* Partial Range Zone is constrained by the LO of *T. vulnifica*. In Hole U1541B, the species was identified in only a single sample (383-U1541B-7H-CC; 61.54–61.70 m CSF-A), and it is absent from the samples above and below. In Hole U1541C, *T. vulnifica* is present in three consecutive samples, and the LO was identified in Sample 383-U1541C-8H-1, 90–91 cm (62.00–62.01 m CSF-A). The *T. vulnifica* Partial Range Zone, which has an age between 2.5 and 2.6 Ma, marks the transition from the early Pleistocene to the late Pliocene. Notably, the LO of *Fragilariopsis interfrigidaria*, which is usually found in the *T. vulnifica* Zone, is poorly defined at Site U1541 and was observed much

Table T3. Chronostratigraphic constraints at Site U1541. Event datum type: D = diatom, R = radiolarian, N = calcareous nannofossil, F = planktonic foraminifer. FO = first occurrence, FCO = first common occurrence, LO = last occurrence, LCO = last common occurrence, LAO = last abundant occurrence. * = datums applied with lower confidence based on preservation, age, or depth uncertainty. References: AO = Anthonissen and Ogg (2012), B = Bohaty et al. (1998), B04 = Bylinskaya (2004), C = Cody et al. (2008) average range model, CG = Censarek and Gersonde (2002), CP = Chaisson and Pearson (1997), G = Gersonde (1989), HM = Harwood and Maruyama (1992), KS = Kennett and Srinivasan (1983), L = Lazarus (1992), O = Ogg (2012), S07 = Scott et al. (2007), S = Sjunneskog et al. (2012), T = Tauxe et al. (2012), W = Winter et al., 2012, W94 = Wei (1994), W11 = Wade et al. (2011), ZG = Zielinski and Gersonde (2002), 181 = ODP Leg 181 Initial Reports (2000), 374 = IODP Expedition 374 diatom and radiolarian biostratigraphic frameworks (David Harwood and Giuseppe Cortese, pers. comm.), 383 = regional datum age revised for IODP Expedition 383. (Continued on next two pages.) **Download table in CSV format.**

Constraint number	Type	Bioevent	Age (Ma)	Top core, section, interval (cm)	Top depth CSF-A (m)	Bottom core, section, interval (cm)	Bottom depth CSF-A (m)	Reference
				383-U1541B-		383-U1541B-		
1	D	LO *Hemidiscus karstenii*	0.19	1H-1, 0	0.00	1H-CC, 0–6	7.00–7.06	HM, ZG
2	N	FO *Emiliania huxleyi*	0.29	1H-CC, 0–6	5.01–5.06	1H-CC, 0–6	7.00–7.06	AO
3	R	LO *Stylatractus universus*	0.43	1H-CC, 0–6	7.00–7.06	2H-CC, 8–14	15.59–15.65	L, 374
4	D	LCO *Actinocyclus ingens*	0.64	1H-CC, 0–6	7.00–7.06	2H-CC, 0–6	15.59–15.65	HM, 374
5	N	LO *Pseudoemiliania lacunosa*	0.44	2H-1, 90	8.00	2H-3, 114	10.50	AO
6	N	LO *Gephyrocapsa omega*	0.61	2H-5, 100	13.23	2H-6, 115	14.87	AO
7	R	LO *Antarctissa cylindrica*	0.64	2H-CC, 8–14	15.59–15.65	3H-CC, 35–41	24.83–24.89	L, 374
8	R	LO *Pterocanium charybdeum trilobum*	0.86	2H-CC, 8–14	15.59–15.65	3H-CC, 35–41	24.83–24.89	L, 374
9	F	FO *Truncorotalia crassaformis imbricata*	0.64	2H-CC, 8–14	15.59–15.65	3H-CC, 35–41	24.83–24.89	B04
10	F	LO *Globoconella puncticulata puncticuloides*	0.7	2H-CC, 8–14	15.59–15.65	3H-CC, 35–41	24.83–24.89	SO7, 374
11	D	LO *Thalassiosira elliptipora*	0.82	2H-CC, 8–14	15.59–15.65	3H-CC, 35–41	24.83–24.89	ZG
12	N	LO *Reticulofenestra asanoi*	0.91	3H-4, 26	20.30	3H-6, 80	23.79	AO
13	D	LO *Actinocyclus* sp. F (Z&G)	1.2–1.42	3H-CC, 35–41	24.83–24.89	4H-CC, 14–20	35.67–35.73	C, ZG
14	N	FO *Reticulofenestra asanoi*	1.14	3H-CC, 35–41	24.83–24.89	4H-CC, 14–20	35.67–35.73	AO
15	N	LO *Gephyrocapsa* large (>5.5 µm)	1.24	3H-CC, 35–41	24.83–24.89	4H-CC, 14–20	35.67–35.73	AO
16	R	LO *Cycladophora pliocenica*	1.81	4H-CC, 14–20	35.67–35.73	5H-CC, 10–16	45.14–45.20	L, 374
17	F	FO *Truncorotalia crassaformis hessi*	0.75	4H-CC, 14–20	35.67–35.73	5H-CC, 10–16	45.14–45.20	AO
18	D	LO *Shionodiscus tetraoestrupii* var. *reimeri*	1.31–1.34	4H-CC, 14–20	35.67–35.73	5H-CC, 10–16	45.14–45.20	C, ZG
19	D	LO *Fragilariopsis barronii*	1.19–1.48	4H-CC, 14–20	35.67–35.73	5H-CC, 10–16	45.14–45.20	C, ZG
20	D	LO *Proboscia barboi*	1.6–1.82	4H-CC, 14–20	35.67–35.73	5H-CC, 10–16	45.14–45.20	C, ZG
21	D	FO *Actinocyclus* sp. F (Z&G)	1.84–2.34	4H-CC, 14–20	35.67–35.73	5H-CC, 10–16	45.14–45.20	C, ZG
22	N	LO *Helicosphaera sellii*	1.26–1.34	4H-CC, 14–20	35.67–35.73	5H-CC, 10–16	45.14–45.20	AO
23	N	LO *Calcidiscus macintyrei*	1.6	4H-CC, 14–20	35.67–35.73	5H-CC, 10–16	45.14–45.20	AO
24	N	FO *Gephyrocapsa* medium (4–5.5 µm)	1.67	4H-CC, 14–20	35.67–35.73	5H-CC, 10–16	45.14–45.20	AO
25	R	FO *Triceraspyris antarctica*	1.88	5H-CC, 10–16	45.14–45.20	6H-CC, 0–6	53.90–53.96	L, 374
26	R	LO *Eucyrtidium calvertense*	1.92	5H-CC, 10–16	45.14–45.20	6H-CC, 0–6	53.90–53.96	L, 374
27	D	LO *Thalassiosira kolbei*	1.98–2.08	5H-CC, 10–16	45.14–45.20	6H-2, 140	48.01	C, ZG
28	D	LO *Fragilariopsis matuyamae*	2–2.12	6H-4, 140	51.01	6H-CC, 0–6	53.90–53.96	C, ZG, 374
29	D	LO *Fragilariopsis matuyamae* var. *heteropola*	2.08–2.11	6H-4, 140	51.01	6H-CC, 0–6	53.90–53.96	C
30	R	LO *Helotholus vema*	2.4	6H-CC, 0–6	53.90–53.96	7H-CC, 34–40	61.64–61.70	L, 374
31	R	LO *Desmospyris spongiosa*	2.46	6H-CC, 0–6	53.90–53.96	7H-CC, 34–40	61.64–61.70	L, 374
32	F	LO *Globoconella puncticulata*	1.88–2.39	6H-CC, 0–6	53.90–53.96	7H-CC, 34–40	61.64–61.70	W94
33	D	FO *Fragilariopsis kerguelensis*	1.95–2.2	6H-CC, 0–6	53.90–53.96	7H-2, 70	56.81	C, ZG
34	D	LO *Thalassiosira vulnifica*	2.2–2.56	7H-4, 70	59.81	7H-CC, 34–40	61.64–61.70	HM, ZG, 374
35	R	FO *Cycladophora davisiana*	2.61	7H-CC, 34–40	61.64–61.70	8H-CC, 10–16	72.09–72.15	L, 374
36	F	FO *Globoconella inflata*	2.39–3.13	7H-CC, 34–40	61.64–61.70	8H-CC, 10–16	72.09–72.15	W94
37	F	LO *Globigerina woodi*	2.3	7H-CC, 34–40	61.64–61.70	8H-CC, 10–16	72.09–72.15	AO
38	D	LO *Thalassiosira insigna*	2.45–2.6	7H-CC, 34–40	61.64–61.70	8H-2, 70	66.30	C, 374
39	D	FO *Thalassiosira vulnifica**	3.14–3.18	7H-CC, 34–40	61.64–61.70	8H-2, 70	66.30	C
40	D	LO *Fragilariopsis weaveri*	2.54–2.66	8H-2, 70	66.30	8H-4, 70	69.30	ZG
41	R	LO *Prunopyle titan*	3.48	8H-CC, 10–16	72.09–72.15	9H-CC, 11–17	82.98–83.04	L,374

Table T3 (continued). (Continued on next page.)

Constraint number	Type	Bioevent	Age (Ma)	Top core, section, interval (cm)	Top depth CSF-A (m)	Bottom core, section, interval (cm)	Bottom depth CSF-A (m)	Reference
42	D	LO *Thalassiosira striata*	2.89–2.96	8H-CC, 10–16	72.09–72.15	9H-1, 50	74.10	C, HM
43	D	FO *Thalassiosira lentiginosa**	2.89–4.11	8H-CC, 10–16	72.09–72.15	9H-1, 50	74.10	C, HM
44	D	LO *Fragilariopsis interfrigidaria**	2.58–2.96	9H-3, 50	77.10	9H-6, 50	81.61	ZG
45	D	FO *Fragilariopsis weaveri*	3.51–3.55	9H-3, 50	77.10	9H-6, 50	81.61	C, ZG
46	D	LO *Fragilariopsis aurica*	3.37–4.35	9H-3, 50	77.10	9H-6, 50	81.61	C, HM, ZG
47	R	LO *Lampromitra coronata*	3.72	9H-CC, 11–17	82.98–83.04	10H-CC, 0–6	91.41–91.47	L, 374
48	R	FO *Helotholus vema*	4.59	9H-CC, 11–17	82.98–83.04	10H-CC, 0–6	91.41–91.47	L, 374
49	D	LO *Fragilariopsis arcula*	3.84–4.09	9H-CC, 11–17	82.98–83.04	10H-1, 50	83.60	C, ZG
50	D	FO *Fragilariopsis interfrigidaria*	3.9–4.19	10H-1, 50	83.60	10H-3, 50	86.60	C, 374
51	D	FO *Fragilariopsis barronii*	4.28–4.45	10H-1, 50	83.60	10H-3, 50	86.60	C, 374
52	N	LO *Reticulofenestra pseudoumbilicus*	3.7	10H-1, 70	83.80	10H-2, 90	85.50	AO
53	D	FO *Thalassiosira inura**	4.71–4.77	10H-3, 50	86.60	10H-5, 50	89.52	C
54	D	LO *Rouxia californica*	4.29–4.82	10H-5, 50	89.52	10H-CC, 0–6	91.41–91.47	C
55	N	LO *Amaurolithus primus*	4.5	10H-5, 74	89.76	10H-CC, 0–6	91.41–91.47	AO
56	R	LO *Lychnocanium grande*	5	10H-CC, 0–6	91.41–91.47	11H-CC, 29–35	102.03–102.09	L, 374
57	F	FO *Globoconella puncticulata*	4.37–5.72	10H-CC, 0–6	91.41–91.47	11H-CC, 29–35	102.03–102.09	W94
58	F	LO *Hirsutella juanai*	5.2–5.72	10H-CC, 0–6	91.41–91.47	11H-CC, 29–35	102.03–102.09	CP, W11
59	F	LO *Hirsutella margaritae*	3.85	10H-CC, 0–6	91.41–91.47	11H-CC, 29–35	102.03–102.09	AO
60	F	FO *Truncorotalia crassaformis*	4.5	10H-CC, 0–6	91.41–91.47	11H-CC, 29–35	102.03–102.09	AO
61	D	LO *Actinocyclus ingens* var. *ovalis*	4.75–6.81	10H-CC, 0–6	91.41–91.47	11H-1, 80	93.40	C
62	R	LO *Amphymenium challengerae*	6.22	11H-CC, 29–35	102.03–102.09	12H-CC, 10–16	111.54–111.60	L, 374
63	F	LO *Globoconella conomiozea*	5.72–6.14	11H-CC, 29–35	102.03–102.09	12H-CC, 10–16	111.54–111.60	W94
64	D	LO *Hemidiscus triangularis*	5.13–5.4	11H-CC, 29–35	102.03–102.09	12H-1, 50	102.60	CG, 374
65	D	LO *Thalassiosira convexa* var. *aspinosa*	5.19–6.64	11H-CC, 29–35	102.03–102.09	12H-1, 50	102.60	C, CG
66	D	LO *Denticulopsis hustedtii*	5.6–6.3	12H-6, 50	110.12	12H-CC, 10–16	111.54–111.60	HM
67	R	FO *Amphymenium challengerae*	6.84	12H-CC, 10–16	111.54–111.60	13H-CC, 25–31	120.55–120.61	L, 374
68	F	LO *Globorotalia miotumida*	6.14–8.58	12H-CC, 10–16	111.54–111.60	13H-CC, 25–31	120.55–120.61	W94, KS
69	D	LO *Actinocyclus ellipticus*	5.14–7.78	13H-1, 50	112.10	13H-3, 50	115.12	C
70	R	FO *Acrosphaera? labrata*	7.84	13H-CC, 25–31	120.55–120.61	14H-CC, 0–6	129.85–129.91	L, 374
71	D	FO *Hemidiscus triangularis*	6.14–7.3	14H-1, 50	121.60	14H-3, 50	124.55	C, CG
72	D	FO *Fragilariopsis reinholdii*	7.96–8.5	14H-5, 50	127.51	14H-CC, 0–6	129.85–129.91	CG, 374
73	D	FO *Fragilariopsis cylindrica**	7.7	14H-CC, 0–6	129.85–129.91	15H-1, 50	131.10	374
74	D	FO *Fragilariopsis fossilis**	8.37–8.7	15H-1, 50	131.10	15H-CC, 0–7	137.98–138.04	C, 374
				383-U1541C-		383-U1541C-		
75	D	LO *Hemidiscus karstenii*	0.19	1H-2, 35–36	1.84–1.85	2H-1, 59–60	4.69–4.70	HM, ZG
76	D	LCO *Actinocyclus ingens*	0.64	2H-5, 59–60	14.25–14.26	3H-1, 65–66	14.25–14.26	ZG
77	D	LO *Thalassiosira elliptipora*	0.82	3H-1, 65–66	14.25–14.26	3H-2, 65–66	15.76–15.77	ZG
78	D	LO *Thalassiosira fasciculata*	0.87–0.89	3H-4, 19–20	18.76–18.77	4H-1, 19–20	23.29–23.30	C, ZG
79	N	LO *Reticulofenestra asanoi*	0.91	4H-1, 60	23.70	4H-4, 20	27.82	AO
80	N	FO *Reticulofenestra asanoi*	1.14	4H-6, 40	31.02	5H-2, 57	34.67	AO
81	N	LO *Gephyrocapsa* large (>5.5 µm)	1.24	4H-6, 40	31.02	5H-2, 57	34.67	AO
82	D	FO *Fragilariopsis separanda**	1.37–1.45	5H-1, 15–16	32.75–32.76	5H-3, 15–16	35.75–35.76	C
83	N	FCO *Gephyrocapsa* large (>5.5 µm)	1.46	5H-4, 35	37.45	6H-1, 83	42.93	AO
84	D	LO *Actinocyclus* sp. F (Z&G)	1.2–1.42	5H-5, 15–16	38.36–38.37	6H-1, 48–49	42.58–42.59	C, ZG
85	D	LO *Shionodiscus tetraoestrupii* var. *reimeri*	1.31–1.34	5H-5, 15–16	38.36–38.37	6H-1, 48–49	42.58–42.59	C, ZG
86	D	LO *Fragilariopsis barronii*	1.19–1.48	5H-5, 15–16	38.36–38.37	6H-1, 48–49	42.58–42.59	C, ZG
87	D	LO *Proboscia barboi*	1.6–1.82	6H-1, 48–49	42.58–42.59	6H-3, 48–49	45.60–45.61	C, ZG
88	D	FO *Actinocyclus* sp. F (Z&G)	1.84–2.34	6H-1, 48–49	42.58–42.59	6H-3, 48–49	45.60–45.61	C, ZG
89	N	LO *Calcidiscus macintyrei*	1.6	6H-2, 125	44.86	6H-4, 69	45.81	AO
90	N	FO *Gephyrocapsa* medium (4–5.5 µm)	1.67	6H-2, 125	44.86	6H-4, 69	45.81	AO
91	D	LO *Thalassiosira kolbei*	1.98–2.08	6H-5, 48–49	48.60–48.61	7H-1, 70–71	52.30–52.31	C, ZG
92	D	LO *Fragilariopsis matuyamae*	2–2.12	6H-5, 48–49	48.60–48.61	7H-1, 70–71	52.30–52.31	C, ZG, 374
93	D	LO *Fragilariopsis matuyamae* var. *heteropola*	2.08–2.11	6H-5, 48–49	48.60–48.61	7H-1, 70–71	52.30–52.31	C
94	D	FO *Fragilariopsis kerguelensis*	1.95–2.2	7H-4, 90–91	57.00–57.01	8H-1, 90–91	62.00–62.01	C, ZG
95	D	LO *Thalassiosira vulnifica*	2.2–2.56	7H-4, 90–91	57.00–57.01	8H-1, 90–91	62.00–62.01	HM, ZG, 374
96	D	LCO *Thalassiosira inura**	2.53–2.65	7H-4, 90–91	57.00–57.01	8H-1, 90–91	62.00–62.01	C, ZG
97	D	FO *Shionodiscus tetraoestrupii* var. *reimeri*	2.3–2.66	8H-1, 90–91	62.00–62.01	8H-3, 35–36	64.45–64.46	C, ZG, 374
98	D	LO *Thalassiosira insigna*	2.45–2.6	8H-3, 35–36	64.45–64.46	8H-5, 70–71	67.81–67.82	C, 374
99	D	LO *Thalassiosira complicata**	3.36–3.44	8H-3, 35–36	64.45–64.46	8H-5, 70–71	67.81–67.82	C
100	D	LO *Fragilariopsis weaveri*	2.54–2.66	8H-5, 70–71	67.81–67.82	9H-1, 60–61	71.20–71.21	ZG
101	D	LO *Thalassiosira striata*	2.89–2.96	8H-5, 70–71	67.81–67.82	9H-1, 60–61	71.20–71.21	C, HM
102	D	FO *Thalassiosira vulnifica*	3.14–3.18	8H-5, 70–71	67.81–67.82	9H-1, 60–61	71.20–71.21	C
103	D	LO *Fragilariopsis interfrigidaria**	2.58–2.96	9H-1, 60–61	71.20–71.21	10H-1, 70–71	80.80–80.81	ZG
104	D	FO *Fragilariopsis weaveri*	3.51–3.55	9H-1, 60–61	71.20–71.21	10H-1, 70–71	80.80–80.81	C, ZG
105	D	LO *Fragilariopsis aurica*	3.37–4.35	10H-1, 70–71	80.80–80.81	10H-3, 10–11	81.93–81.94	C, HM, ZG
106	D	LO *Fragilariopsis arcula*	3.84–4.09	10H-3, 10–11	81.93–81.94	10H-6, 110–111	87.43–87.44	C, ZG
107	D	FO *Fragilariopsis interfrigidaria*	3.9–4.19	10H-6, 110–111	87.43–87.44	11H-1, 20–21	89.80–89.81	C, 374
108	D	FO *Fragilariopsis barronii*	4.28–4.45	10H-6, 110–111	87.43–87.44	11H-1, 20–21	89.80–89.81	C, 374
109	D	LO *Actinocyclus ingens* var. *ovalis*	4.75–6.81	10H-6, 110–111	87.43–87.44	11H-1, 20–21	89.80–89.81	C

Table T3 (continued).

Constraint number	Type	Bioevent	Age (Ma)	Top core, section, interval (cm)	Top depth CSF-A (m)	Bottom core, section, interval (cm)	Bottom depth CSF-A (m)	Reference
110	D	LO *Fragilariopsis clementia*	4.51–4.6	11H-1, 20–21	89.80–89.81	11H-3, 20–21	92.80–92.81	C, 374
111	F	LO *Hirsutella margaritae*	3.85	Constrained in Hole U1541B only	—	11H-6, 75–76	97.84–97.85	AO
112	D	LO *Fragilariopsis praecurta*	4.19–4.28	11H-3, 20–21	92.80–92.81	11H-5, 20–21	95.78–95.79	C, 374
113	D	FO *Thalassiosira complicata*	4.64–4.71	11H-5, 20–21	95.78–95.79	12H-1, 70–71	99.80–99.81	C
114	D	FO *Thalassiosira inura*	4.71–4.85	11H-5, 20–21	95.78–95.79	12H-1, 70–71	99.80–99.81	C, 374
115	D	LO *Hemidiscus triangularis*	5.13–5.4	11H-5, 20–21	95.78–95.79	12H-1, 70–71	99.80–99.81	CG, 374
116	D	LO *Thalassiosira convexa* var. *aspinosa*	5.19–6.64	11H-5, 20–21	95.78–95.79	12H-1, 70–71	99.80–99.81	C, CG
117	D	FO *Fragilariopsis clementia**	6.35–7.7	11H-5, 20–21	95.78–95.79	12H-1, 70–71	99.80–99.81	C
118	D	FO *Fragilariopsis cylindrica**	7.7	13H-1, 50–51	109.10–109.11	13H-2, 90–91	111.00–111.01	374

Figure F17. Age-depth plot, Site U1541.

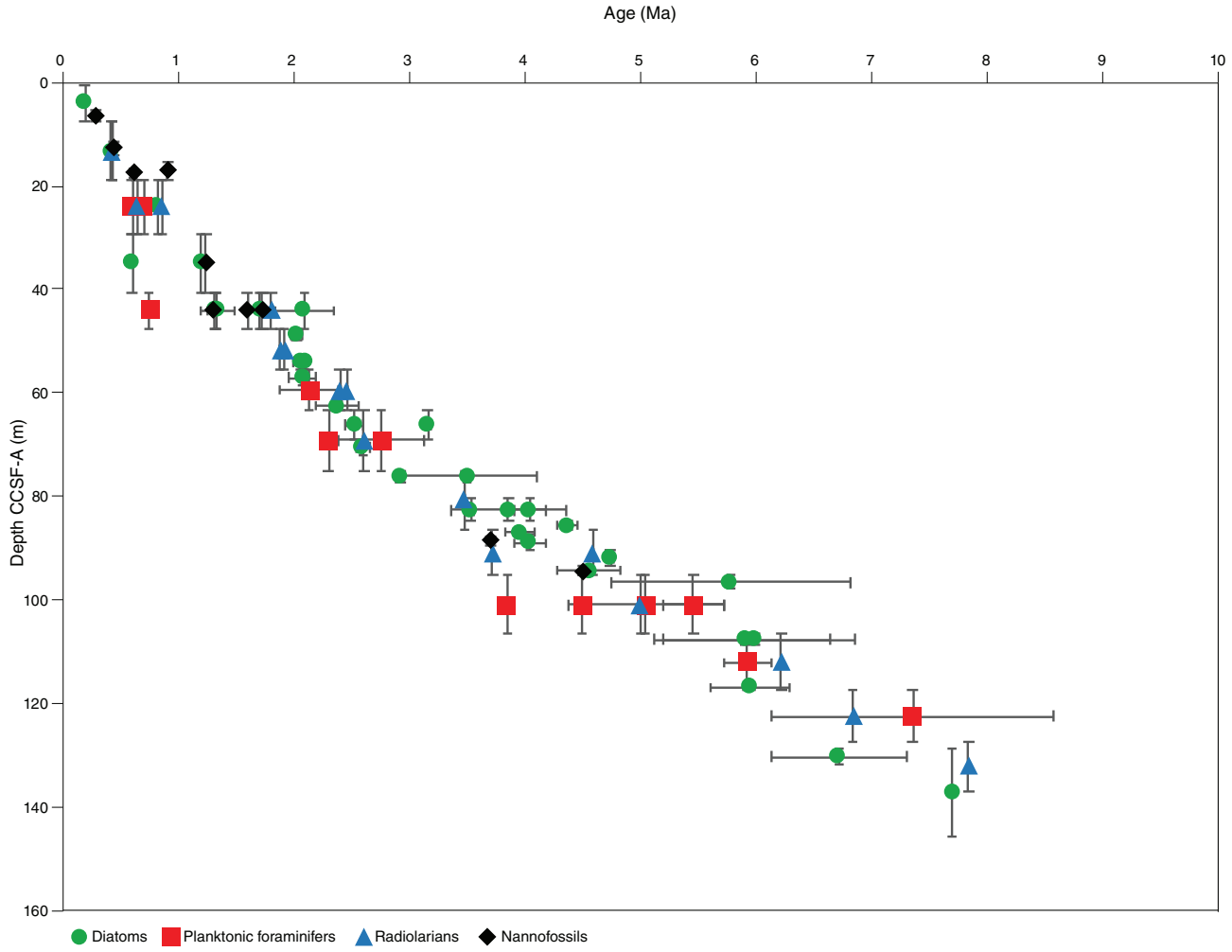

deeper in the section than predicted from its regional last appearance datum (LAD) (Cody et al., 2008; Zielinski and Gersonde, 2002). This discrepancy may be ecological but may also reflect plasticity of taxonomic concepts within the *Fragilariopsis praeinterfrigidaria* lineage (Riesselman, 2012), of which diverse morphologies were observed in the Pliocene interval of Hole U1541B.

Pliocene diatom zones

The Pliocene sequence in the middle part of Holes U1541B (Samples 383-U1541B-8H-2, 70 cm, to 12H-1, 50 cm) and U1541C (Samples 383-U1541C-8H-1, 90–91 cm, through 11H-5, 20–21 cm) is characterized by common to rare *F. barronii, Hemidiscus cuneiformis*, and diverse *T. nitzschioides* varieties, and by few to rare *A. ingens*, indicating a warmer marine environment than that recorded

Figure F18. Distribution of siliceous and calcareous microfossils, Hole U1541B. B = barren, R = rare, F = few, C = common, A = abundant, D = dominant. Ostracods reported as number of valves per sample (>125 mm fraction)

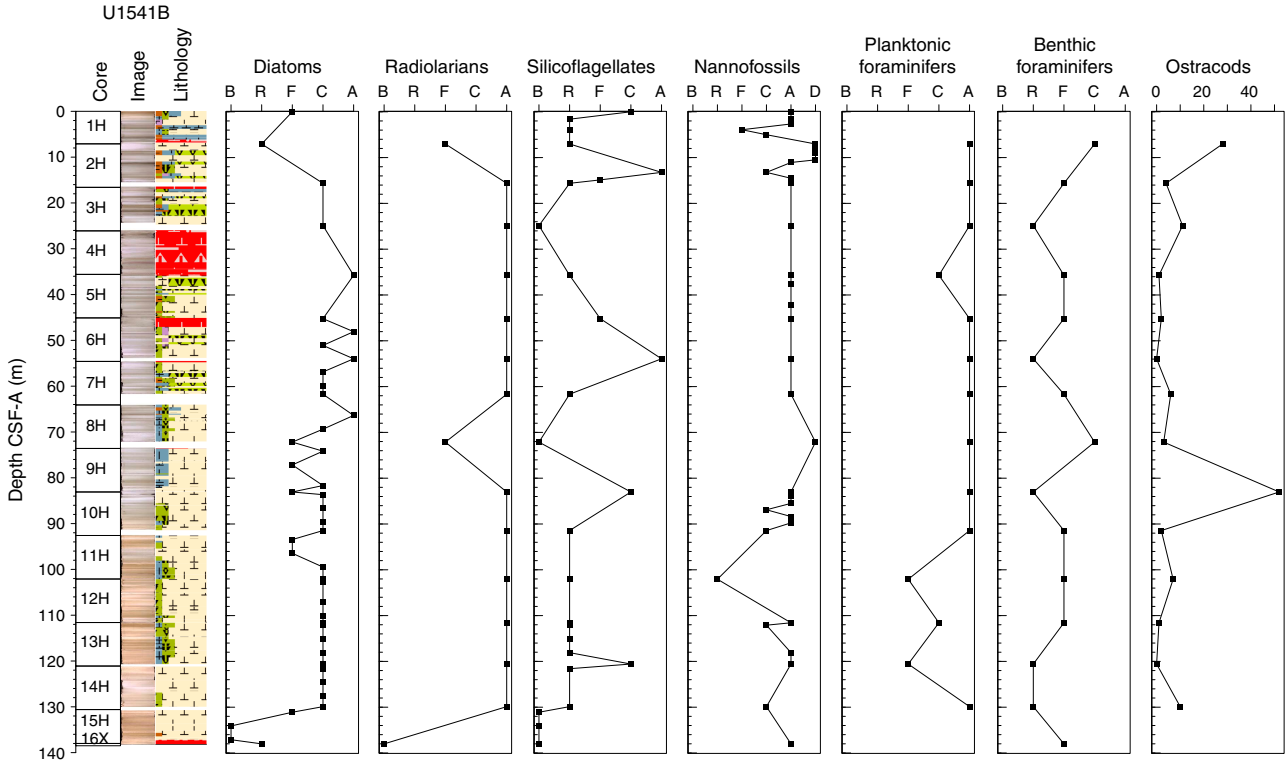

Figure F19. Distribution of diatoms and nannofossils, Hole U1541C. B = barren, R = rare, F = few, C = common, A = abundant, D = dominant.

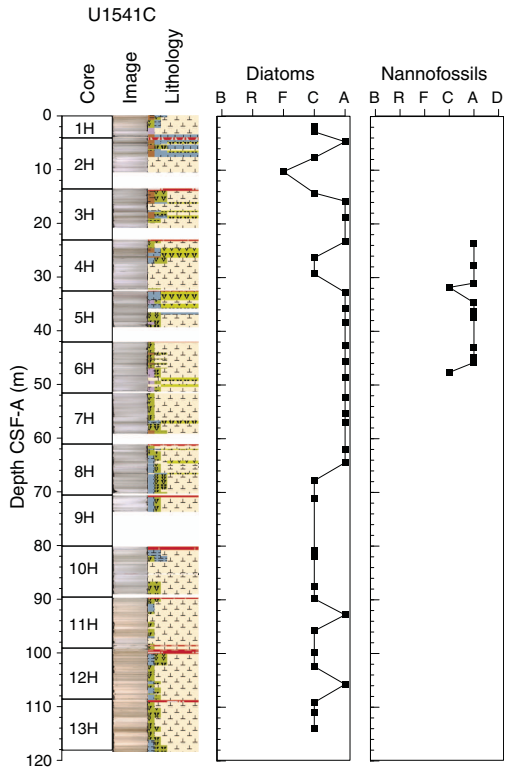

Table T4. Distribution chart of diatoms, Holes U1541B and U1541C. **Download table in CSV format.**

during the Pleistocene. The LO of *Thalassiosira inura* is not well defined in Hole U1541B but was clearly observed in Sample 383-U1541C-8H-1, 90–91 cm (62.00–62.01 m CSF-A). The transition from the *T. vulnifica* Zone to the *Thalassiosira insigna*/*Fragilariopsis weaveri* Concurrent Range Zone is constrained by the LO of *T. insigna* in Samples 383-U1541B-8H-2, 70 cm (66.30 m CSF-A), and 383-U1541C-8H-5, 70–71 cm (67.81–67.82 m CSF-A). Below, the base of the zone is marked by the first occurrence (FO) of *F. weaveri* in Samples 383-U1541B-9H-3, 50 cm (77.10 m CSF-A), and 383-U1541C-9H-1, 60–61 cm (71.20–71.21 m CSF-A). In this zone, the LO of *Thalassiosira complicata* is clearly defined only in Sample 383-U1541C-8H-5, 70–71 cm (67.81–67.82 m CSF-A), whereas the LO of *Thalassiosira striata* was found in Samples 383-U1541B-9H-1, 50 cm (74.10 m CSF-A), and 383-U1541C-9H-1, 60 cm (71.20–71.21 m CSF-A), and the LO of *Fragilariopsis aurica* was identified in Samples 383-U1541B-9H-6, 50 cm (81.61 m CSF-A), and 383-U1541C-10H-3, 10–11 cm (81.93–81.94 m CSF-A). Below, the *F. interfrigidaria* Partial Range Zone is constrained at the top by the FO of *F. weaveri* (described above) and at the bottom by the FO of *F. interfrigidaria* in Samples 383-U1541B-10H-1, 50 cm (83.60 m CSF-A), and 383-U1541C-10H-6, 110–111 cm (87.43–87.44 m CSF-A). Within this zone, the LO of *Fragilariopsis arcula* is in Samples 383-U1541B-10H-1, 50 cm (83.60 m CSF-A), and 383-U1541C-10H-6, 110–111 cm (87.43–87.44 m CSF-A). Below the *F. interfrigidaria* Zone, the top of the *F. barronii* Partial Range Zone should be constrained by the FO of *F. interfrigidaria* (described above), and

the bottom of the zone should be constrained by the FO of *F. barronii*. However, these two events were found in the same samples in both holes (383-U1541B-10H-1, 50 cm [83.60 cm CSF-A], and 383-U1541C-10H-6, 110–111 cm [87.43–87.44 m CSF-A]) (Tables **T3**, **T4**). Based on the complete sequence of magnetic reversals recovered at Site U1541 (see **Paleomagnetism**), we interpret this co-occurrence of datums not as a hiatus but instead as an indication that the sedimentary sequence containing the *F. barronii* Zone is very condensed at Site U1541, and we expect the zonal boundaries to be refined by higher resolution postcruise characterization. Below the *F. barronii* Zone, the boundary at the base of the *T. inura* Partial Range Zone is constrained by the FO of *T. inura* in Sample 383-U1541C-11H-5, 20–21 cm (95.78–95.79 m CSF-A), but it is not clearly defined in Hole U1541B. Within the *T. inura* Zone, the LO of *Fragilariopsis cylindrica* was noted in Samples 383-U1541B-11H-5, 80 cm (99.41 m CSF-A), and 383-U1541C-11H-3, 20–21 cm (92.80–92.81 m CSF-A), whereas the LO of *Fragilariopsis clementia* was found only in Sample 383-U1541C-11H-3, 20–21 cm (92.80–92.81 m CSF-A). The LO of *A. ingens* var. A sensu Harwood and Matuyama (1992) was also noted in this zone in Samples 383-U1541B-11H-5, 80 cm (99.41 m CSF-A), and 383-U1541C-11H-1, 20–21 cm (89.80–89.81 m CSF-A), and coincides with the LCO of *Azpeitia nodulifer*. *A. ingens* var. A persists through the base of both holes, sometimes co-occurring with specimens tabulated as *A. ingens* var. *ovalis* sensu Gersonde (1990) (Table **T4**), which have an oval valve outline but are otherwise very similar in appearance. Noting the ongoing taxonomic debate regarding differentiation of *A. ingens* var. A sensu Harwood and Maruyama (1992), *A. ingens* var. *ovalis* sensu Gersonde (1990), and *Hemidiscus ovalis* sensu Harwood and Maruyama (1992), we have lumped all morphologies into a single category for biostratigraphic purposes and applied the datum age of Cody et al. (2008) for *A. ingens* var. *ovalis*. The LO of *Denticulopsis hustedtii* also occurs in the *T. inura* Zone in Sample 383-U1541C-11H-1, 20–21 (89.80–89.81 m CSF-A). Finally, in the *T. inura* Zone, the core catcher from Core 383-U1541B-10H contains a distinct assemblage relative to all other samples examined that has diverse morphologies (both established species and unidentified variants) in the genera *Azpeitia, Coscinodiscus*, and *Thalassionema*.

Miocene diatom zones

The upper Miocene sequence in the lower part of Holes U1541B (below Sample 12H-4, 50 cm) and U1541C (below Sample 12H-1, 70–71 cm) is characterized by common to rare *A. ingens, T. nitzschioides* (long, thin varieties), and *T. nitzschioides* var. *parva* and by few to rare *H. cuneiformis* and *Proboscia* sp., suggesting Miocene water temperatures that were even warmer than those in the Pliocene. The persistent presence of *Denticulopsis dimorpha* was noted in both holes from the base of the sequence to the lower Pliocene. The transition from the *T. inura* Zone above into the *Hemidiscus triangularus/F. aurica* Zone below is constrained by the FO of *H. triangularus* in Sample 383-U1541B-12H-1, 50 cm (102.60 m CSF-A). The diatom assemblage in the lowermost sample analyzed from Hole U1541C, 13H-4, 90–91 cm (114.04–114.05 m CSF-A), still includes trace occurrences of *H. triangularus*, which constrains the bottom age of Hole U1541C to younger than 7.3 Ma. The zone is further characterized by the co-occurrence of few to rare *Thalassiosira convexa* var. *aspinosa* and *F. praeinterfrigidaria*. The bottom of the zone is constrained by the FO of *H. triangularus* in Sample 383-U1541B-14H-1, 50 (121.60 m CSF-A). Below the *H. triangularus*/*F. aurica* Zone, the upper boundary of the *Fragilariopsis reinholdii* Partial Range Zone of Censarek and Gersonde (2002) is defined by the FO of *H. triangularus* (described above), and the base is defined by the FO of *F. reinholdii* in Sample 383-U1541B-14H-5, 50 cm (127.51 m CSF-A), near the bottom of the recovered sequence. Given the longstanding uncertainty in the community (e.g., Frenguelli, 1949; Schrader, 1973; Suto and Uramoto, 2015) regarding the species concepts differentiating *F. reinholdii* from the related taxon *F. fossilis*, the LO of which is in Sample 383-U1541B-15H-1, 50 cm (131.10 m CSF-A), we note that the placement of this zone boundary is tentative and will likely be updated through postcruise refinement. The final zone, the *A. ingens* var. *ovalis* Partial Range Zone, sits below the *F. reinholdii* Zone. The top of the zone is defined by the FO of *F. reinholdii* (described above), and the base, marked by the FO of *A. ingens* var. *ovalis*, probably lies below the lowermost sample recovered from Hole U1541B. Although diatom abundance decreases as calcareous nannofossils become dominant toward the bottom of the hole, the lowermost sample recovered from Hole U1541B contains trace occurrences of *A. ingens* var. A. sensu Harwood and Maruyama, which we infer to be conspecific with *A. ingens* var. *ovalis* sensu Gersonde (see **Pliocene diatom zones**).

Table T5. Distribution chart of radiolarians, Hole U1541B. **Download table in CSV format.**

Radiolarians

Core catcher samples from Hole U1541B were analyzed for the occurrence of radiolarians (383-U1541B-1H-CC through 15H-CC [7.00–138.04 m CSF-A]). Radiolarians are abundant and generally well preserved in Site U1541 sediments (Figure **F18**; Table **T5**) except for Samples 1H-CC (7.00–7.06 m CSF-A) and 8H-CC (72.09–72.15 m CSF-A), which contain few radiolarians, and Sample 15H-CC (137.98–138.04 m CSF-A), in which radiolarians are absent. Recognized radiolarian biostratigraphic events are shown alongside diatoms, calcareous nannofossils, and planktonic foraminifers in Table **T3**.

Sample 383-U1541B-1H-CC (7.00–7.06 m CSF-A) is correlative to the Omega Zone based on the radiolarian assemblage and the absence of *Stylatractus universus*. The boundary between the Omega Zone and the underlying Psi Zone was identified by the presence of *S. universus* (0.43 Ma) in Sample 2H-CC (15.59–15.65 m CSF-A). The last appearance of *Pterocanium charybdeum trilobum* (0.86 Ma) is in Sample 3H-CC (24.83–24.89 m CSF-A). The good preservation and frequent occurrence of *P. charybdeum trilobum* in Sample 3H-CC defined its placement at the top of the Chi Zone (24.83–24.89 m CSF-A). The LAD of *Antarctissa cylindrica* (0.64 Ma), which falls in the Psi Zone, was also identified in Sample 3H-CC.

The following interval, down to 45.20 m CSF-A (Sample 383-U1541B-5H-CC), was assigned to the upper Chi Zone by the presence of *Cycladophora pliocenica*. In this sample, *Helotholus vema* is diagnostic of the Upsilon Zone. The common occurrence with *Triceraspyris antarctica* and absence of *Eucyrtidium calvertense* implies a Pleistocene age in the Chi Zone and reworking of *H. vema*. The lower Chi Zone and the top of the Phi Zone occur in Sample 6H-CC (53.90–53.96 m CSF-A), where *Triceraspyris antarctica* and *E. calvertense* were recognized. The Upsilon Zone, whose top is defined by the LAD of *H. vema* (2.40 Ma), was encountered in Hole U1541B in Sample 7H-CC (61.64–61.70 m CSF-A). The LO of *Desmospyris spongiosa* and occurrence of *Cycladophora davisiana* in Sample 7H-CC place this sample in the upper Upsilon Zone. The middle/upper boundary of the Upsilon Zone is defined by the first appearance datum (FAD) of *C. davisiana* in Sample 8H-CC (72.09–

Table T6. Distribution chart of silicoflagellates, Hole U1541B. **Download table in CSV format.**

72.15 m CSF-A). The lower/middle part of the Upsilon Zone occurs from this sample through Sample 9H-CC (82.98–83.04 m CSF-A), where the LO of *Prunopyle titan* was recognized. The LO of *Lampromitra coronata*, which falls in the lower Upsilon Subzone, occurs in Sample 10H-CC.

The top of the Tau Zone was placed in Sample 383-U1541B-10H-CC (91.41–91.47 m CSF-A) by the first appearance of *H. vema*. The FAD of *H. vema* was challenging to assign at Site U1541 because of its co-occurrence with *Helotholus haysi*, a species very similar to *H. vema*, and a drop in abundance below 82.98 m CSF-A. For this report, the FO of *H. vema* was defined as the first appearance of specimens with six regularly radial beams. The LCO of *Lychnocanium grande* was recognized in Sample 11H-CC (102.03–102.09 m CSF-A). Above this sample, only single specimens of *L. grande* were observed, and the FO was noted well above the LCO. At Site U1541, the LCO of *L. grande* (5 Ma) is consistent with the diatom biostratigraphy, which suggests an age of 5–5.3 Ma.

The *Amphymenium challengerae* Zone was assigned in Sample 383-U1541B-12H-CC (111.54–111.60 m CSF-A) by the presence of *A. challengerae*, which has a short range from 6.22 to 6.84 Ma. This species was not found below this interval; therefore, this sample represents the total range of *A. challengerae* at Site U1541 and the base of the *A. challengerae* Zone. The deepest sample from Hole U1541B (15H-CC; 129.85–129.91 m CSF-A) is older than 7.84 Ma based on the absence of *Acrosphaera labrata* (FAD at 7.84 Ma), which is in good agreement with the diatom age estimate (younger than 7.9 Ma) for the same sample.

Silicoflagellates

Silicoflagellates were analyzed from 1 mudline, 15 core catcher, and 13 split-core samples from Hole U1541B. Silicoflagellates are rare to barren throughout the core except for four samples in which they are common to abundant (Table **T6**; Figure **F18**). The silicoflagellate assemblage at Site U1541 consists of nine species: *Dictyocha stapedia, Dictyocha aculeata, Dictyocha perlaevis, Dictyocha brevispina, Dictyocha concavata, Stephanocha speculum, Stephanocha boliviensis, Octactis* sp., and *Bachmannocena diodon* (Figure **F20**). *D. stapedia* and *D. aculeata* are the dominant species in the mudline sample but are otherwise sporadic. *S. speculum* is present in all samples and has a large morphological variability, including specimens with long and short corner spines, specimens with variable apical ring features (*S. speculum* var. *monospicata*, *S. speculum* var. *bispicata*, *S. speculum* var. *coronata*, and *S. speculum* var. *pseudofibula*), specimens with different numbers of basal ring sides (*S. speculum* var. *pentagona* and *S. speculum* var. *octonaria*), and a large (≥30 µm) variety similar to the *S. speculum* Group B described by Tsutsui et al. (2009) from water samples. A peculiar assemblage dominated by the pentagonal variety of *S. speculum* showing coronatid ornamentation occurs in Sample 383-U1541B-9H-CC (82.98–83.04 m CSF-A). *Octactis* sp. is present in Samples 4H-CC through 6H-CC (35.67–53.96 m CSF-A).

The *D. speculum* A Zone, developed for the Southern Ocean (Ciesielski 1975) and spanning the middle–late Pleistocene, was recognized from the top of the core through Sample 383-U1541B-9H-CC (82.98–83.04 m CSF-A). The presence of *S. boliviensis* in Sample 10H-CC (91.41–91.47 m CSF-A) indicates the top of the *S. boliviensis* Zone, and the common abundance of *B. diodon* from Sample 13H-CC (120.55–120.61 m CSF-A) downhole indicates the *B. diodon* Zone, which spans the late Miocene. However, the *Dictyocha aspera* var. *pygmea* and *Dictyocha pseudofibula* Zones in between the two zones mentioned above were not recognized. This was possibly due to the rare occurrences of silicoflagellates, although one single specimen of *D. pseudofibula* was recovered in Sample 13H-5, 50 cm (118.09 m CSF-A).

Calcareous nannofossils

Calcareous nannofossil biostratigraphy is based on the analysis of 47 samples: 1 mudline, 15 core catcher, and 20 split-core samples from Hole U1541B and 11 split-core samples from Hole U1541C (23.7–47.65 m CSF-A). In general, nannofossils are present throughout the sequence with variable abundance (Table **T7**; Figures **F18**, **F19**); they are common to dominant in most of the studied samples and have minimum abundances of few to rare only in Samples 383-U1541B-1H-3, 93 cm (3.92 m CSF-A), and 11H-CC (102.03–102.09 m CSF-A). Although the preservation of calcareous nannofossils varies, it is moderate to good in the majority of the samples.

The nannofossil assemblage at Site U1541 consists of 31 groups/taxa, including *Emiliania huxleyi, Gephyrocapsa margerelii/muellerae, Gephyrocapsa caribbeanica, Gephyrocapsa oceanica, Gephyrocapsa* spp. (small <4 µm, medium, and large >5.5 µm), *Gephyrocapsa omega, Pseudoemiliania lacunosa, Reticulofenestra* (<3, 3–5, 5–7, and >7 µm), *Reticulofenestra asanoi, R. pseudoumbilicus, Reticulofenestra perplexa, Dictyoccocites* spp., *C. pelagicus, Calcidiscus leptoporus, Calcidiscus macintyrei, Helicosphaera carteri, Helicosphaera sellii, Pontosphaera multipora, Rhabdosphaera clavigera, Syracosphaera* spp. (including *Syracosphaera pulchra*), *Scyphosphaera* spp., *Discoaster* spp., *Discoaster variabilis*, *Amaurolithus primus*, and *Amaurolithus delicatus*. Reworked specimens including *Dictyoccocites* spp. and *Reticulofenestra* spp. were found throughout the cores (Table **T7**; Figure **F21**).

In total, 12 biostratigraphic events were observed at Site U1541. Nannofossil Zones CN15/NN21 through CN11a/NN13 were recognized (Figure **F16**) based on the following events:

- The FO of *E. huxleyi* (Sample 383-U1541B-1H-4, 53 cm; 5.01–5.06 m CSF-A);
- The LO of *P. lacunosa* (Sample 2H-3, 114 cm; 10.50 m CSF-A);
- The LO of *G. omega* (Sample 2H-5, 100 cm; 13.23 m CSF-A);
- The LO of *R. asanoi* (Sample 3H-6, 80 cm [23.79 m CSF-A]; refined in Sample 383-U1541C-4H-4, 20 cm [27.82 m CSF-A]);
- The first common occurrence (FCO) of *R. asanoi* (Sample 383-U1541B-3H-CC [24.83–24.89 m CSF-A]; refined in Sample 383-U1541C-4H-6, 40 cm [31.02 m CSF-A]);
- The LO of *Gephyrocapsa* spp. (>5.5 µm) large (Sample 383-U1541B-4H-CC [35.67–35.73 m CSF-A]; refined in Sample 383-U1541C-5H-2, 57 cm [34.67 m CSF-A])
- The FO of *Gephyrocapsa* spp. (>5.5 µm) large (Sample 383-U1541B-5H-2, 60 cm [37.70 m CSF-A]; refined in Sample 383-U1541C-5H-4, 35 cm [37.45 m CSF-A]);
- The FO of *Gephyrocapsa* spp. (4–5.5 µm) medium (Sample 383-U1541B-5H-5, 66 cm [42.27 m CSF-A]; refined in Sample 383-U1541C-6H-2, 125 cm [44.86 m CSF-A]);
- The LO of *R. pseudoumbilicus* (Sample 383-U1541B-10H-2, 90 cm; 85.50 m CSF-A); and
- The LO of *A. primus* (Sample 383-U1541B-10H-CC cm; 91.41–91.47 m CSF-A).

Figure F20. Silicoflagellates, Hole U1541B. Focus on basal ring (upper images) and apical structure (lower images). Light microscope. 1. *Dictyocha stapedia*. 2. *Dictyocha aculeata*. 3. *Stephanocha speculum* var. *speculum*. 4. *S. speculum*, large form with indented basal ring sides. 5. *S. speculum* var. *pentagona* with apical ring spines. 6. *S. speculum* var. *septenaria*, large form. 7. *S. speculum* var. *pseudofibula*. 8. *Octactis* sp. 9. *Stephanocha boliviensis* with apical ring spines. 10. *S. boliviensis*. 11. *Dictyocha concavata*. 12. *Dictyocha brevispina*. 13. *Dictyocha perlaevis*. 14. *Bachmannocena diodon* var. *nodosa*. 15. *D. perlaevis*, asperoid form.

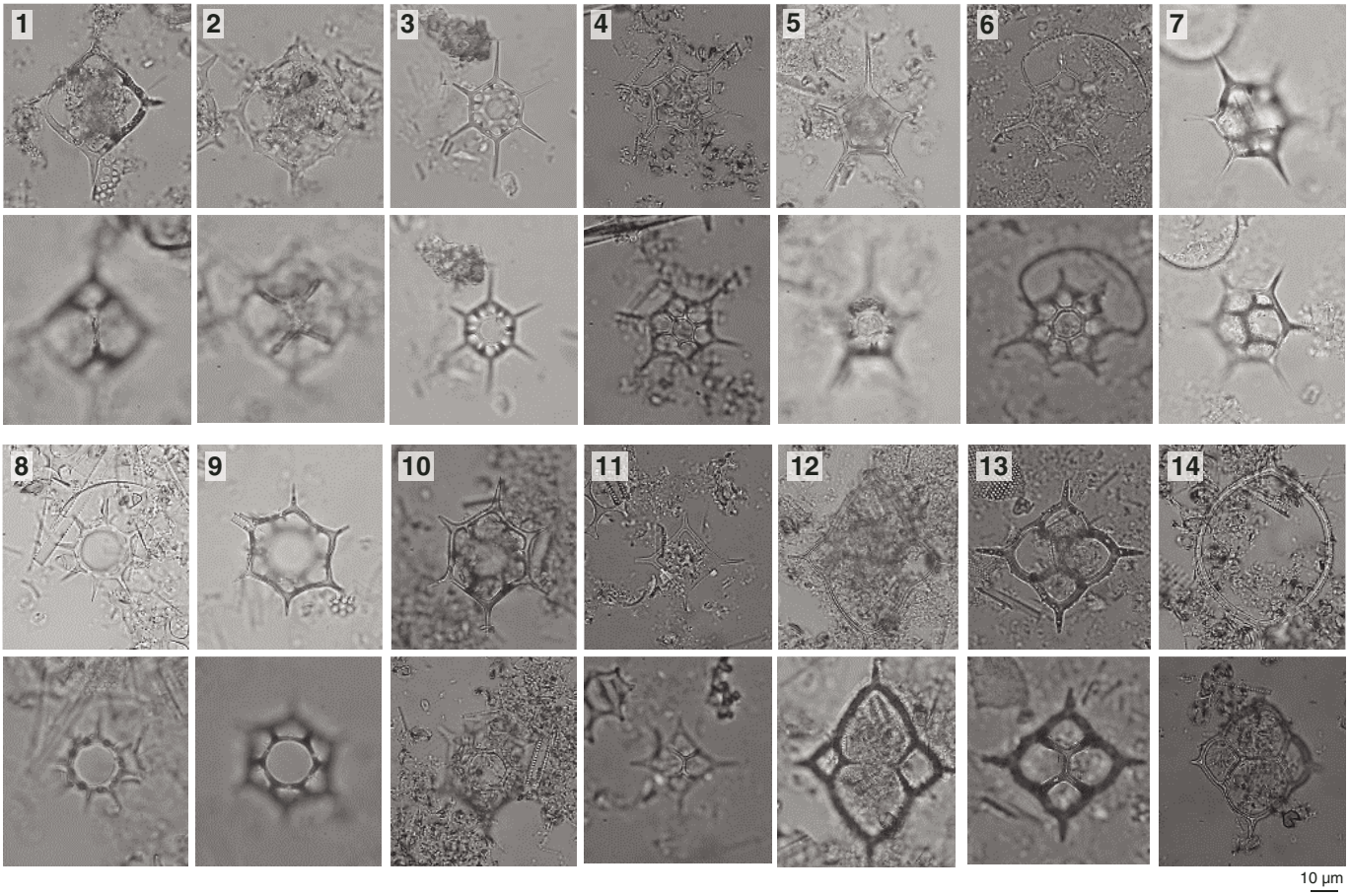

Table T7. Distribution chart of calcareous nannofossils, Holes U1541B and U1541C. **Download table in CSV format.**

The presence of *H. sellii* in Sample 383-U1541B-5H-CC (45.14–45.20 m CSF-A) is not considered a true LO because this species rarely occurs in the core; *Helicosphaera* is usually rare throughout the core, possibly due to ecological forcing. The LO of *C. macintyrei* (Sample 383-U1541B-5H-CC [45.14–45.20 m CSF-A]; refined in Sample 383-U1541C-6H-3, 69 cm [45.81 m CSF-A]) occurs below the FO of *Gephyrocapsa* spp. (4–5.5 µm) medium in Holes U1541B and U1541C, although its LO is slightly younger, which is also possibly due to ecological forcing.

No calcareous nannofossil markers were found deeper than Sample U1541B-10H-CC. Several specimens of *Discoaster* were occasionally observed between Samples 10H-3, 80 cm (86.90 m CSF-A), and 15H-CC (137.98–138.04 m CSF-A), but they could not be identified at the species level due to their poor preservation and therefore did not provide any additional age constraint. We noted large changes in the size of *Reticulofenestra* coccoliths, from <3 to >10 µm, especially in the cores below Sample 5H-CC (45.14–45.2 m CSF-A) (Figure **F22**).

Foraminifers

Planktonic foraminifers

Core catcher samples from all 14 cores from Hole U1541B and 1 working-half sample from Hole U1541C were analyzed for planktonic foraminifers (Table **T8**). Planktonic foraminifers are abundant throughout Hole U1541B and make up >50% of the coarse fraction residue in most samples (Figure **F18**). Abundance is lower (5%–25%) only in Samples 383-U1541B-11H-CC and 13H-CC. Preservation is generally moderate to good in Hole U1541B but poor in Sample 11H-CC. Many encrusted forms of *Neogloboquadrina pachyderma, Globoconella inflata, Globoconella puncticulata puncticuloides*, and *Truncorotalia crassaformis* were found, which may influence stable isotope or trace element analyses (Jonkers et al., 2012; Steinhardt et al., 2015).

Assemblages are characterized by mainly high-latitude and some temperate species. *N. pachyderma* (sinistral) dominates the assemblage in Samples 383-U1541B-1H-CC through 7H-CC (7.00–61.70 m CSF-A), and *Globigerina bulloides* is present throughout the sequence. *T. crassaformis, Truncorotalia crassaformis hessi, Truncorotalia crassaformis ronda, Truncorotalia crassaformis imbricata, Globoconella conomiozea, Globoconella pliozea, G. puncticulata, G. puncticulata puncticuloides, G. inflata*, and *Hirsutella juanai* occur regularly in their respective age ranges. Rarer species include *Turborotalita quinqueloba, Globigerinita glutinata, Globigerina woodi, Orbulina universa, Neogloboquadrina incompta, Neogloboquadrina dutertrei, Truncorotalia truncatulinoides, Truncorotalia crassula, Globorotalia miotumida, Hirsutella hirsuta, Hirsutella margaritae*, and *Hirsutella scitula*. Examples of major foraminiferal taxa found at Site U1541 are shown in Figures **F23** and **F24**.

Figure F21. Calcareous nannofossils, Hole U1541B. Light microscope. 1. *Emiliania huxleyi* (mudline). 2. *Pseudoemiliania lacunosa* (3H-CC). 3. *Gephyrocapsa omega* (2H-CC). 4. *Reticulofenestra asanoi* (3H-CC). 5. *Gephyrocapsa* large (>5.5 µm) (4H-CC). 6. *Helicosphaera sellii* (5H-CC). 7. *Calcidiscus macintyrei* (5H-CC). 8, 9. *Reticulofenestra pseudoumbilica*; (8) 10H-CC, (9) 11H-3, 71 cm. 10. *Amaurolithus primus/delicatus* (10H-CC). 11. *Scyphosphaera* spp. (10H-1, 70 cm). 12. *Discoaster variabilis* (13H-1, 50 cm).

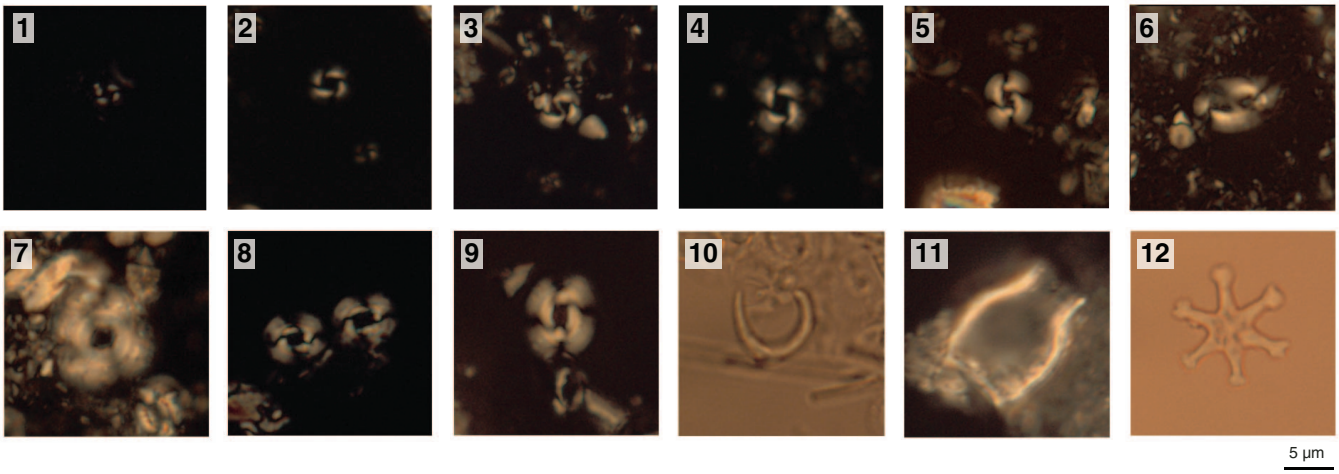

Eleven biomarkers species are present in Site U1541 planktonic foraminifer assemblages: *G. inflata, T. crassaformis hessi, T. truncatulinoides, G. conomiozea, G. miotumida, Globoconella sphericomiozea, H. hirsuta, H. juanai, G. woodi, G. puncticulata*, and *H. margaritae*. The uppermost part of Hole U1541B is late Pleistocene in age based on the presence of *T. crassaformis imbricata* (0.6 Ma; Bylinskaya, 2004) in Samples 383-U1541B-1H-CC and 2H-CC (7.00–15.65 m CSF-A) and *T. hessi* (~0.75 Ma; Gradstein et al., 2012) in Samples 1H-CC through 4H-CC (7.00–35.73 m CSF-A). *G. inflata* was observed between Samples 1H-CC and 7H-CC (7.00–61.70 m CSF-A), and *G. puncticulata puncticuloides* is abundant in Samples 3H-CC through 10H-CC (22.84–91.47 m CSF-A), which dates this interval to between 0.7 and 2.39–3.13 Ma (Hornibrook, 1981; Hornibrook and Jenkins, 1994; Wei, 1994; Scott et al., 2007). *T. truncatulinoides* was found only in Sample 1H-CC (7.00–7.06 m CSF-A), indicating Zone SN14 of Jenkins (1993). *T. crassaformis ronda*, another subspecies of *T. crassaformis*, was found sporadically in Samples 5H-CC through 10H-CC (45.14–91.47 m CSF-A), indicating that this interval comprises the upper Quaternary (~0.6 Ma) to mid-lower Pliocene (Bylinskaya, 2004). *G. woodi* was present at low abundance in most samples between Samples 8H-CC and 14H-CC (72.09–129.91 m CSF-A), indicating an age older than 2.3 Ma, but it was absent in Samples 10H-CC and 12H-CC, which suggests that it occurs only sporadically in the higher latitudes and its first occurrence at Site U1541 might not match the global LAD. *G. puncticulata* is present in Samples 7H-CC through 10H-CC (61.64–91.47 m CSF-A), indicating ages older than 1.88–2.39 Ma for this interval (Wei, 1994). Sporadic specimens of *H. margaritae* in Samples 14H-CC and 383-U1541C-11H-6 indicate that these samples are older than 3.85 Ma. *G. conomiozea* was observed only in Sample 383-U1541B-12H-CC (111.54–111.60 m CSF-A), indicating an age between 5.72–6.14 and 6.14–8.58 Ma (Wei, 1994). *H. juanai* occurs in Samples 11H-CC through 14H-CC (102.03–129.91 m CSF-A); thus, this interval can be associated with ages between 5.20–5.72 and 9.7 Ma (Chaisson and Pearson, 1997; Wade et al., 2011). *G. miotumida* occurs only in the bottommost samples from Hole U1541B (13H-CC and 14H-CC), indicating that the base of the recovered sequence is older than 6.14–8.58 Ma (Wei, 1994; Kennett and Srinivasan, 1983). Planktonic foraminiferal age estimates are consistent with radiolarian, diatom, and nannofossil ages.

Benthic foraminifers

Benthic foraminifers were examined in core catcher samples from Hole U1541B (15 samples). Samples with an average volume of ~20 cm^3 were processed from all core catchers to obtain quantitative estimates of benthic foraminiferal distribution patterns downhole. The mudline samples recovered from Holes U1541B and U1541C were also examined, although mudline assemblage data were not systematically collected. To assess assemblage composition and variability, ~100 specimens from the >125 µm fraction were picked and transferred to slides for identification and counting. The presence and distribution of benthic foraminifers was additionally checked in the 125–63 µm fraction to ensure that assemblages in the >125 µm fraction were representative and that small species such as phytodetritus feeders or small infaunal taxa were not overlooked.

Benthic foraminifers are more abundant at Site U1541 than at Sites U1539 and U1540, and their abundance is few or greater in all but five samples examined (Figure **F18**). They are well preserved in the upper part of the sequence and moderately to poorly preserved in the lower part (Figures **F18**, **F19**; Table **T9**).

In total, 79 benthic foraminifer taxa were identified at this site. Table **T9** and Figure **F25** summarize the downcore distribution of benthic foraminifers in core catcher samples from Hole U1541B. Figure **F26** illustrates characteristic taxa found at this site in addition to taxa from Sites U1539 and U1540.

The overall assemblage composition indicates lower bathyal to abyssal paleodepth throughout the late Miocene to Holocene, and the site has remained above the carbonate compensation depth. Species commonly recorded throughout the sequence include the calcareous species *Globocassidulina subglobosa, Melonis barleeanum, Nuttallides umbonifera, Oridorsalis umbonatus*, and *Pullenia bulloides*. The *Uvigerina* species is dominant in Samples 383-U1541B-1H-CC, 5H-CC, and 8H-CC and present in small amounts in a few more samples. *Cibicides*/*Cibicidoides* species mainly comprising *Cibicidoides mundulus, Cibicidoides lobatulus*, and *Cibi-*

Figure F22. SEM images of calcareous nannofossils, Hole U1541B. Scale bar = 5 µm. 1. *Pseudoemiliania lacunosa*. 2. *Reticulofenestra asanoi*. 3. Transitional form between *Reticulofenestra minutula* and *P. lacunosa*. 4, 5. *R. minutula*. 6. Transitional form between *R. minutula* and *R. asanoi*. 7–17. *R. minutula* showing different degrees of calcification of the central area; (10, 12, 15) closed central area/*Dictyococcites* spp.). 18. R. *minutula* with slits. 19–21. *Reticulofenestra haquii*/*Reticulofenestra* 3–5 µm. 22–26. *Reticulofenestra pseudoumbilicus* showing different sizes (8–12 µm) and different degrees of calcification of the central area; (22, 23, 25, 26) open central area, (24) closed. 27. Coccosphere of *R. pseudoumbilicus*.

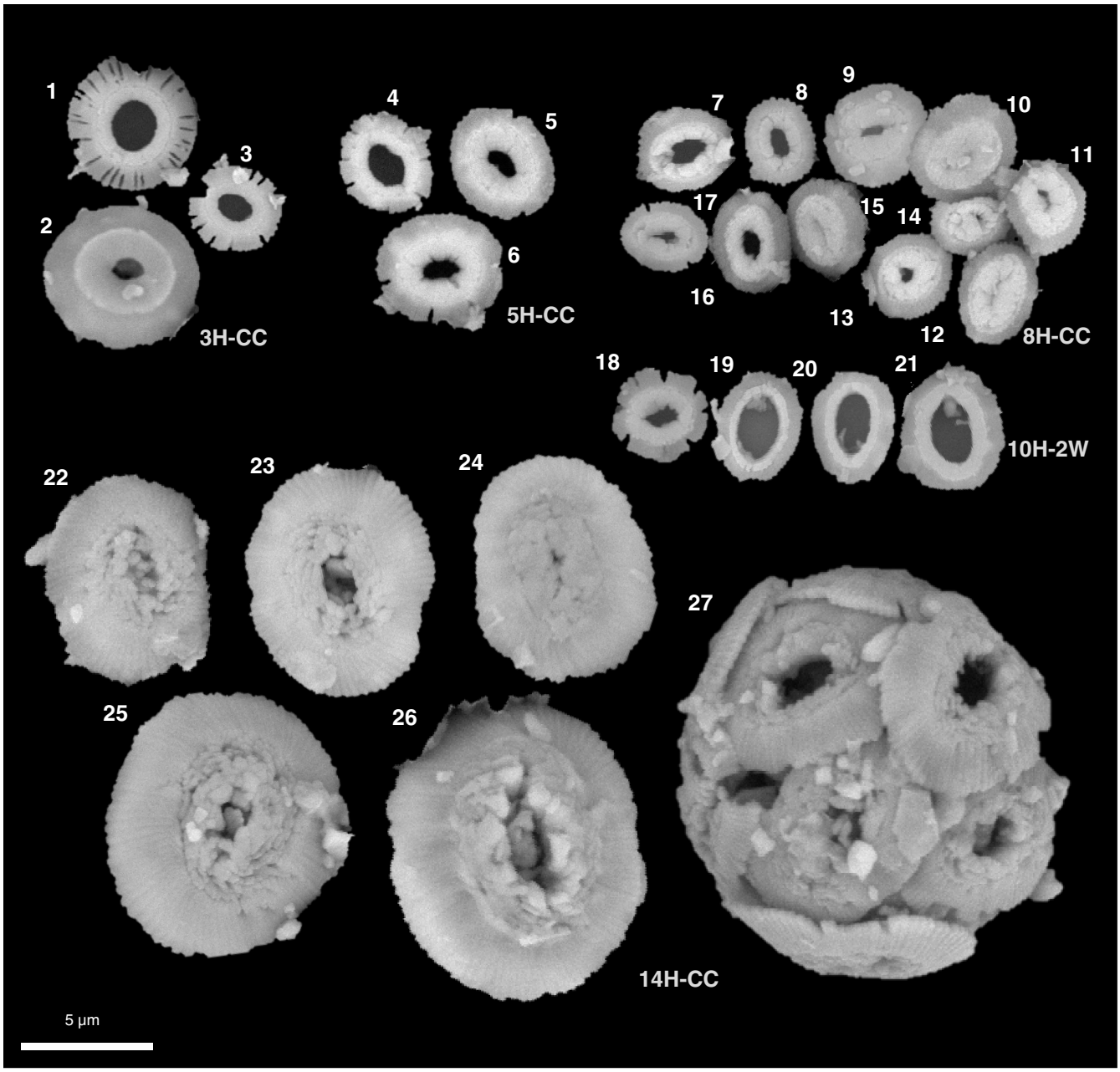

Table T8. Distribution chart of planktonic foraminifers, Holes U1541B and U1541C. **Download table in CSV format.**

cides wuellerstorfi are present in lesser amounts and show a decreasing trend between Samples 2H-CC and 11H-CC. The abundance of this species, mainly *C. wuellerstorfi*, increases in Sample 12H-CC, and this species remains abundant thereafter along with *N. umbonifera*, suggesting well-oxygenated deep water with strong currents and high seasonality (Singh and Gupta, 2004). Below ~90 m CSF-A, the diversity of benthic foraminifers reaches a maximum and remains high downcore. None of the species mentioned above are abundant, and *N. umbonifera*, a species indicative of corrosive bottom water (Singh and Gupta, 2010; Bremer and Lohmann, 1982), increases. These conditions suggest the presence of warm corrosive bottom water at Site U1541 below ~90 m CSF-A. Above this depth, the abundance of *Uvigerina* suggests higher surface productivity (Das et al., 2018; Schönfeld, 2006; Singh and Gupta, 2004) and abundances of *O. umbonatus, Melonis* spp., and *Pullenia* spp. suggest intermediate to high flux of organic matter and low-oxygen conditions (Corliss, 1985; Singh and Gupta, 2004; Fontanier et al.,

Figure F23. Common planktonic foraminifers, Site U1541. Scale bars = 100 µm. A. *Orbulina universa*. B. *Orbulina suturalis*. C. *Globigerina bulloides*. D. *Globigerina umbilicata*. E. *Globigerinita glutinata*. F. *Neogloboquadrina pachyderma*. G. *Neogloboquadrina incompta*. H–J. *Hirsutella juanai* in (H) spiral, (I) side, and (J) umbilical view. K. *Hirsutella scitula*. L, M. *Hirsutella hirsuta* in (L) umbilical and (M) spiral view. N, O. *Truncorotalia crassaformis* in (N) umbilical and (O) side view. P, Q. *T. crassaformis hessi* in (P) umbilical and (Q) spiral view. R. *T. crassaformis imbricata*. S. *Truncorotalia crassula*. T. *T. crassaformis ronda*.

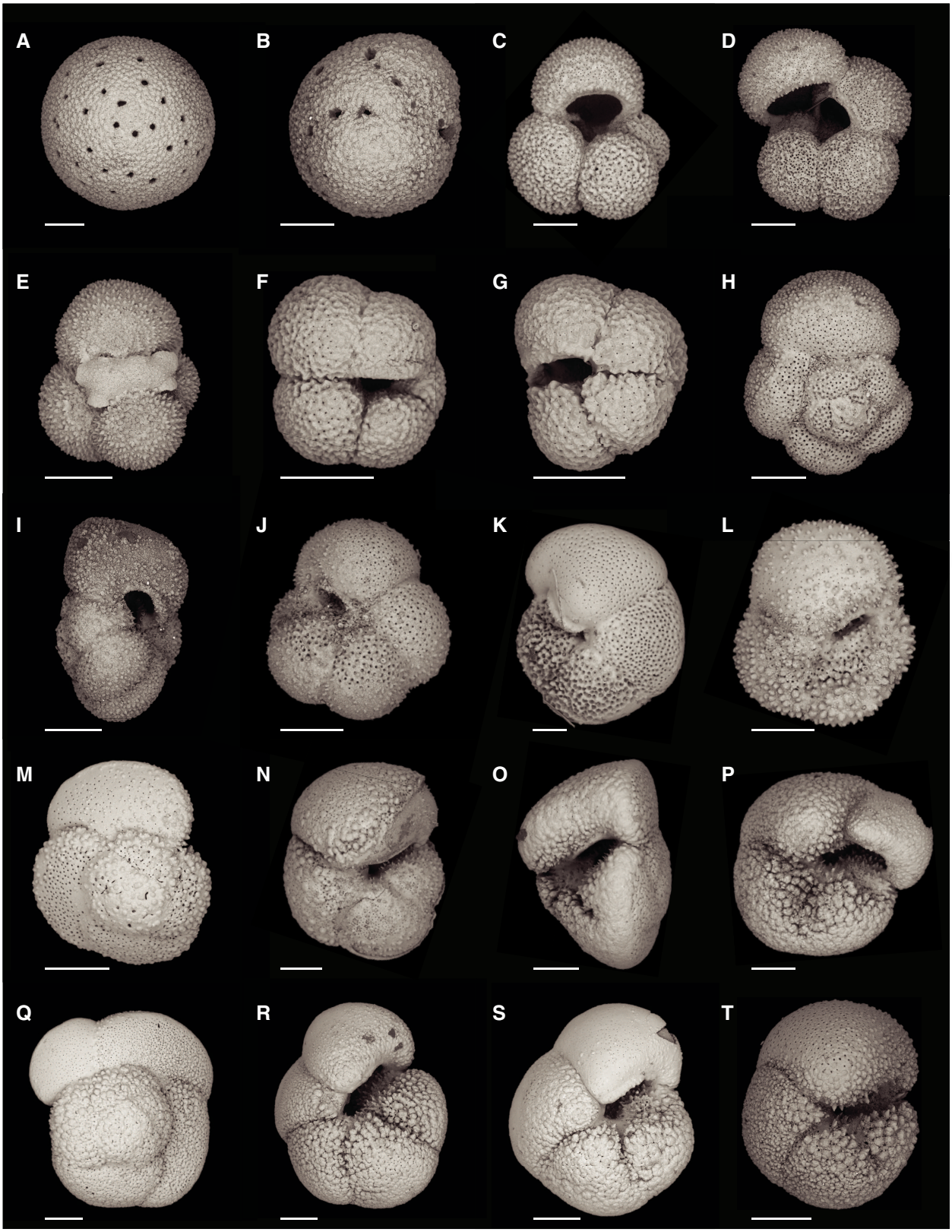

Figure F24. Common planktonic foraminifers, Site U1541. Scale bars = 100 µm. A–C. *Globorotalia miotumida* in (A) umbilical, (B) side, and (C) spiral view. D–F. *Globoconella pliozea* in (D) umbilical, (E) side, and (F) spiral view. G–I. *Globoconella conomiozea* in (G) umbilical, (H) side, and (I) spiral view. J, K. *Globoconella puncticulata* in (J) umbilical and (K) side view. L, M. *Globoconella puncticulata puncticuloides* in (L) umbilical and (M) side view. N, O. *Globoconella inflata* in (N) umbilical and (O) side view.

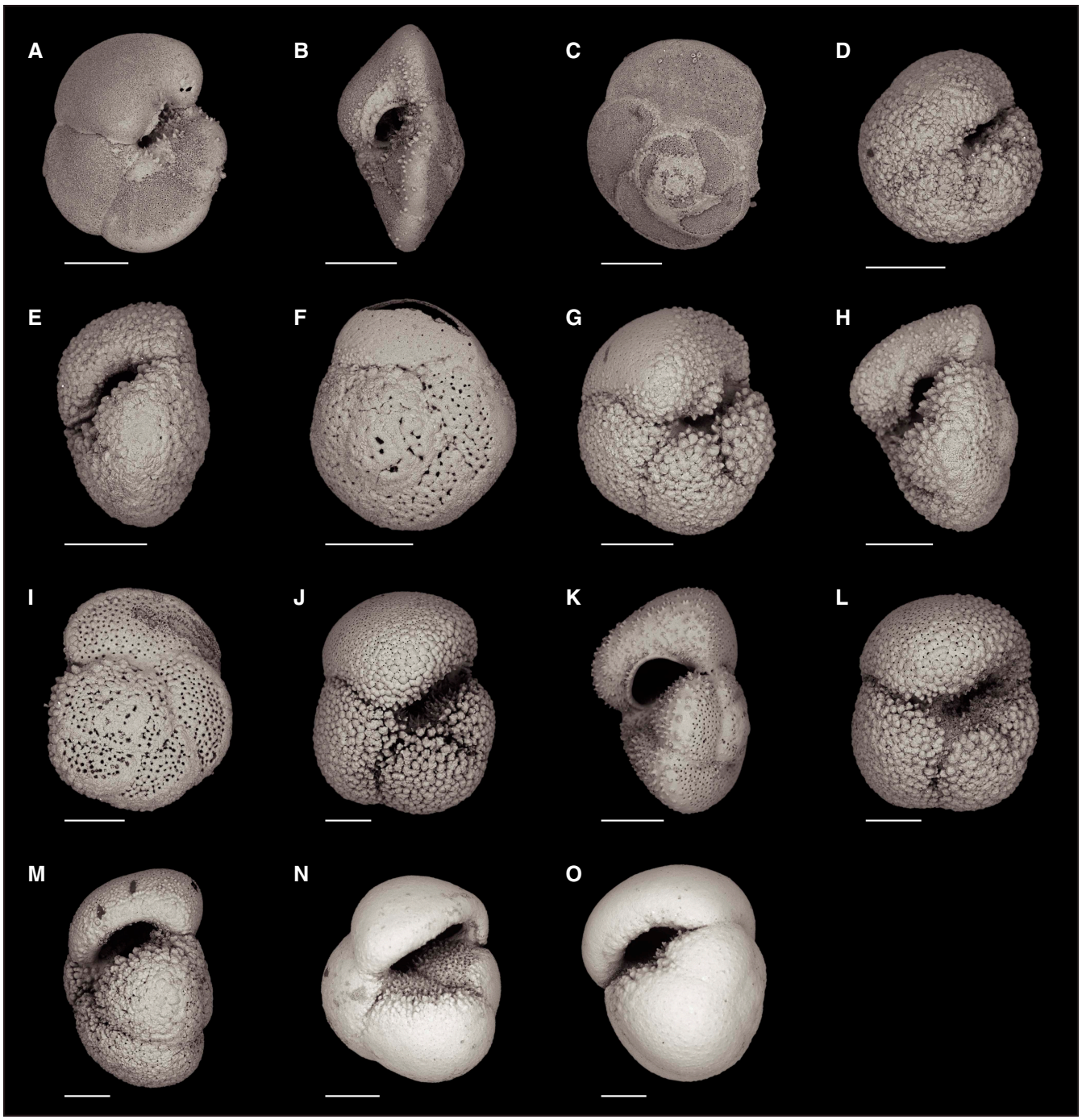

Table T9. Distribution chart of benthic foraminifers, Hole U1541B. **Download table in CSV format.**

2005; Verma et al., 2013). The abundance of *G. subglobosa* is associated with enhanced flow of AABW (Corliss, 1979; Singh and Gupta, 2004, 2010; Singh et al., 2012).

Downcore changes in assemblage composition at Site U1541 suggest changes in paleoenvironmental conditions that may be linked to distinct phases of glacial–interglacial and major global paleoclimatic changes. However, the analyzed sample resolution is not sufficiently high to capture glacial–interglacial cyclicity or definitively identify climate events. Postcruise work will explore these intervals of change, including species diversity minima at ~36 and ~70 m CSF-A (Figure **F25**), which may represent cool intervals, and the high species diversity peak at ~91 m CSF, which may be associated with global warmth (Singh and Gupta, 2005; Singh et al., 2012; Gupta et al., 2013).

Figure F25. Species diversity index (H) and abundance of dominant genus/species Uvigerinids, *Oridorsalis umbonatus, Pullenia* spp., Milliolids, *Melonis* spp., *Globocassidulina subglobosa*, and *Cibicides/Cibicidoides* spp., Site U1541. Gray field = interval potentially influenced by warm bottom water.

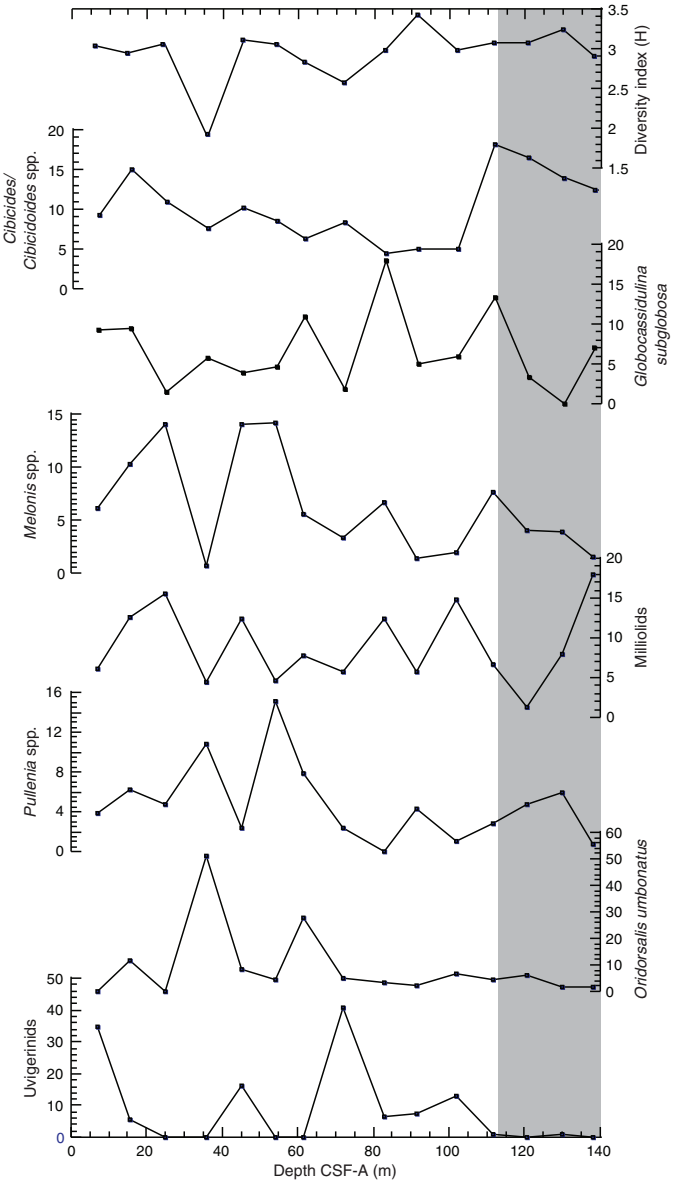

The mudline samples from Holes U1541B and U1541C were soaked in rose bengal and ethanol solution and gently washed to preserve fragile, agglutinated foraminifer specimens with extremely low fossilization potential. The mudline samples from Holes U1541B and U1541C have stained agglutinated and calcareous benthic foraminifers, suggesting that both mudlines collected modern sediment–water interfaces. Although relative species abundance was not tabulated, the mudline samples from this site have diverse assemblages and contain stained specimens of the common and rare agglutinated species such as *Cribostromoides subglobosus, Paratrochammina challengeri, Rhabdammina* spp., *Reophax* sp., *Rhizammina* sp., *Siphotextularia* sp., and *Ammobaculites* sp. Calcareous taxa are also very diverse and include *Astrononion stelligerum*, *C. mundulus*, *Dentalina* spp., *Eggerella bradyi, Epistominella exigua, Fursenkoina complanata, Fursenkoina bradyi, Fissurina* spp., *G. subglobosa, Lenticulina convergens, M. barleeanum, Nonion* sp., *Pullenia quinqueloba, O. umbonatus, Quinqueloculina venusta, Quinqueloculina oblonga*, and *Triloculina tricarinata*. A few additional species were found unstained. One intact stained bilvalve was also found in the mudline sample from Hole U1541C. The mudline samples from both holes are dominated by unstained planktonic foraminifers and radiolarians. Photomicrographs of mudline benthic foraminifer and bivalve specimens are presented in Figure **F27**.

Ostracods

Core catcher samples from Holes U1541A (1H-CC) and U1541B (1H-CC through 15H-CC) were also examined for the presence of ostracods. All ostracods present in the >125 mm sand fraction were picked, counted, and identified to the genus level. Their abundance ranges between rare (1 valve) and abundant (>50 valves), although two samples (383-U1541B-6H-CC and 13H-CC) were barren (Figure **F18**). Valves and carapaces are moderately to well preserved. The highest ostracod abundance was observed in Samples 383-U1541A-1H-CC and 383-U1541B-9H-CC. The assemblage is dominated by *Krithe* and *Henryhowella* and includes *Poseidonamicus, Pelecocythere, Legitimocythere, Pennyella, Bradleya*, and *Ambocythere* in lower concentrations. The taxa indicate lower bathyal to abyssal depths and varying bottom water ventilation (Alvarez Zarikian et al., 2009, Alvarez Zarikian, 2015; Stepanova and Lyle, 2014; Whatley et al., 1986; Yasuhara et al., 2013). Table **T10** summarizes the downcore distribution of ostracods present in core catcher samples from Site U1541.

Figure F26. Benthic foraminifers, Hole U1541B. Scale bars = 100 µm. 1. *Spiroplectella* sp. (11H-CC). 2. *Stilostomella lepidula*. (14H-CC). 3. *Pleurostomella incrasata* (9H-CC). 4. *Procerolagena clavata* (13H-CC). 5. *Uvigerina* sp. (9H-CC) 6. *Uvigerina peregrina* (10H-CC). 7. *Uvigerina hispida* (13H-CC). 8. *Siphotextularia* sp. (13H-CC). 9. *Lagena plumigera* (10H-CC). 10, 11. *Spiroloculina* sp. (14H-CC). 12. *Bolivina decussata* (10H-CC). 13. *Ehrenbergina* sp. (11H-CC). 14. *Pleurostomella* sp. (14H-CC) 15. *Pseudonodosaria* sp. (9H-CC). 16. *Evolvocassidulina* sp. (6H-CC). 17–19. *Globobulimina* sp. (17, 18) 13H-CC. (19) 15H-CC. 20. *Laticarina pauperata* (14H-CC). 21. *Cibicides wuellerstorfi* (15H-CC). 22. *Pseudoglandulina* sp. (13H-CC). 23. *Lagena quadralata* (14H-CC). 24. *Fissurina* sp. (covered with nannofossils) (15H-CC).

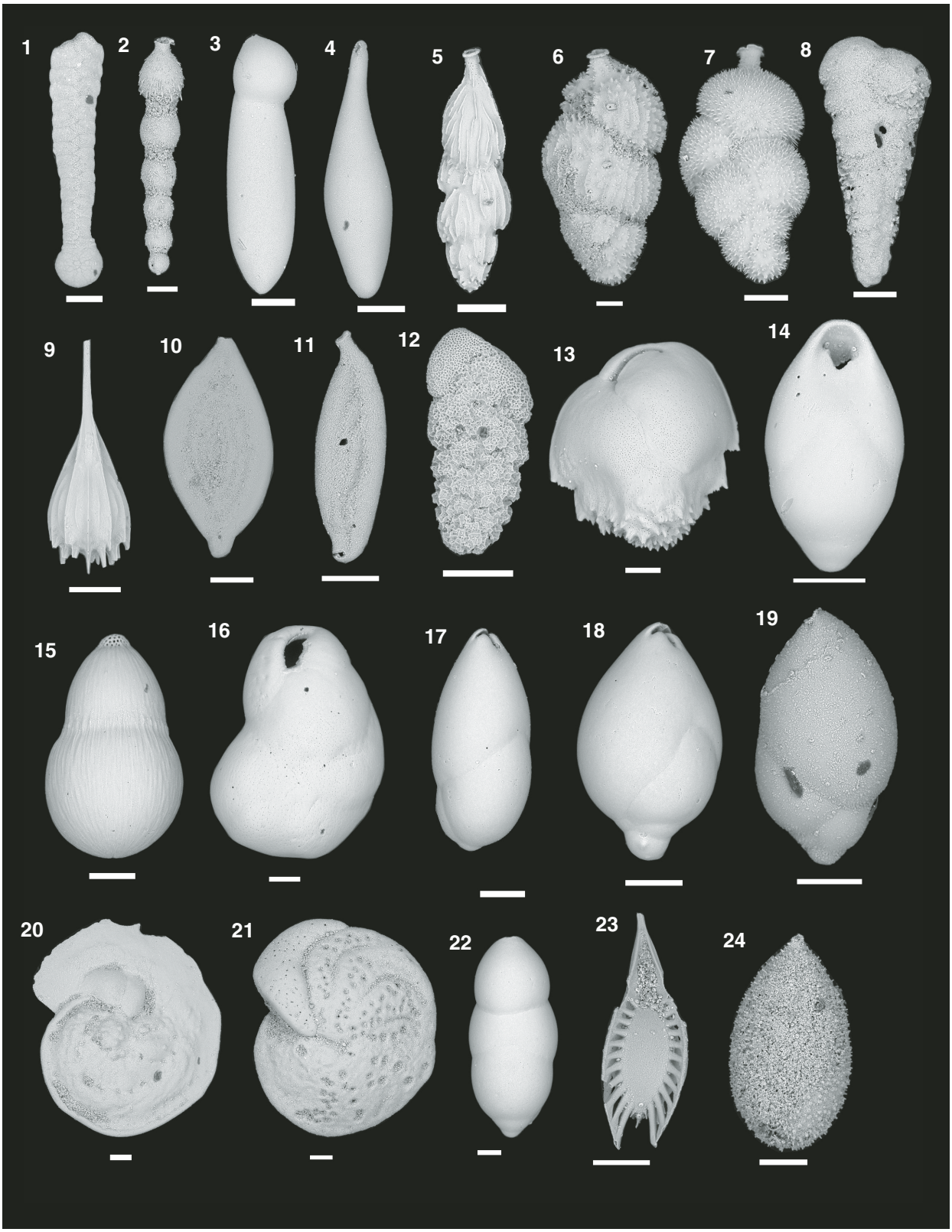

Figure F27. Agglutinated and calcareous benthic foraminifers and bivalves from mudline samples, Site U1541. Scale bars = 100 µm unless otherwise noted. 1. Stained bivalve (both valves intact). 2. Bivalve with concentric growth lines. 3. Bivalve beak. 4. *Lagenammina* sp. 5. Stained calcareous foraminifers. 6. Stained agglutinated foraminifers. 7. Unstained calcareous foraminifers. 8. Unstained agglutinated foraminifers. 9, 10. *Reophax* sp. 11. *Astrorhiza* sp. 12, 13. *Rhabdammina* sp.

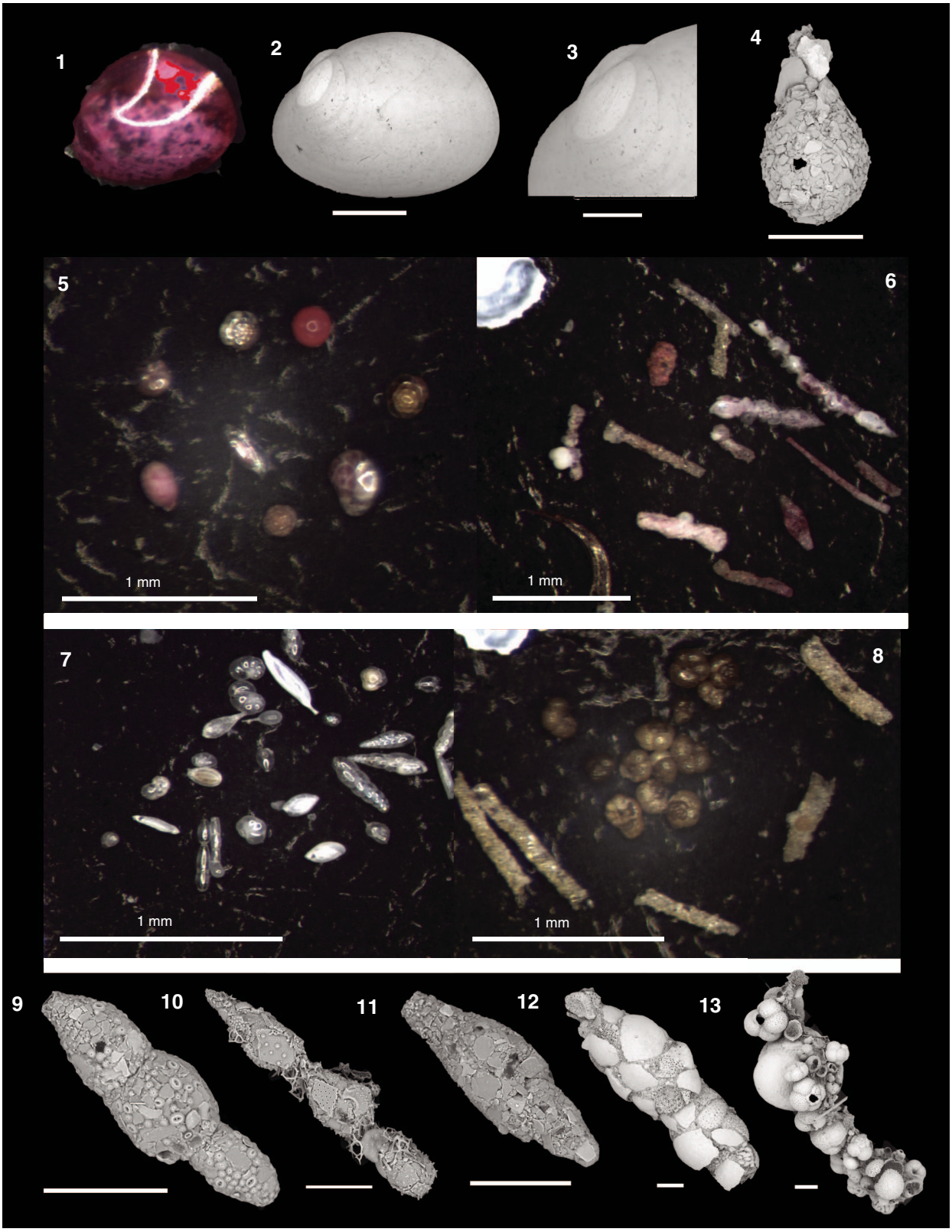

Table T10. Distribution chart of ostracods, Holes U1541A, U1541B, and U1541C. **Download table in CSV format.**

Table T11. Alternating field (AF) demagnetization steps, Site U1541. **Download table in CSV format.**

Hole	AF demagnetization steps (mT)	Cores
U1541A	0, 5, 10, 15, 20	4H, 5H
U1541B	0, 5, 10, 15, 20	1H–5H
U1541B	0, 10, 15, 20	All other cores in Hole U1541B
U1541C	0, 10, 15, 20	All cores

Paleomagnetism

The natural remanent magnetization (NRM) of archive-half core sections from Site U1541 was measured and remeasured after alternating field (AF) demagnetization at 2 cm increments. Peak AFs were restricted to a maximum of 20 mT for all sections recovered using the APC system with standard full, nonmagnetic core barrels (see **Operations**). In general, the number of demagnetization steps and the peak AF used reflect the severity of the drill string and natural overprints, the desire to use low peak fields to preserve the magnetization for future shore-based studies, and the need to maintain core flow through the laboratory. See Table **T11** for a list of AF demagnetization steps employed for each section. To maintain core flow, sections completely affected by drilling disturbance, as noted by the lithostratigraphic and/or paleomagnetic groups, were not measured. Data associated with intervals affected by obvious drilling deformation or measurement error were culled prior to uploading or during data processing.

The NRM intensities of cores recovered from Holes U1541A–U1541C range from 10^{-1} to 10^{-6} A/m (Figure **F28**). After demagnetization at a peak AF of 20 mT, the intensities are more constrained, although the pattern is complex and reflects the concentration of magnetic minerals (lithology), the polarity, and the drill string overprint. In general, reversed polarity intervals (positive inclinations) that are relatively strongly magnetized (0–5 m; below 30 m CCSF-A) show a significant drop (~50%) in intensity after a peak AF of 20 mT, whereas normal polarity intervals (negative inclination) that are relatively strongly magnetized show a much smaller decrease in intensity. This reflects the orientation of the drill string–induced overprint that is oriented down ($-z$) or positive (Richter et al., 2007) relative to the NRM's polarity. As a result, reversed (positive) polarities show a large decrease in intensity as the drill string overprint is removed, whereas removal of the overprint from normal (negative) polarities gives rise to an initial increase in intensity before the primary magnetization begins to be demagnetized. The amplitude of the intensity decline relative to the NRM intensity after peak AF demagnetization is termed Δ (for details, see **Paleomagnetism** in the Site U1540 chapter [Winckler et al., 2021b]):

$$\Delta = \frac{NRM_{lowAF} - NRM_{highAF}}{NRM_{highAF}}.$$

The Δ parameter provides an initial measure of the quality of the NRM relative to the overprint that can be used to provide guidance on the reliability of the paleomagnetic record. At Site U1541, the Δ parameter suggests that by 20 mT peak AF demagnetization, outside of a few intervals that will be discussed below, most of the drill string magnetic overprint has been removed. Low intensity intervals (5–30 m CCSF-A) (Figure **F28**), in contrast, show a large and variable (noisy) intensity decrease after demagnetization that reflects a lower coercivity magnetization combined with a low signal to noise ratio NRM giving rise to poorly resolved directions and even polarity (Figure **F29**).

Downhole NRM intensity records from Holes U1541A–U1541C are comparable (Figure **F28**). NRM intensities from the uppermost sediments are relatively high (10^{-2} to ~10^{-3} A/m), but they quickly decrease by around two orders of magnitude over the upper 10 m CCSF-A. This may be attributed to redox conditions because sulfate is rapidly decreasing (see **Geochemistry**), although the existence of thick carbonate oozes also likely contributes (see **Sedimentology**). The NRM is characterized by very low intensity (10^{-4} to 10^{-5} A/m) from ~5 to ~30 m CCSF-A. Below this interval, NRM intensities are higher and vary between 10^{-2} and 10^{-4} A/m (Figure **F28**). Overall, the downhole intensity pattern generally follows physical properties such as magnetic susceptibility (see **Sedimentology**), suggesting that NRM intensity is largely controlled by the lithology with a diagenetic overprint.

Figure **F29** shows inclination for Holes U1541A–U1541C before and after AF demagnetization at 20 mT. Inclinations capture a series of apparent polarity reversals that are consistent between Holes U1541B and U1541C where they overlap and together provide a long and almost continuous (see **Stratigraphic correlation**) record of polarity change over the past 8 My (Figures **F30**, **F31**). As stated above, polarity is less clearly observed in the upper part of the record (above 30 m CCSF-A) and is particularly problematic between 8–15 and 23–27 m CCSF-A, intervals characterized by exceedingly low signal to noise ratios. Despite these complications, the Matuyama/Brunhes and upper and lower Jaramillo polarity boundaries that define the upper part of the Matuyama Chron (C1r.1r and.1n) are observed (Figures **F29**, **F30**). Most reversal boundaries from the Olduvai Chron (C2n) to Chron C4r.1n (8.254 Ma) are generally well defined, and their positions in each hole are shown in Table **T12** and Figure **F30**. The record of inclination and intensity after 20 mT peak AF demagnetization for the splice composite record allows polarity interpretations and correlation to the geomagnetic polarity timescale (GPTS) (Cande and Kent, 1995). Only the boundaries associated with the reversed polarity intervals of the Gauss Chron (C2An) (Kaena and Mountain) and the short normal polarity Subchron C3BR.2n that spans 7.454–7.485 Ma are not clearly recognized over the 0–8.5 Ma interval. Figure **F31** illustrates the shipboard age model for Site U1541 based on correlation to the GPTS on 2012 geologic timescale (GTS2012) chronology (Hilgen et al., 2012). Shore-based studies will refine these correlations and facilitate development of relative paleointensity as the next step in magnetic stratigraphy.

Figure F28. Natural remanent magnetization (NRM) intensity before and after 20 mT peak alternating field demagnetization, Holes U1541A–U1541C.

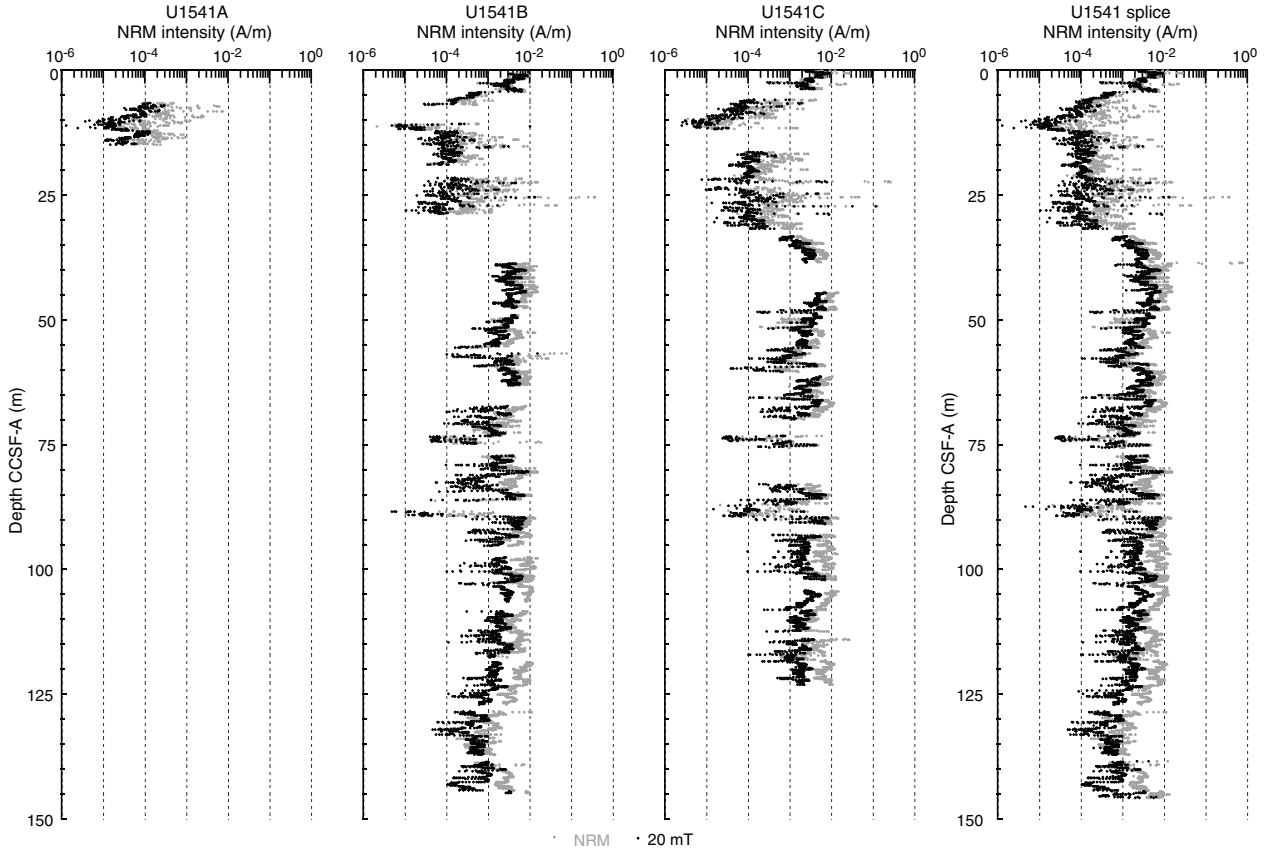

Figure F29. Inclination before and after 20 mT peak alternating field demagnetization, Holes U1541A–U1541C. NRM = natural remanent magnetization.

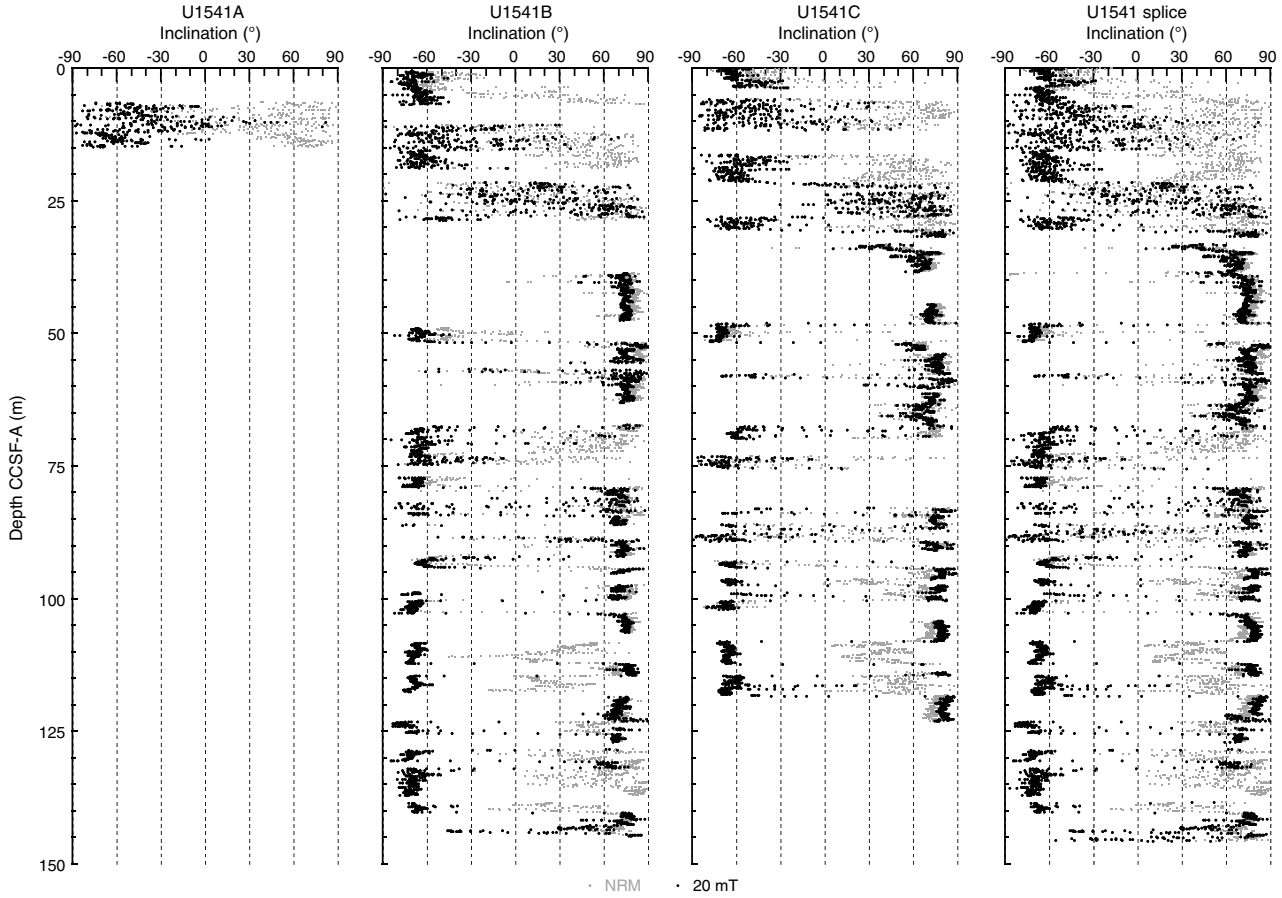

Figure F30. Natural remanent magnetization (NRM) intensity and inclination after 20 mT peak alternating field demagnetization, Site U1541. Polarity interpretation and correlation to the geomagnetic polarity timescale (GPTS; Cande and Kent, 1995) on geologic timescale of Hilgen et al. (2012; GTS2012) is discussed in text.

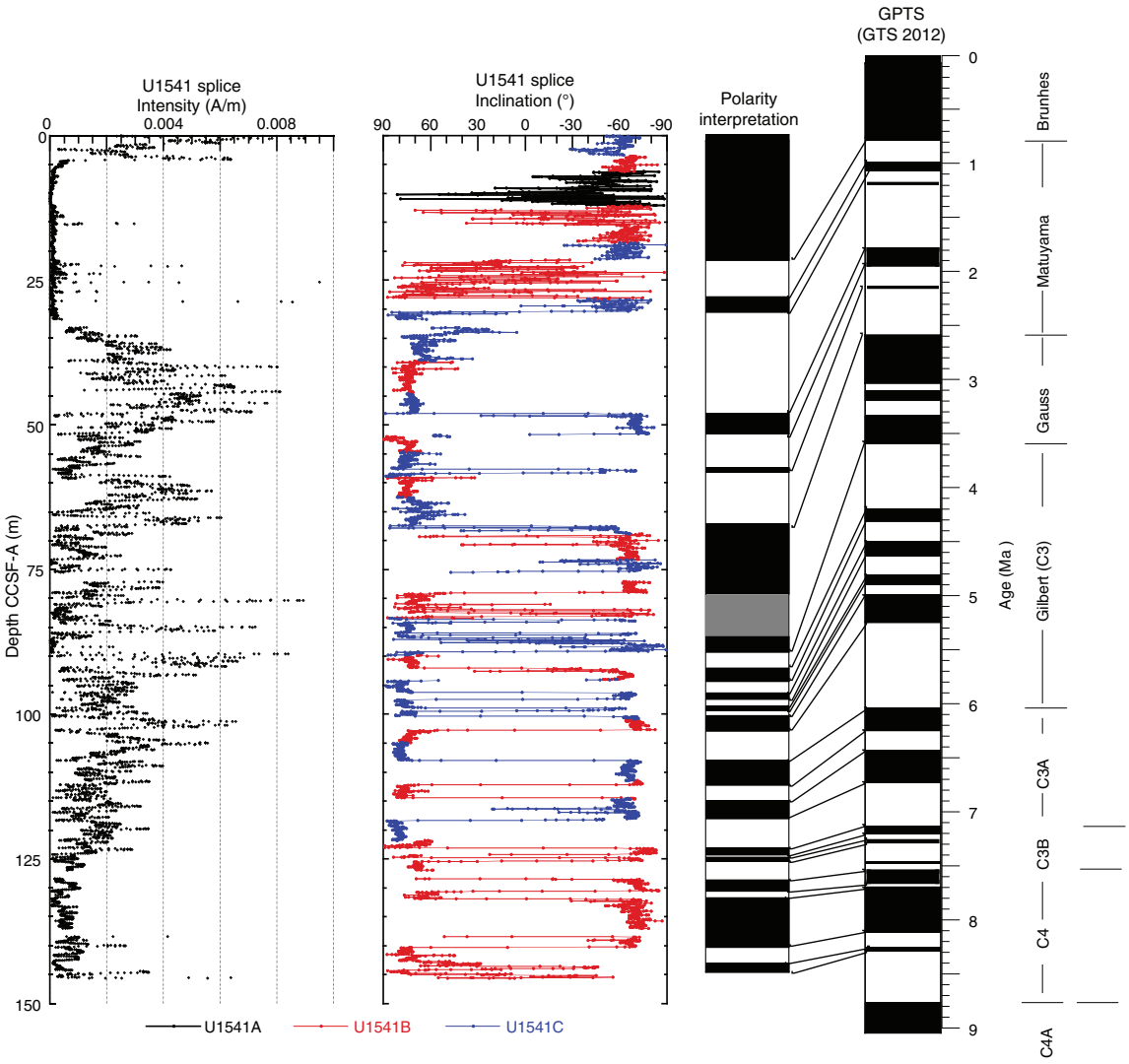

Figure F31. Age-depth relationship based on correlation to the geomagnetic polarity timescale (Cande and Kent, 1995), Holes U1541B and U1541C.

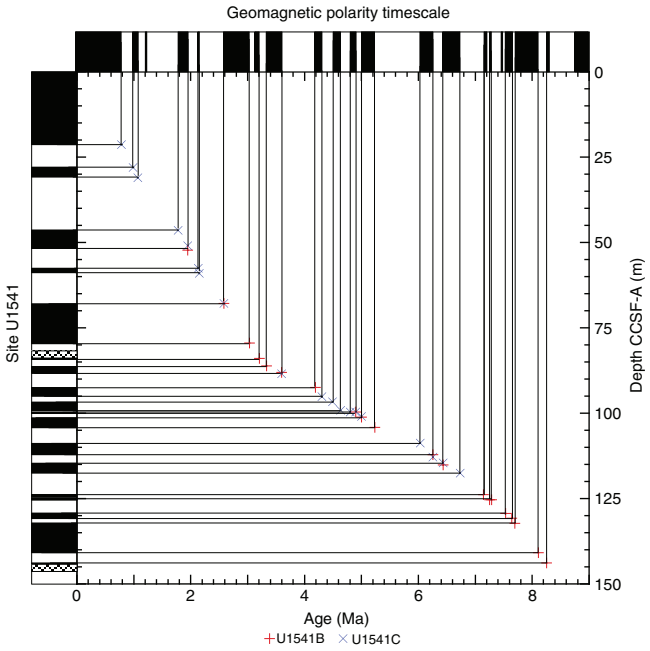

Table T12. Position of identified polarity transitions, Site U1541. GTS2012 = geomagnetic timescale of Gradstein et al. (2012). t = top. (Continued on next page.)
Download table in CSV format.

Polarity chron interpretation	Subchron	GTS 2012 Age (Ma)	Core, section	Depth CSF-A (m)	Depth (±m)	Depth CCSF-A (m)	Comment	Core, section	Depth CSF-A (m)	Depth (±m)	Depth CCSF-A (m)	Comment
			383-U1541B-					383-U1541C-				
C1r.1r (t)	Matuyama/Brunhes	0.781						3H-4/3H-5	19.4	1.35	21.28	
C1r.1n (t)	Jaramillo	0.988						4H-4	28.35	0.75	28.00	
C1r.2r (t)		1.072						4H-6	31.35	0.75	31	
C2n (t)	Olduvai	1.778						6H-2	44.35	0.75	46.44	
C2r.1r (t)		1.945	6H-4	50.35	0.75	52.21		6H-5	48.85	0.75	50.94	
C2r.1n (t)	Reunion	2.128						7H-3	55.35	0.75	57.53	
C2r.2r (t)		2.148						7H-4	56.85	0.75	59.03	
C2An.1n (t)	Gauss/Matuyama	2.581	8H-1	64.85	0.75	67.87	Reversal not clearly defined	8H-5	67.85	0.75	67.84	
C2An.1r	Kaena	3.032	9H-2	75.85	0.75	79.37		9H-2				
C2An.2n		3.116										
C2An.2r	Mammoth	3.207	9H-5	80.35	0.75	83.87	Overlying polarity not clearly defined	9H-5				
C2An.3n	Gauss	3.33	9H-7	82.6	0.3	86.12	Underlying polarity not clearly defined	9H-7				
C2Ar	Gilbert	3.596	10H-1	83.85	0.75	87.96	Overlying polarity not clearly defined	10H-1	86.1	0.75	88.48	
C3n.1n	Cochiti	4.187	10H-4	88.3	0.7	92.41		10H-4				
C3n.1r		4.3						11H-2	91.85	0.75	95.12	
C3n.2n	Nunivak	4.493						11H-3	93.35	0.75	96.62	
C3n.2r		4.631						11H-4	95.8	0.75	99.07	
C3n.3n	Sidufjall	4.799						11H-5	96.35	0.75	99.62	
C3n.3r		4.896	11H-2	94.85	0.75	99.66		11H-2	96.35	0.75	99.62	
C3n.4n	Thvera	4.997	11H-3	96.35	0.75	101.16		11H-3	97.6	0.5	100.87	
C3r	Gilbert	5.235	11H-4	99.35	0.75	104.16		11H-4				
C3An.1n		6.033						12H-4	104.35	0.75	108.68	
C3An.1r		6.252	12H-3	105.85	0.75	112.12		12H-3	108.5	0.75	112.83	
C3An.2n		6.436	12H-5	108.85	0.75	115.12		12H-5	109.35	0.75	114.50	
C3Ar		6.733						13H-3	112.35	0.75	117.50	
C3Bn		7.14	13H-4	116.85	0.75	123.80		13H-4				
C3Br.1r		7.212										
C3Br.1n		7.251	13H-5	118.35	0.75	125.30		13H-5				
C3Br.2r		7.285	13H-5	118.35	0.75	125.30		13H-5				
C3Br.2n		7.454										
C3Br.3r		7.489										
C4n.1n		7.528	14H-1	121.85	0.75	129.30	Could be C3Br.2n	14H-1				
C4n.1r		7.642	14H-2	123.3	0.75	130.75		14H-2				

Table T12 (continued).

Polarity chron interpretation	Subchron	GTS 2012 Age (Ma)	Core, section	Depth CSF-A (m)	Depth (±m)	Depth CCSF-A (m)	Comment	Core, section	Depth CSF-A (m)	Depth (±m)	Depth CCSF-A (m)	Comment
C4n.2n		7.695	14H-3	124.8	0.75	132.25		14H-3				
C4r.1r		8.108	15H-2	132.85	0.75	140.80		15H-2				
C4r.1n		8.254	15H-4	135.85	0.75	143.80		15H-4				

Geochemistry

Sediment gas sampling

Routine safety hydrocarbon measurements were collected at Site U1541 in headspace gastight vials at a resolution of approximately one 5 cm^3 sample per core for Hole U1541A (5.98 m CSF-A) and Cores 383-U1541B-1H through 15H (5.97–136.6 m CSF-A) (see **Geochemistry** in the Expedition 383 methods chapter [Winckler et al., 2021a]). Methane concentrations are low at this site overall, averaging 2.86 ppmv and never exceeding 3.47 ppmv (Figure **F32**; see U1541-T1.xlxs in GEOCHEM in **Supplementary material**). Ethane and propane remain below detection limit throughout the entire hole.

Interstitial water chemistry

At Site U1541, 37 whole rounds were collected for interstitial water samples from Holes U1541B and U1541C at a resolution of three per core from 0 to 120 m CSF-A and two per core from 120 to the bottom of the hole. Because of drilling disturbance in the upper part of the core, the interstitial water sampling strategy could not be followed as planned; only one interstitial water whole round was collected from the second core, and no whole rounds were collected from the third. A mudline sample collected from Hole U1541B was allowed to settle for several hours and was subsequently filtered through a 0.45 µm syringe-tip filter. Filtered mudline water was subjected to all standard shipboard chemistry. We squeezed whole rounds and subsampled for interstitial water according to the methods described in **Geochemistry** in the Expedition 383 methods chapter (Winckler et al., 2021a).

Alkalinity and pH

Alkalinity remains fairly constant around a mean value of 2.8 ± 0.5 (±1σ) mM to ~90 m CSF-A (Figure **F33**; see U1541-T2.xlxs in GEOCHEM in **Supplementary material**). Starting at 90.27 m CSF-A, alkalinity values show a decreasing trend to the bottom of the core at 136.55 m CSF-A. In the uppermost 32.03 m, pH values stay close to 8 (Figure **F33**). Between ~40 and 90 m CSF-A, pH values show higher variability. They decrease from 7.9 to 7.7 between ~82 and ~95 m CSF-A, and they remain stable around 7.8 thereafter.

Salinity, chlorinity, sodium, and magnesium

Salinity for all interstitial water samples is constant at 35 throughout the core. Downhole chlorinity values do not show any prominent trends and have an average value around 563 ± 7 mM (Figure **F34**). Sodium (Na) concentrations show little variability downhole. The mean Na value is ~462 ± 6 mM. Magnesium (Mg) concentrations remain unchanged with depth with a mean value of 51.3 ± 0.5 mM (Figure **F34**).

Iron, manganese, and lithium

Above 38.55 m CSF-A, dissolved iron (Fe) concentrations are largely below detection limit in the interstitial water (Figure **F35**). Between 38.55 and 90.27 m CSF-A, Fe is present in the interstitial water with significant scatter, ranging from below detection limit to a maximum concentration of 6.9 µM. Below 90.27 m CSF-A, aqueous Fe decreases in the interstitial water to below detection limit, possibly due to rapid scavenging by abundant Fe oxides at the bottom of the core. Manganese (Mn) concentrations increase sharply from below detection limit in the mudline sample to a local maxi-

Figure F32. Headspace methane concentrations, Holes U1541A and U1541B.

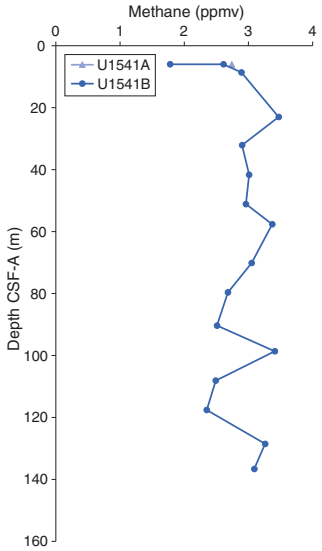

Figure F33. Interstitial water alkalinity and pH, Site U1541. Red square = overlying seawater sample.

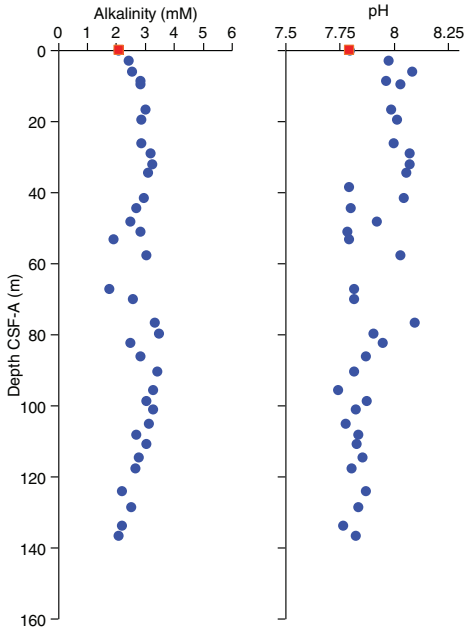

Figure F34. Interstitial water chloride, sodium, and magnesium, Site U1541. Chloride data points represent the mean of triple measurements. A few chloride measurements were discarded (hence not plotted) due to possible error at the time of measurement. Red square = overlying seawater sample.

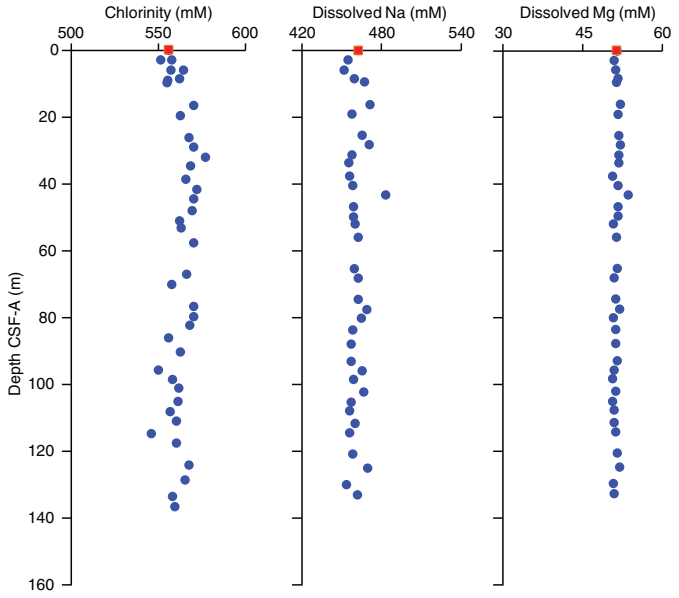

Figure F35. Interstitial water iron, manganese, and lithium, Site U1541. Red square = overlying seawater sample.

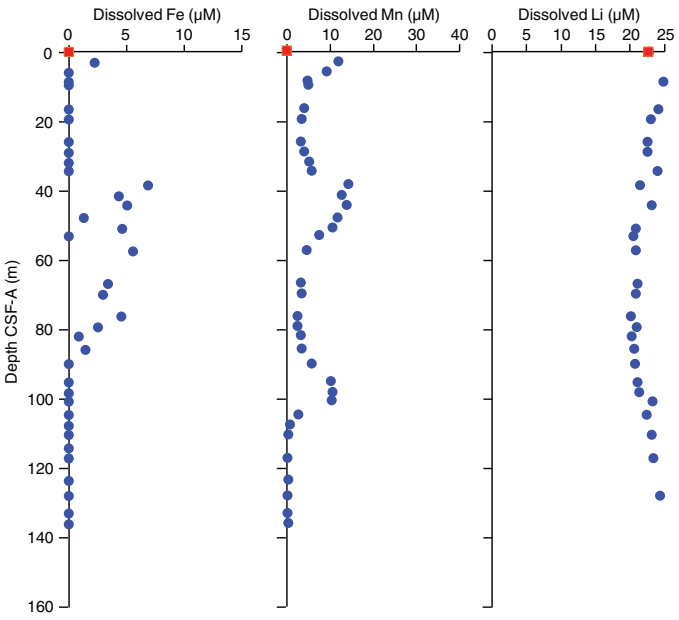

mum of 14.2 μM at 36.55 m CSF-A (Figure **F35**). Mn concentrations drop again to 2.5 μM at 79.56 m CSF-A before slowly rising to 10.2 μM at 95.55 m CSF-A. At 110.79 m CSF-A, Mn is depleted from the interstitial water to 0.3 μM in the bottommost sample, similar to the behavior of Fe in this interval. Dissolved lithium (Li) displays a nearly constant interstitial water concentration of 23.8 ± 3.3 μM with slight increase below 76.55 m CSF-A (Figure **F35**). This slight increase in Li at depth could be due to influence of hydrothermal fluid.

Figure F36. Interstitial water calcium, bromide, strontium, and silicon, Site U1541. Red square = overlying seawater sample.

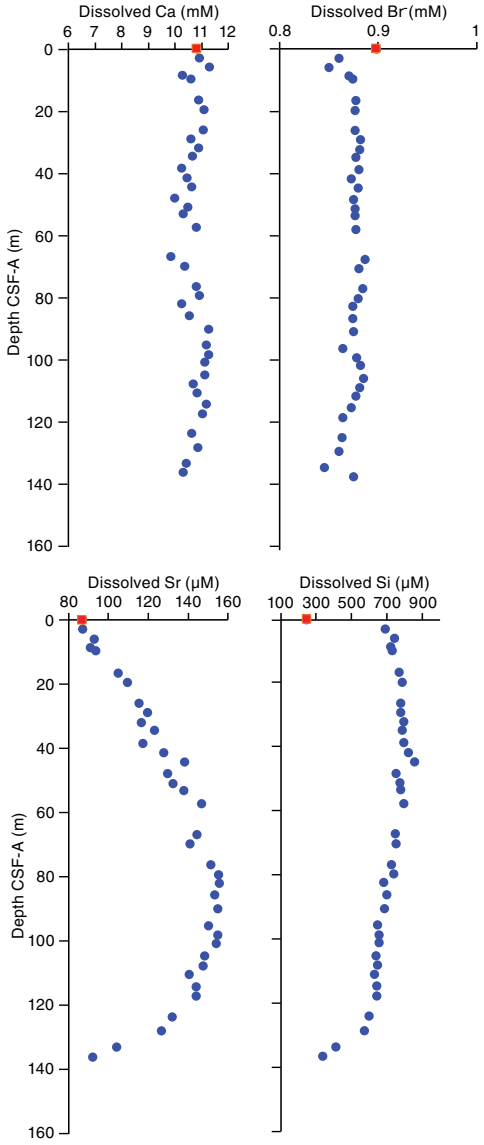

Calcium, bromide, strontium, and silicon

Calcium (Ca) and bromide (Br^-) concentrations remain fairly constant throughout the record, varying around averages of 10.7 ± 0.4 mM and 0.87 ± 0.01 mM, respectively (Figure **F36**). Strontium (Sr) increases almost linearly from a surface value of 87.1 μM to a maximum of 156 μM at 82.22 m CSF-A (Figure **F36**). Below this depth, Sr becomes progressively depleted in the interstitial water to a concentration of 92.1 μM in the bottommost sample (136.55 m CSF-A) (Figure **F36**). Dissolved silicon (Si) is low in the mudline water (246 μM) and relatively higher in the interstitial water down to 90.27 m CSF-A and has an average concentration of 757 ± 44 μM over this interval (Figure **F36**). Between 90 and 124 m CSF-A, interstitial water Si concentrations decrease gradually to 573 μM. In the lowermost four samples below 120 m CSF-A, Si exhibits a more rapid decrease to a minimum of 336 μM.

Figure F37. Interstitial water phosphate, sulfate, and ammonium, Site U1541. Red square = overlying seawater sample.

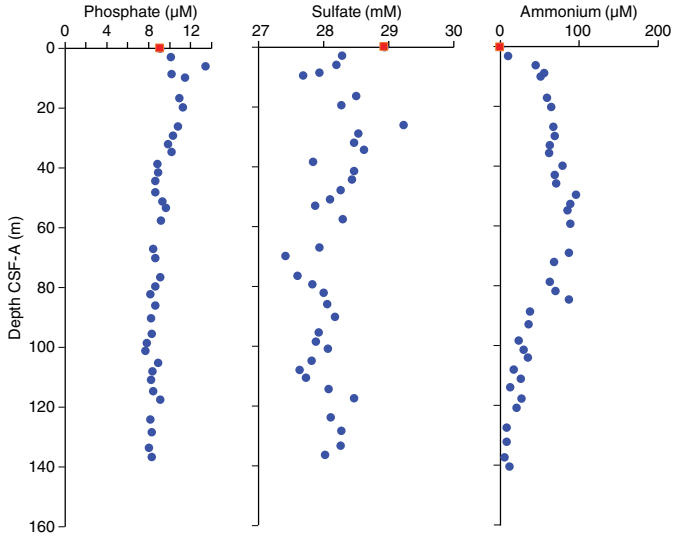

Figure F38. Interstitial water potassium, boron, and barium, Site U1541. Red square = overlying seawater sample.

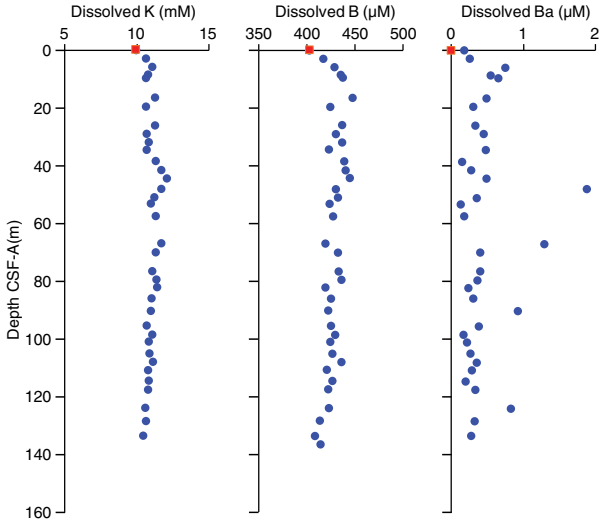

Phosphate, sulfate, and ammonium

Phosphate (PO_4^{3-}) concentrations decrease gradually with depth from an average of 10.7 ± 1.1 μM in the uppermost ~30 m to 8.4 ± 0.4 μM in the lowermost ~30 m CSF-A (Figure **F37**). Sulfate (SO_4^{2-}) concentrations are generally constant downhole with an average of 28.2 ± 0.4 mM and no prominent trends with depth despite some variability between 27 and 29 mM (Figure **F37**). Ammonium (NH_4^+) concentrations increase over the upper part of the core from below detection limit in the mudline sample to 95.6 μM at 49.06 m CSF-A (Figure **F37**). Below this depth, NH_4^+ decreases to a minimum of 5.5 μM at 133.55 m CSF-A. The increase in NH_4^+ in the upper layers of sediment could be related to NH_4^+ accumulation in interstitial water due to organic matter remineralization. The decreasing trend at depth might suggest presence of anaerobic oxidation of NH_4^+, perhaps through interactions with hydrothermal material and/or basalt.

Potassium, boron, and barium

Dissolved potassium (K) is generally constant in the interstitial water with depth and has an average concentration of 11.0 ± 0.4 mM (Figure **F38**). Boron concentrations exhibit a slight increase in the uppermost sediment, from 403 μM in the mudline sample to 448 μM at 16.56 m CSF-A, below which depth concentrations remain constant around an average of 428 ± 8 μM (Figure **F38**). Barium (Ba) concentrations are low in the interstitial water and between 0.13 and 0.55 μM throughout the record, with the exception of four higher values of 0.75 μM at 5.92 m CSF-A, 1.29 μM at 67.05 m CSF-A, 0.93 μM at 90.27 m CSF-A, and 0.83 μM at 124 m CSF-A (Figure **F38**).

Bulk sediment

Calcium carbonate

Calcium carbonate ($CaCO_3$) concentration measurements for Hole U1541B were obtained with a resolution of three samples per core except for Cores 383-U1541B-2H, 3H, 6H, and 7H, from which two samples per core were taken instead. For Hole U1541A, three $CaCO_3$ samples were obtained from the one recovered core. The composite $CaCO_3$ record of Holes U1541A and U1541B has a mean value of 68.6 wt% and a downhole variability ranging from 21.6 wt% at 1.1 m CSF-A to 92.7 wt% at 5.19 m CSF-A in Hole U1541A (Figure **F39**; see U1541-T3.xlxs in GEOCHEM in **Supplementary material**). $CaCO_3$ measurements show a strong correlation with blue color intensity and color reflectance (L*) measurements (see **Sedimentology**).

Major and trace elements

A total of 16 samples taken for $CaCO_3$ analyses from Holes U1541A and U1541B were also analyzed for major and minor element concentrations using inductively coupled plasma–atomic emission spectroscopy (ICP-AES) (see U1541-T4.xlxs in GEOCHEM in **Supplementary material**). Elemental oxides (namely MgO, K_2O, Fe_2O_3, SiO_2, and TiO_2) show a strong positive correlation with a near zero intercept when plotted against aluminum oxides (Al_2O_3) (Figure **F40**). This correlation could indicate the presence of micaceous/clay minerals. In contrast, plots of Al_2O_3 versus MnO and P_2O_5 do not show any well-defined relation. Mn is a redox sensitive element and is also removed as carbonate minerals precipitate (Calvert and Pedersen, 1994). Precipitation of Mn carbonate might explain the lack of correlation between MnO and Al_2O_3. CaO shows a positive correlation against Al_2O_3.

Below 100 m CSF-A, measured Al, K, Fe, Ba, Mg, titanium (Ti), zinc (Zn), and zircon (Zr) in bulk sediment decrease in concentration in relation to their concentration values in the shallower sediments (Figure **F41**). Mn concentrations, however, show an abrupt increase between ~98 and 124 m CSF-A and a maximum of 1595 ppm at ~105 m CSF-A. The Mn concentration profile above 100 m CSF-A remains relatively constant at ~ 405 ppm. Most measured elements show an increase in the bottom sample at 135.85 m CSF-A (Figure **F41**), possibly indicating the influence of hydrothermal alteration or basaltic basement interactions on sediment composition. Downhole Sr and Ca concentrations show a strong similarity (Figure **F41**). Bulk sediment Ca primarily represents biogenic $CaCO_3$; hence, covariation of Sr and Ca can be attributed to incorporation of Sr in biogenic $CaCO_3$.

Figure F39. A–D. Solid phase geochemistry of (A) $CaCO_3$, (B) total organic carbon (TOC):total nitrogen (TN), (C) TN, and (D) TOC, Holes U1541A and U1541B. Gray bar = sample overlap.

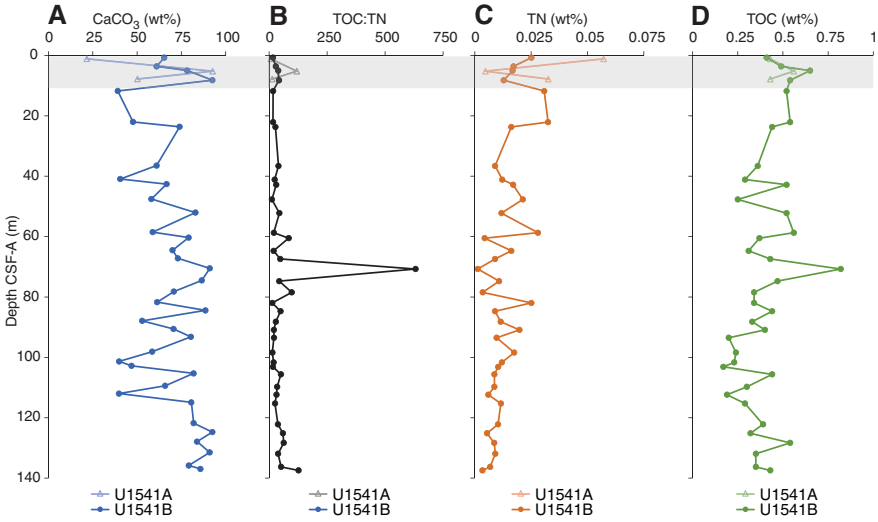

Figure F40. Bulk sediment elemental (Na, K, Si, P, Mg, Ca, Ti, Mn, and Fe) oxides vs. aluminum oxide (Al_2O_3), Site U1541.

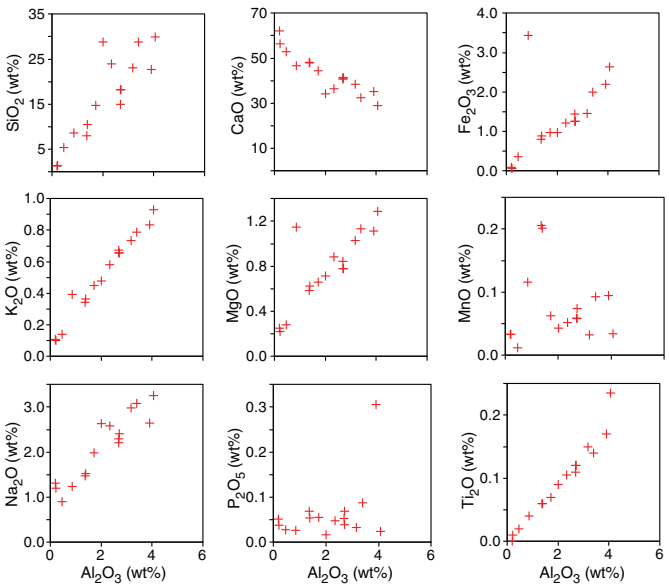

Figure F41. Bulk sediment major and minor element concentrations, Site U1541.

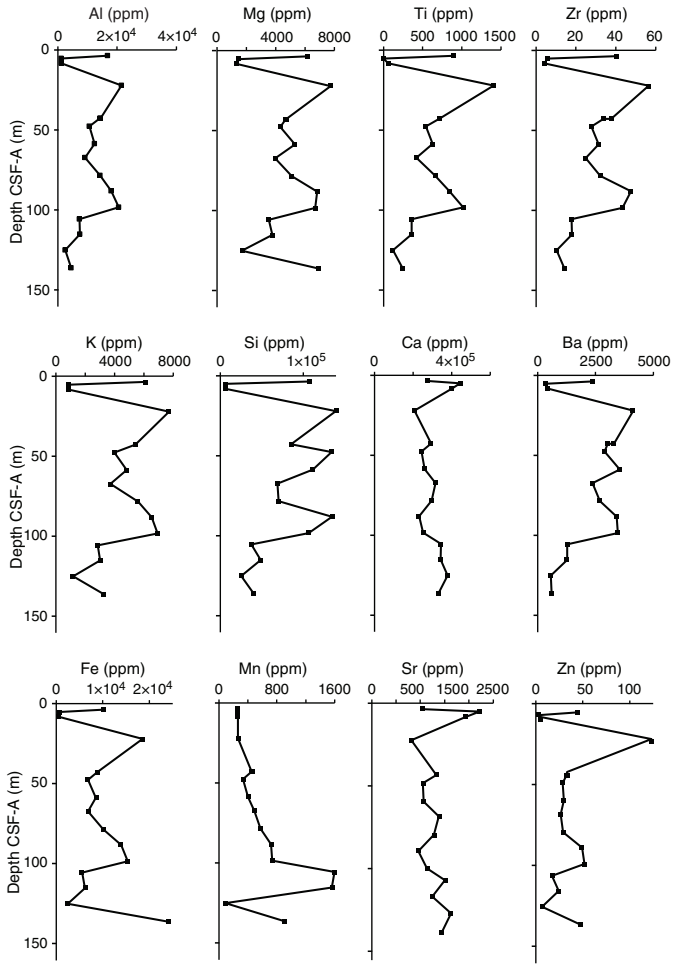

Organic carbon

All samples analyzed for $CaCO_3$ were additionally subsampled for total carbon (TC) analysis. Total organic carbon (TOC) estimates were obtained by measuring the TC and subtracting the contribution of inorganic $CaCO_3$ (see **Sedimentary inorganic and organic carbon, nitrogen, and carbonate content** in the Expedition 383 methods chapter [Winckler et al., 2021a]). The composite TOC record of Holes U1541A and U1541B shows a mean of 0.4 wt% and downhole variability ranging from 0.2 to 0.8 wt% (Figure **F39**; see U1541-T3.xlxs in GEOCHEM in **Supplementary material**). Considering the low mean TOC of 0.4 wt% at Site U1541, the relatively high standard deviation of internal standards (see **Geochem-**

istry in the Expedition 383 methods chapter [Winckler et al., 2021a]) produces high percent error in TOC measurements. Further shore-based analyses are required to refine these findings. The TOC record shows little correlation to the $CaCO_3$ record (r^2 = 0.11) downhole.

Total nitrogen

Samples were measured for total nitrogen (TN) simultaneously with TC. It was assumed that all the nitrogen detected in the sediment was organic in origin. The composite TN record of Holes U1541A and U1541B has a mean of 0.015 wt% and shows downhole variability ranging from 0.001 to 0.057 wt% (Figure **F39**; see U1541-T3.xlxs in GEOCHEM in **Supplementary material**). The net amplitude of TN variability and overall TN concentration decrease slightly downhole. The upper portion of the core between 0.7 and 81.71 m CSF-A has a mean TN value of 0.016 ± 0.009 wt%. The lower portion of the core from 84.45 to 137.00 m CSF-A has a mean TN value of 0.01 ± 0.004 wt%. These small values likely fall below the accurate detection limit of the instrument, given the relatively high standard deviation of internal standards (see **Geochemistry** in the Expedition 383 methods chapter [Winckler et al., 2021a]), and should therefore be interpreted with caution until shore-based analyses are collected. Therefore, the error associated with these low concentration measurements is too high for interpretation.

Organic carbon to organic nitrogen ratios

The ratio of TOC to TN from the composite record of Holes U1541A and U1541B has a mean value of 53 and shows downhole variability ranging from 7.5 to 630.8 (Figure **F39**; see U1541-T3.xlxs in GEOCHEM in **Supplementary material**). The maximum TOC:TN value coincides with a TN of 0.001 wt%, which falls below the detection limit of the elemental analyzer. This sample was run in duplicate to test results, and the difference in TOC:TN ratio between duplicates was 5.7. Excluding this peak, mean TOC:TN downhole is 38.1, which suggests that organic matter throughout Site U1541 derives from terrestrial sources (Meyers, 1994, 1997). Only one TOC:TN value of 7.5 falls within the range of algal-derived organic matter at 1.1 m CSF-A. All analyses should be interpreted with caution, however, because of the low TN detected at Site U1541.

Summary

The interstitial water composition is marked by an increase in alkalinity and pH in the upper ~5–8 m. This could have been caused by anaerobic organic matter oxidation through reduction of Mn oxides, Fe oxides, or SO_4^{2-} (Soetaert et al., 2007), which might also explain the peak in dissolved Mn concentration at the surface. Decreasing trends in alkalinity and pH values below ~80 m CSF-A indicate the presence of chemical reactions that are supported in a hydrothermal setting (German and Von Damm, 2003). Fe concentrations are below detection limit deeper than 86.05 m CSF-A and could suggest precipitation of authigenic Fe or adsorption onto existing Fe oxides. Mn concentrations also show near zero values below 105.05 m CSF-A, indicating possible precipitation of Fe-Mn oxides/hydroxides or adsorption of Mn to Fe-oxides; scenarios consistent with Fe-Mn-rich hydrothermal fluid interacts with overlying seawater. The slight increase in Li concentration in the bottom sample might also indicate influence of hydrothermal fluid because hydrothermal input is one of the primary sources of Li to the oceanic Li budget. Should hydrothermal fluid dominate the interstitial water chemistry, we would expect high Si in the deeper part of the record. In contrast, Si concentrations tend to decrease in the bottom sections of the record, indicating that clay mineralogy or diagenetic reactions might have played a bigger role in shaping the interstitial water Si concentration profile. Given that the site is close to a hydrothermal ridge and the basement rock has been identified as basalt, interstitial water chemistry at depth (e.g., >80 m CSF-A) might represent some vestigial product of seawater-hydrothermal fluid-basalt interaction.

$CaCO_3$ content is relatively high at this site. It never falls below 21.6 wt% and has a downhole average content of 68.6 wt%. TOC does not exceed 0.8 wt% and shows no clear correlation with $CaCO_3$ content. TN is very low at this site, never exceeding 0.06 wt%, and low concentrations yield poor reproducibility of samples due to instrumental detection limits. The ratio of TOC:TN ranges between 7.5 and 126.4, with the exception of one major peak at 630.7. Therefore, mean values suggest a predominance of terrestrial input to the organic component of the sediment. However, the very high values (excluding the peak of TOC:TN at 70.5 m CSF-A) of the TOC:TN ratios are likely related to the extremely low values and poor reproducibility of TN measurements.

The bulk sediment elemental composition shows a marked increase in the contents of all metals toward the bottom of Hole U1541B at 135.85 m CSF-A, indicating interaction between basement rocks with the sediment. Oxide contents of Mg, K, Fe, Si, and Ti co-vary strongly with Al oxides, suggesting that these elements are present primarily in clay minerals. High coherency between downhole Ca and Sr concentrations suggest that Sr is incorporated in biogenic $CaCO_3$.

Physical properties

Shipboard physical properties measured at Site U1541 comprise nondestructive whole-round measurements of GRA bulk density, magnetic susceptibility (MS), *P*-wave velocity using the Whole-Round Multisensor Logger (WRMSL) and NGR measurements on core sections from Holes U1541A–U1541C. Additional physical property data collected include thermal conductivity using a needle probe on whole-round core sections from Holes U1541B and U1541C. To support stratigraphic correlation and optimize drilling depths at subsequent holes to cover coring gaps, MS and GRA data were acquired while drilling Holes U1541A–U1541C before temperature equilibration using the Special Task Multisensor Logger (STMSL) at a 3 cm resolution with a 1 s GRA acquisition time and one MS measurement. The STMSL data were stored in the International Ocean Discovery Program Laboratory Information Management System (LIMS), but further use is discouraged because the more complete WRMSL and Section Half Multisensor Logger (SHMSL) data from all core sections also are available in LIMS. WRMSL measurements were carried out on all recovered sections, including sections with incompletely filled liners or partially water-filled sections. WRMSL data were processed to indicate measurements that were not representative of the sediment characteristics (see **Physical Properties** in the Expedition 383 methods chapter [Winckler et al., 2021a]). A number of discrete X-ray fluorescence (XRF) measurements were done on selected cores from Holes U1541B and U1541C.

After splitting the core sections, discrete samples were taken from the working halves representative of the defined lithostratigraphic units for moisture and density (MAD) measurements to determine porosity and bulk, dry, and grain density from Holes U1541A and U1541B. Discrete compressional wave velocity mea-

Figure F42. Splice data, Site U1541: Whole-Round Multisensor Logger (WRMSL) magnetic susceptibility (MS) (red) and Section Half Multisensor Logger (SHMSL) point magnetic susceptibility (MSP) (orange). Black vertical lines = lithostratigraphic unit boundaries (see Sedimentology).

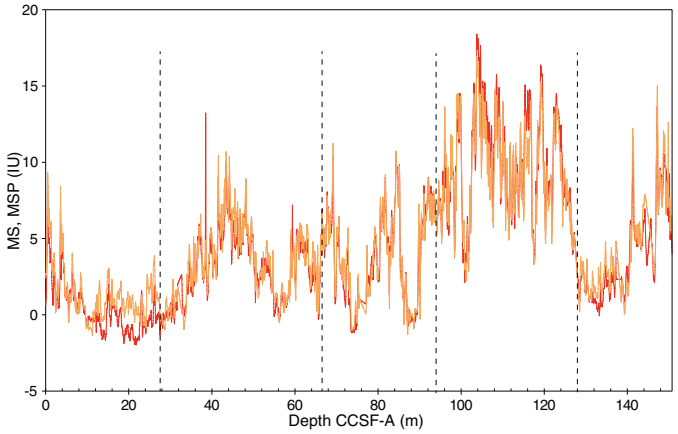

surements were conducted on at least one working half of each core using the *P*-wave caliper (PWC) contact probe system on the Section Half Measurement Gantry (SHMG). Archive halves were measured with the SHMSL for MS and color reflectance (see **Sedimentology**).

Physical property data were used for hole-to-hole stratigraphic correlation and splicing (see **Stratigraphic correlation**). In line with the pelagic lithology at Site U1541, multiple physical property parameters display long-term cyclic changes and variability throughout the recovered strata. They generally correlate well with the alternating lithologies at Site U1541 over both short (e.g., less than a meter) and longer (e.g., several to tens of meters) timescales.

Magnetic susceptibility

Both whole-round measurements on the WRMSL and discrete point measurements on the SHMSL were used to characterize MS at Site U1541 (Figure **F42**). Both methods yielded a similar range of values and similar downhole variability. Values range from −2 to 18.5 IU (see **Physical properties** in the Expedition 383 methods chapter [Winckler et al., 2021a] for details on instrument units [IU; ~10^{-5} SI]) for the WRMSL and from −1 to 17 IU for the SHMSL. High values of >30 IU are attributed to individual outsized clasts or dropstones and are not representative of the overall sediment composition. At the top of some cores, high MS values are associated with identified dropstones that likely fell from the sides of the hole and accumulated at the bottom during the drilling process and thus were sampled at the top of these cores (e.g., Sections 383-U1541B-4H-1, 6H-1, and 7H-1). These sections, considered artifacts from the drilling, were removed from the spliced record in Figure **F42**. MS is higher at 34–54, 59–72, 77.2–85.3, and 89.6–127.5 m CCSF-A and below 140.7 m CCSF-A. The highest values in the MS record correspond to Lithostratigraphic Subunit IIIA. The increase of susceptibility values is observed at the transition from Subunit IIIB to Subunit IIIA at 127.51 m CCSF-A and corresponds to a transition from nannofossil ooze (Lithofacies 4) to diatom-rich nannofossil ooze (Lithofacies 3) (Figure **F42**) (see **Sedimentology**). This period of high susceptibility values extends to 89.65 m CCSF-A in Unit II, and the decrease corresponds to a transition from Lithofacies 3 to Lithofacies 4. Transitions in MS on depth scales of a few meters to tens of meters correspond generally to lithofacies changes. Diatom ooze (Lithofacies 2) or diatom-rich nannofossil ooze (Lithofacies 3)

Figure F43. Splice data, Site U1541: density-normalized natural gamma radiation (NGR)-derived bulk density (NGR/gamma ray attenuation [GRA]).

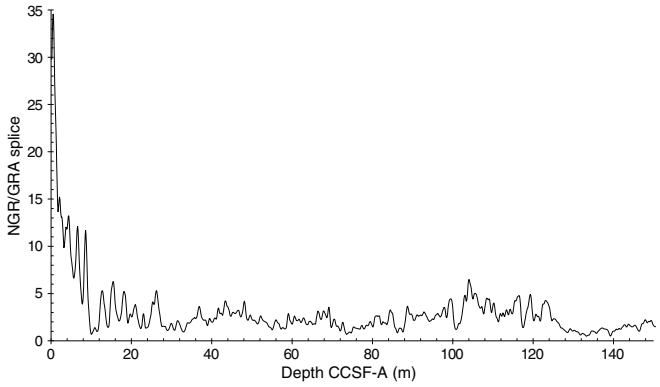

Figure F44. Splice data, Site U1541: density-normalized natural gamma radiation (NGR) (NGR/gamma radiation [GRA], black) with Whole-Round Multisensor Logger (WRMSL) magnetic susceptibility (MS) (red) and Section Half Multisensor Logger (SHMSL) point magnetic susceptibility (MSP) (orange). Black vertical lines = lithostratigraphic unit boundaries (see Sedimentology).

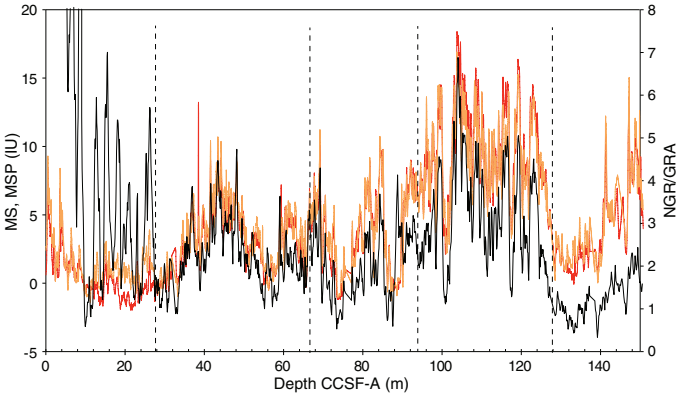

are associated with higher susceptibility values, and diatom-bearing and pure nannofossil ooze (Lithofacies 3 and 4, respectively) are typically associated with lower susceptibility values. This might indicate that increased diatom presence is generally associated with enhanced clay or ice-rafted debris transport to the site. Two notable exceptions are observed, one in the Lithofacies 4 portion of Core 383-U1541B-9H, representing the later part of the warm Pliocene where high susceptibility is associated with carbonate-bearing nannofossil ooze, and the other near the bottom of the site where high susceptibility is associated with nannofossil ooze (Lithofacies 4) and clay-bearing biogenic ooze (Lithofacies 6).

Natural gamma radiation

NGR density-normalized measurements show downhole variations between about 4 and 35 counts/s, and the highest values are from the uppermost 10 m (Figure **F43**). NGR variations match well with MS variations except for one NGR peak at 88.7 m CCSF-A that coincides with a MS minimum (Figure **F44**).

In addition, we deconvolved Site U1541 NGR counts into low-resolution (semi)quantitative concentrations for the elements K, Th, and U (Figure **F45**), following the methods of Dunlea et al. (2013) and De Vleeschouwer et al. (2017). All three elements follow similar patterns, exhibit clear cyclic peaks, and correlate well with MS values. Although U and Th show less pronounced peaks than K because of

Figure F45. Splice data, Site U1541: K (black), U (blue), and Th (red) semiquantitatively derived from natural gamma radiation (NGR). Black vertical lines = lithostratigraphic unit boundaries (see Sedimentology).

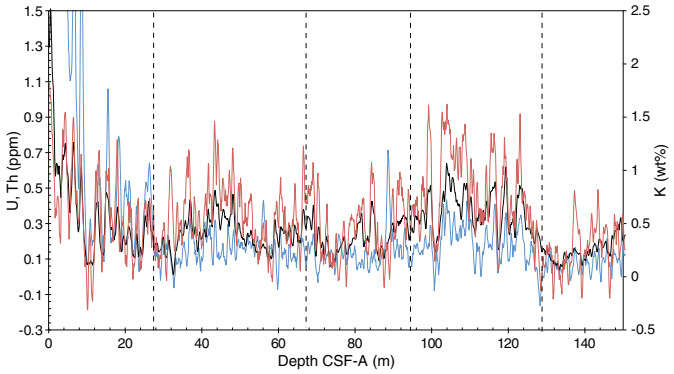

their lower concentrations and maximum attainable resolution in the NGR data, they may provide initial information about sedimentation regime changes and sediment redox conditions (e.g., Jacobel et al., 2017). Higher total NGR counts, as well as the individual elemental data, which most likely indicate higher contents of siliciclastic material (primarily clay minerals), correlate with maxima in MS. The peak at 88.7 m CCSF-A described above corresponds to a peak in U that does not show up in Th or K of the NGR deconvolved records. The U peak at Site U1541 appears to match a U peak observed at Site U1540 (210.9 m CCSF-A) and likely represents a peak in authigenic U.

Measurements with a portable XRF spectrometer were performed on selected cores from Hole U1541C (Figure **F46**). K analyses are in good agreement with NGR-derived K concentrations and show similar variability, except in the upper part of the record where NGR indicates high values that might not be representative of K concentrations.

Bulk density, grain density, and porosity

We used GRA measurements at 2 cm spacing and discrete MAD values (44 samples) to evaluate changes in bulk density at Site U1541. GRA bulk density values throughout Holes U1541A and U1541C vary from 1.2 to ~1.85 g/cm^3, and discrete MAD values range from 1.27 to 1.78 g/cm^3 (Figure **F47**). Bulk density calculated from discrete MAD samples correlates well with the GRA and displays similar downhole trends in Holes U1541A and U1541C, leading to a high correlation coefficient of r^2 = 0.94 between both methods across all encountered lithofacies (Figure **F47**). The highest GRA values (1.55–1.86 g/cm^3) occur in the lowermost Miocene Subunit IIIB and are higher than the GRA values measured at Sites U1539 and U1540, where these older sediments were not recovered. Subunit IIIB and the central part of Unit II, which mainly correspond to Lithofacies 4, represent higher density values and lower-frequency changes than Unit I and Subunit IIIA, where the relative fraction of diatom and nannofossil content alternates. Where the diatom content varies most, in Lithofacies 2 and 3, GRA undergoes large and rapid variations. In Subunits IA and IB, large-amplitude GRA variations are linked to the alternation of diatom ooze (Lithofacies 2) during glacial periods and to diatom-bearing nannofossil oozes (Lithofacies 3) during interglacial periods. Although the GRA record displays changes over several meters in Subunit IA and the top part of Subunit IB, higher frequencies (~1 m) are seen in the GRA record in Subunit IB and in the lowermost meters of Unit II, probably corresponding to the 40 ka world of the early Pleistocene.

Figure F46. Natural gamma radiation (NGR)-derived K (black line) and discrete measurements of K (blue diamonds) from the portable X-ray fluorescence (XRF) spectrometer, Hole U1541C. Top: correlation between NGR and XRF K measurements. Red triangles = first four sections of the hole, blue diamonds = deeper cores. Regression line and equation correspond to the blue dots.

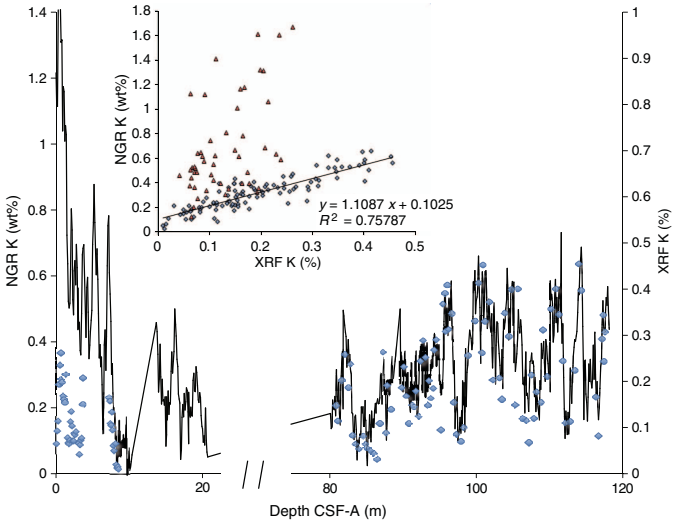

Figure F47. Whole-Round Multisensor Logger (WRMSL) gamma ray attenuation (GRA) bulk density raw (blue dashed line) and processed (blue solid line), Holes U1541A and U1541B. Black/blue diamonds = discrete moisture and density (MAD) measurements. Upper panel: correlation between MAD- and GRA-derived bulk density data.

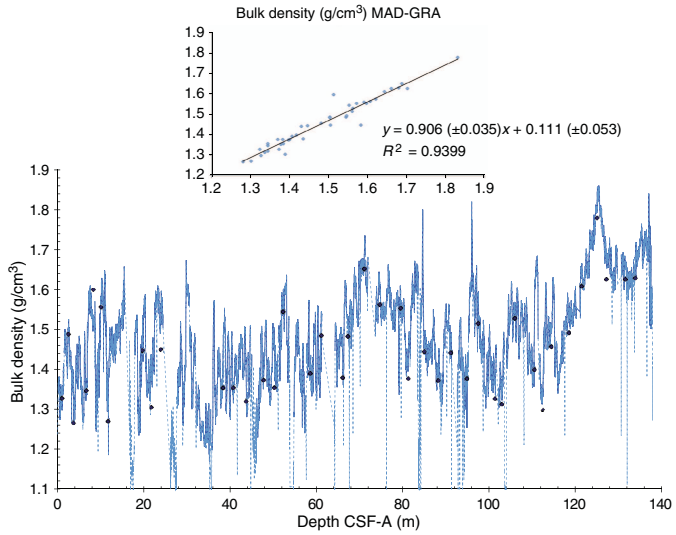

GRA results strongly correlate with the carbonate content (r^2 = 0.81) from Unit I through Subunit IIIA. Including Subunit IIIB, the correlation coefficient decreases to 0.77 because of higher GRA values for similar high carbonate content. In Subunit IIIA and through most of Unit II, GRA and MS are highly anticorrelated (Figure **F48**). This was also observed in the Pliocene interval at Site U1540. Diatoms are present in these units but are less abundant, resulting in lower amplitude variability in GRA. Probably the lower accumulation of ice-rafted debris and dropstones in those units removes the correlated presence of some MS and GRA peaks as seen in Unit I.

Figure F48. Splice data, Site U1541: processed gamma ray attenuation (GRA) bulk density (blue) and Whole-Round Multisensor Logger (WRMSL) magnetic susceptibility (MS) (inverted axis, red). Black vertical lines = lithostratigraphic unit boundaries (see Sedimentology).

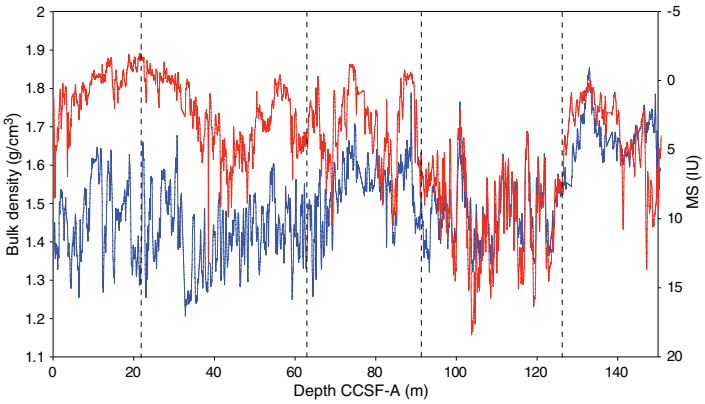

Figure F49. Top: Whole-Round Multisensor Logger (WRMSL) *P*-wave data (blue dashed line = raw data, blue solid line = processed data) and discrete *P*-wave caliper (PWC) measurements (black/blue dots), Holes U1541B and U1541C. Lower left: WRMSL *P*-wave logger (PWL) and PWC measurements. Lower right: correlation between caliper (*x*-axis) and WRMSL results. Red point = outlier not considered for the correlation.

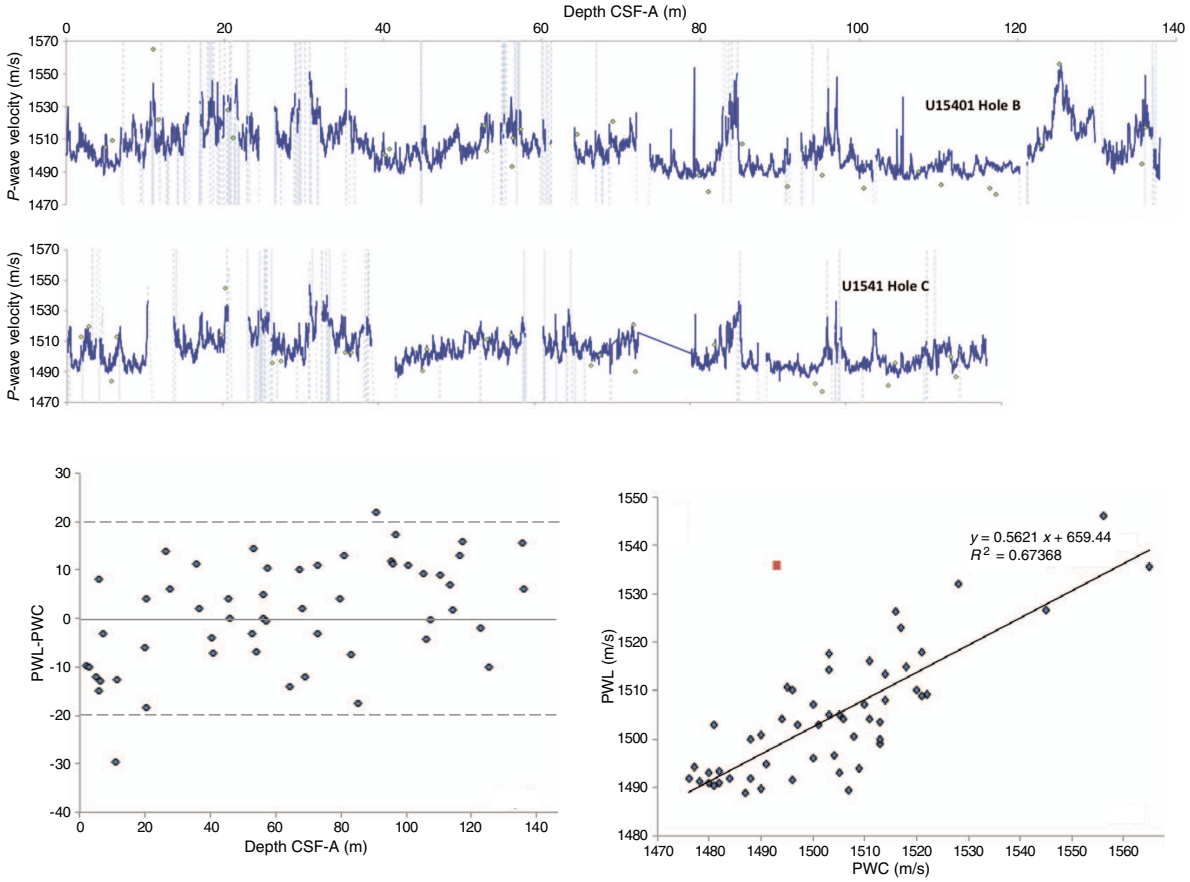

In addition to bulk density, MAD measurements provide estimates of dry density, grain density, porosity, water content, void ratio, and several other properties, which co-vary downhole. Bulk density and porosity are anticorrelated. Intervals of high porosity and water content and low grain density correspond to diatom-rich oozes (Lithofacies 2 and 3). Intervals of low porosity and high density correspond to carbonate-bearing to carbonate-dominated lithologies (Lithofacies 3, 4, and 6). Water content varies from 38% to 68% throughout the site, except for the lowest 30 m, where values are ≤40%.

Compressional *P*-wave velocity

P-wave measurements from the WRMSL indicate moderate variations from 1485 to 1555 m/s (Figure **F49**). The measurements carried out using the PWC on working halves vary from 1475 to 1565 m/s, indicating a higher range of velocity values than the measurements made on the whole-round sections, but a linear relationship is observed between the whole- and half-core analyses with a r^2 correlation coefficient of 0.674 (Figure **F49**). The difference between the PWC and the WRMSL measurements is within 20 m/s,

Figure F50. Splice data, Site U1541: Whole-Round Multisensor Logger (WRMSL) gamma ray attenuation (GRA) bulk density processed (green) and *P*-wave velocity (blue). Black vertical lines = lithostratigraphic unit boundaries (see Sedimentology).

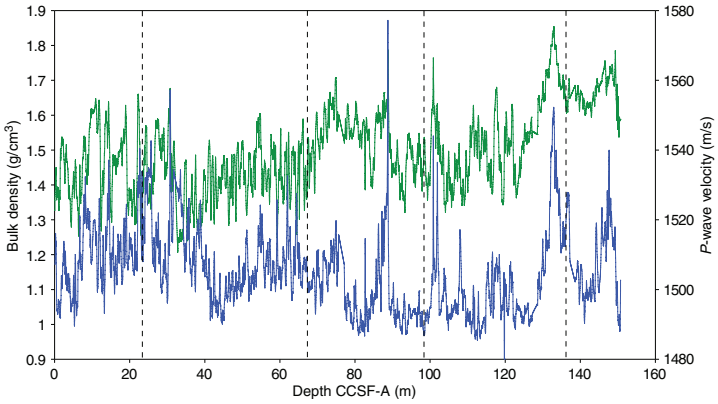

which is lower than the indicated reproducibility for the caliper, which is ± 40 m/s (Figure **F49**). Clear oscillations and cycles like those occurring in other physical properties are observed within the three holes: shorter term variations in Unit I and longer term variations in Units II and III. The relationship between *P*-wave velocity and GRA changes throughout the site (Figure **F50**). In Lithofacies 4 (pure nannofossil ooze), *P*-wave velocity is linked to density, as in Subunit IIIB, except for the diatom-bearing interval at 136.5 m CCSF-A (129.5 m CSF-A) in Hole U1541B. The relationship between GRA and *P*-wave velocity changes throughout the core from a positive to negative correlation. *P*-wave velocity varies with diatom content, and higher velocities correspond to higher diatom content. When diatoms are absent or at a constant percent content in nannofossil ooze, then *P*-wave velocity varies with density.

Thermal conductivity

Thermal conductivity was measured on all cores from Holes U1541A–U1541C with mostly two measurements, sometimes one, per core (Figure **F51**). A low value of 0.5 W was used for the needle probe. Measurements were carried out using the needle probe on the whole-round sections. For each depth, three replicates were measured. At six depths, one of the duplicate measurements failed (not plotted). The standard deviation was >5% at another five depths. Thus, the remaining 44 measurements should be reliable.

Across all holes at Site U1541, thermal conductivity ranges from ~0.72 to 1.24 W/(m·K) with a mean value of 0.978 W/(m·K). In general, diatom-rich oozes (Lithofacies 2; Subunits IA and IB) are characterized by low thermal conductivity and carbonate facies (Lithofacies 3 and 4) are characterized by higher thermal conductivity. The mean thermal conductivity is 0.907 W/(m·K) for Unit I, which alternates between Lithofacies 2 and 3, and 1.033 W/(m·K) for Units II and III (>70 m CSF-A) (Figure **F51**), which are dominated by Lithofacies 3 and 4. This highest thermal conductivity occurs in Unit II and Subunit IIIB where Lithofacies 4 dominates. Thermal conductivity mean values may indicate that thermal conductivity follows a pattern similar to GRA, with high values (>1.21 W/[m·K]) corresponding to the GRA values >1.6g/cm^3 (Figure **F51**).

Summary

Data acquired from whole-round measurements for Site U1541 are generally in good agreement with those from split-core measurements (Figures **F42**, **F47**, **F49**). GRA and WRMSL *P*-wave logger data indicate shorter term variations in Unit I and at the top of Unit II, and the shortest term variations at the top of Unit II and in Unit IB are probably linked to the 40 ka world of the early Pleistocene. MS has both high amplitude and large timescale variability all the record. Higher GRA values in Unit II and Subunit IIIB correspond to a higher fraction of carbonate/nannofossils compared to diatoms, whereas higher values of MS and NGR in Subunit IIIA are likely linked to higher terrigenous content.

Downhole changes in physical property characteristics overall are in good agreement with the defined lithofacies based on sedimentologic characteristics but show different relationships with one another than at the two previous sites (U1539 and U1540) in intervals of low diatom content.

Figure F51. Thermal conductivity data from needle probe measurements, Site U1541. 0.5 W heating power over 80 s interval. Light blue diamonds = mean values, light blue dots = individual measurements, light green dashed line = GRA density record for Hole U1541B.

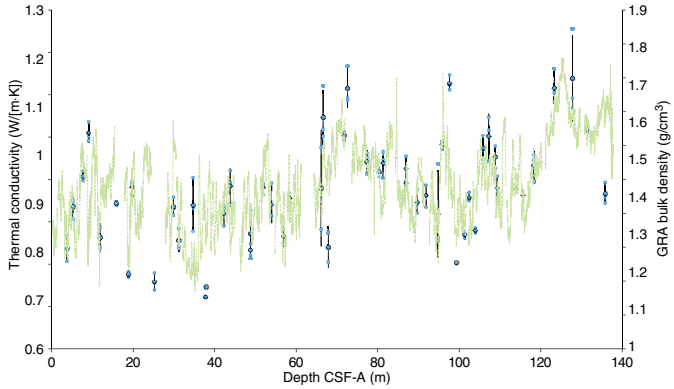

Downhole measurements

In situ temperature and heat flow

We carried out four downhole formation temperature measurements in Hole U1541B using the APCT-3 tool (Table **T13**). The calculated in situ formation temperatures increase with depth from 2.51°C at 35.6 m CSF-A to 4.37°C at 138.0 m CSF-A (Figure **F52**). The scatter is relatively small; however, the number of measure-

Table T13. Results from advanced piston corer temperature (APCT-3) tool profiles, Site U1541. **Download table in CSV format.**

Figure F52. Advanced piston corer temperature (APCT-3) tool plots of heat flow calculations, Hole U1541B. A. Thermal resistance calculated from heat conductivity measurements against core depth (m CSF-A). B. Downhole needle-point thermal conductivity measurements. Solid diamonds = mean values with standard error, circles = individual measurements. C. In situ sediment temperatures from APCT-3 measurements with average values for Cores 4H, 7H, 11H and 15H (diamonds) and linear fit (stippled line). D. Bullard plot of heat flow calculated from a linear fit of temperature vs. thermal resistance data.

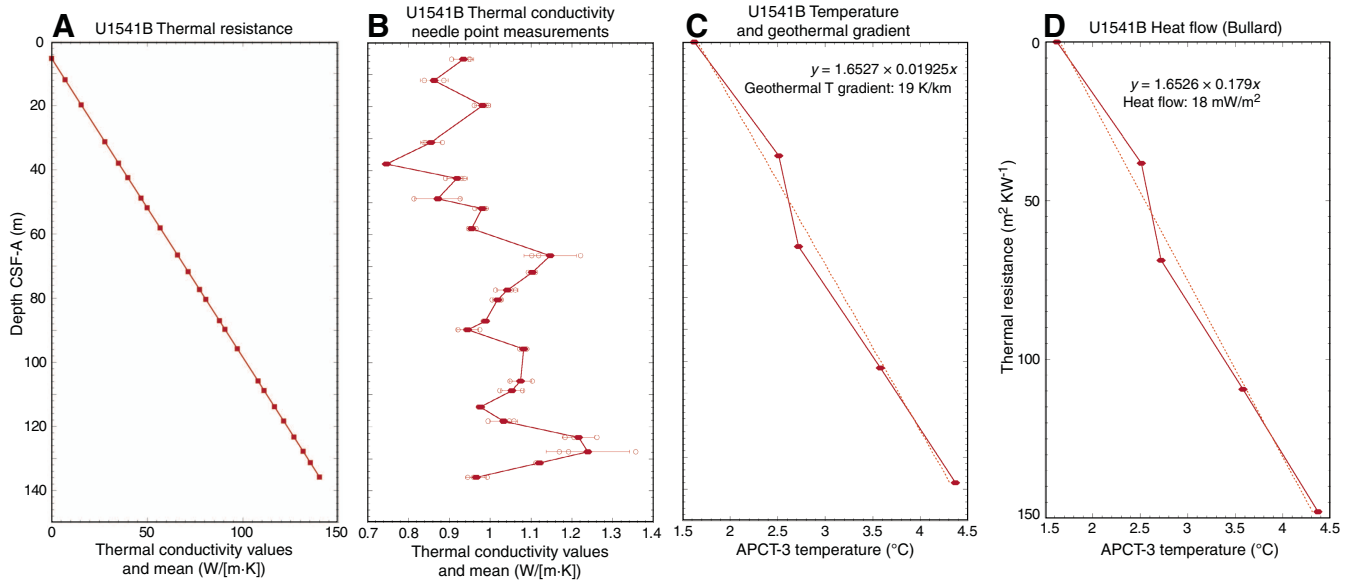

ments carried out was smaller than planned due to the need to optimize drilling time ahead of deteriorating weather conditions. Average bottom water temperature was calculated as 1.624°C, and the recorded minima were 1.588°C (Table **T13**), measured as the APCT-3 core cutting shoe was placed at the mudline for ~5 min. The mud pumps were then switched off before lowering the tool to target depth. Thus, temperature values represent the average of the means of the four APCT-3 time series at mudline level and should be regarded as approximations of true bottom water temperature. True bottom water temperature values are about 0.5°C higher than at the previous Sites U1539 and U1540 and consistently slightly warmer by about 0.5°C than the bottom water temperature measured with a conductivity-temperature-depth rosette system during Cruise PS75 at locations nearby to the drilled sites. The temperatures remain broadly within the expected temperature range based on World Ocean Atlas 2009 data from the location of Site U1541 (Gersonde, 2011; Locarnini et al., 2010).

Thermal conductivity under in situ conditions was estimated from laboratory-determined thermal conductivity using established methods (Pribnow et al., 2000; Hyndman et al., 1974) (see **Physical properties** in the Expedition 383 methods chapter [Winckler et al., 2021a]). Thermal resistance was calculated by cumulatively adding the inverse of the in situ thermal conductivity values over depth intervals downhole (Figure **F52**). A calculated heat flow of 18 mW/m^2 for Hole U1541B was obtained from the slope of the linear fit of in situ temperature and thermal resistance (Figure **F52**; cf. Pribnow et al., 2000). These values from Site U1541 west of the EPR are comparable to results calculated for Site U1540 (11–19 mW/m^2) from a similar water depth east of the EPR and only nominally higher than the values for Site U1539 (11–14 mW/m^2) from around 600 m deeper. These values indicate a fairly uniform subsurface crustal and sedimentary environment. Comparable low values between 10 and 50 mW/m^2 were observed in previous studies (Hensen et al., 2019), although heat flow data density in the subpolar South Pacific south of 40°S is among the lowest for any oceanic region globally and exhibits high lateral gradients, implying a potential for laterally heterogeneous fluid flow and hydrothermal systems along and within the transform fault zone system near our sites (Hensen et al., 2019).

The geothermal gradient (gT) for Site U1541 is estimated at ~18 K/km within the total measured depth interval based on a linear fit of temperature versus depth. Reported results were calculated based on a mean thermal conductivity of 0.93 W/(m·K), a core water depth of 3614 m, a sediment density of 1.80 g/cm, a bottom water temperature of 1.62°C, and a laboratory temperature of 18°C. Calculations for heat flow, resistivity, and geothermal gradient were checked for potential bias due to varying assumptions about the bottom water temperature, but reported results remain the same for various assumptions of bottom water temperature changes within a degree Celsius or less.

Stratigraphic correlation

Correlations between holes at Site U1541 were accomplished using Correlator software (version 3.0). Tie points were established mostly using the blue channel extracted from the SHMSL data (RGB blue) (Figure **F53**), but in many cases a combination of measurements was used (Table **T14**). We constructed a splice from 0 to 127.254 m CCSF-A using Holes U1541A–U1541C (Table **T15**; Figures **F53**, **F54**, **F55**); however, because some cores were disturbed or short and could not be used, the splice contains two gaps (Figure **F53**), as detailed below. Because Hole U1541B was drilled deeper than the other holes, the last two cores in Hole U1541B were appended to the bottom of the splice.

The CCSF-A scale is anchored to the mudline of Core 383-U1541C-1H, which is assigned the depth of 0 m CCSF-A. From this

Figure F53. Red-green-blue (RGB) blue data vs. composite depth in 50 m intervals, Holes U1541A–U1541C. Top: red-green-blue (RGB) blue splice constructed by combining data from all holes.

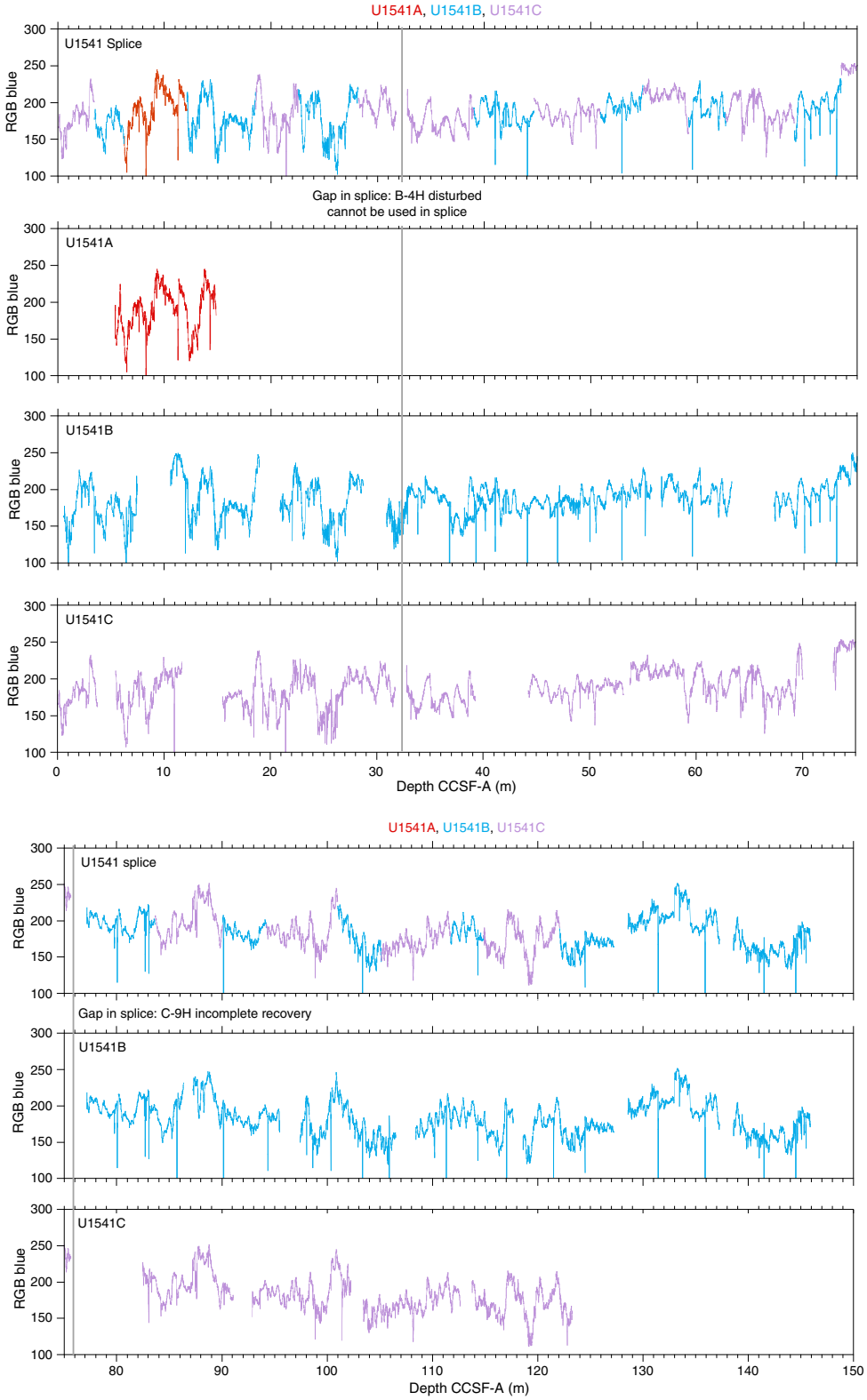

Table T14. Affine table, Site U1541. RGB = red, green, blue, MS = magnetic susceptibility, WRMSL = Whole-Round Multisensor Logger. **Download table in CSV format.**

Core	Depth CSF-A (m)	Depth CCSF-A (m)	Offset (m)	CCSF of TIE point used to determine offset (m)	Type of shift	Data used	Reference core
383-U1541A-							
1H	0	5.348	5.348	6.216	TIED to	RGB blue	U1541B-1H
383-U1541B-							
1H	0	0.49	0.49	3.427	TIED to	RGB blue	U1541C-1H
2H	7.1	10.545	3.445	12.13	TIED to	RGB blue	U1541A-1H
3H	16.6	20.825	4.225	22.563	TIED to	RGB blue	U1541C-3H
4H	26.1	30.825	4.725		SET to affine of Core 3H + 0.5 m		
5H	35.6	38.101	2.501	39.013	TIED to	RGB blue	U1541C-5H
6H	45.1	46.961	1.861	50.883	TIED to	MS WRMSL	U1541C-6H
7H	54.6	56.571	1.971	59.175	TIED to	RGB blue	U1541C-7H
8H	64.1	67.124	3.024	69.104	TIED to	RGB blue	U1541C-8H
9H	73.6	77.124	3.524		SET to affine of Core 8H + 0.5 m		
10H	83.1	87.206	4.106	90.055	TIED to	RGB blue	U1541C-10H
11H	92.6	97.406	4.806	101.006	TIED to	RGB blue	U1541C-11H
12H	102.1	108.367	6.267	111.705	TIED to	RGB blue	U1541C-12H
13H	111.6	118.554	6.954	122.075	TIED to	RGB blue	U1541C-13H
14H	121.1	128.554	7.454		SET to affine of Core 13H + 0.5 m		
15H	130.6	138.554	7.954		SET to affine of Core 14H + 0.5 m		
16X	138	144.253	8.454		SET to affine of Core 15X + 0.5 m		
383-U1541C-							
1H	0	0	0	18.568			Mudline
2H	4.1	5.432	1.332	6.216	TIED to	RGB blue	U1541B-1H
3H	13.6	15.478	1.878	18.568	TIED to	RGB blue	U1541B-2H
4H	23.1	22.751	–0.349	28.205	TIED to	RGB blue	U1541B-3H
5H	32.6	32.751	0.151		SET to affine of Core 4H + 0.5 m		
6H	42.1	44.194	2.094	44.685	TIED to	RGB blue	U1541B-5H
7H	51.6	53.783	2.183	54.896	TIED to	RGB blue	U1541B-6H
8H	61.1	61.094	–0.006	62.661	TIED to	RGB blue	U1541B-7H
9H	70.6	72.886	2.286	73.5	TIED to	MS WRMSL	U1541B-8H
10H	80.1	82.478	2.378	83.638	TIED to	RGB blue	U1541B-9H
11H	89.6	92.872	3.272	94.216	TIED to	RGB blue	U1541B-10H
12H	99.1	103.432	4.332	105.133	TIED to	RGB blue	U1541B-11H
13H	108.6	113.753	5.153	114.843	TIED to	RGB blue	U1541B-12H

anchor, we worked downhole using Correlator to establish a composite stratigraphy on a core-by-core basis. Interstitial water sampling and shipboard measurement sampling were done on Cores 383-U1541A-1H; 383-U1541B-1H, 2H, and 4H–15H; and 383-U1541C-2H through 4H. Thus, our general approach was to avoid using material from these cores. However, because of poor recovery or coring disturbance in a few intervals, we had to piece together the splice using all three holes, sometimes using cores that had been used for shipboard sampling. We mainly used Hole U1541C as the backbone of the splice and filled gaps between cores and avoided any disturbed intervals by including cores from Holes U1541A and U1541B in the splice. Finally, we adjusted splice tie points to avoid intersection with paleomagnetic reversals so that reversals occur within splice intervals.

The upper portion of the splice is continuous with no gaps from 0 to 31.78 m CCSF-A. At that depth, because Core 383-U1541B-4H was highly disturbed, it was not used in the splice; instead, Core 383-U1541C-5H was appended to the splice by setting the affine offset using an offset consistent with an increasing cumulative affine offset of 0.5 m CCSF-A per core. Below this first gap, the splice is continuous from 32.75 m CCSF-A to the bottom of Core 383-U1541C-9H at 75.67 m CCSF-A. At that depth, because Core 383-U1541C-9H was short (only 3.02 m recovered), it was clear that it did not cover the entire gap between Cores 383-U1541B-8H and 9H, and we had to append Core 383-U1541B-9H to the bottom of Core 383-U1541C-9H by setting the affine offset using an offset consistent with an increasing cumulative affine offset of 0.5 m CCSF-A per core. Below 77.12 m CCSF-A, the splice is continuous to 127.25 CCSF-A, which is the bottom of Core 383-U1541B-13H. At that depth, because drilling at Hole U1541C was terminated due to weather, Cores 383-U1541B-14H and 15H were appended to the splice using an increasing cumulative offset of 0.5 m CCSF-A per core.

The cumulative offset between the CSF-A and CCSF-A depth scales is nearly linear for Holes U1541B and U1541C (Figure **F56A**). The growth factor averages 8.6% but varies from 0% to 49% because of ship heave and misfired APC cores. The average growth factor of 8.6% is consistent with what is expected for sediments that expand because of release of overburden but have minimal gas expansion due to low concentrations of methane and other gases (see **Geochemistry**). There are small changes in the growth factor, and therefore in the cumulative offset with depth (Figure **F56B**), because of core disturbance due to bad weather conditions and misfired APC coring in a few instances, particularly in the upper 80 m. The CSF-A depth for the top of each core is set to the drilling depth below seafloor (DSF), which is based on the position of the drill string below the seafloor. However, the process of correlation moved each core top depth to a position on the CCSF-A scale that may not represent variable sediment compaction and expansion. Calculation of mass accumulation rates based on the CCSF-A scale should account for differential expansion by dividing apparent depth intervals by the appropriate growth factor.

Table T15. Splice interval table, Site U1541. RGB = red, green, blue, MS = magnetic susceptibility, WRMSL = Whole-Round Multisensor Logger. **Download table in CSV format.**

	Top of splice interval				Bottom of splice interval					
Hole	Core, section	Offset (cm)	Depth CSF-A (m)	Depth CCSF-A (m)	Core, section	Offset (cm)	Depth CSF-A (m)	Depth CCSF-A (m)	Splice type	Data used
U1541C	1H-1	0	0	0	1H-3	43.7	3.427	3.427	TIE	RGB blue
U1541B	1H-2	144.7	2.937	3.427	1H-4	124.6	5.726	6.216	TIE	RGB blue
U1541A	1H-1	86.8	0.868	6.216	1H-5	80.2	6.782	12.13	TIE	RGB blue
U1541B	2H-2	9.5	8.685	12.13	2H-7	20.3	15.123	18.568	TIE	RGB blue
U1541C	3H-3	8	16.69	18.568	3H-5	107.5	20.685	22.563	TIE	RGB blue
U1541B	3H-2	52.8	18.338	22.563	3H-6	99	23.98	28.205	TIE	RGB blue
U1541C	4H-4	93.4	28.554	28.205	4H-6	151	32.13	31.781	APPEND	RGB blue
U1541C	5H-1	0	32.6	32.751	5H-5	65.2	38.862	39.013	TIE	RGB blue
U1541B	5H-1	91.2	36.512	39.013	5H-5	57.4	42.184	44.685	TIE	RGB blue
U1541C	6H-1	49.1	42.591	44.685	6H-5	66.9	48.789	50.883	TIE	MS WRMSL
U1541B	6H-3	91.2	49.022	50.883	6H-6	41.5	53.035	54.896	TIE	RGB blue
U1541C	7H-1	111.3	52.713	54.896	7H-4	89.2	56.992	59.175	TIE	RGB blue
U1541B	7H-2	109.4	57.204	59.175	7H-5	74	60.69	62.661	TIE	RGB blue
U1541C	8H-2	6.7	62.667	62.661	8H-6	49	69.11	69.104	TIE	RGB blue
U1541B	8H-2	48	66.08	69.104	8H-5	37.6	70.476	73.5	TIE	MS WRMSL
U1541C	9H-1	61.4	71.214	73.5	9H-2	128	73.38	75.666	APPEND	RGB blue
U1541B	9H-1	0	73.6	77.124	9H-5	50.4	80.114	83.638	TIE	RGB blue
U1541C	10H-2	34	81.26	83.638	10H-6	134.7	87.677	90.055	TIE	RGB blue
U1541B	10H-2	134.9	85.949	90.055	10H-5	109	90.11	94.216	TIE	RGB blue
U1541C	11H-1	134.4	90.944	94.216	11H-6	64.4	97.734	101.006	TIE	RGB blue
U1541B	11H-3	60	96.2	101.006	11H-6	21.7	100.327	105.133	TIE	RGB blue
U1541C	12H-2	19.1	100.801	105.133	12H-6	72.3	107.373	111.705	TIE	RGB blue
U1541B	12H-3	33.8	105.438	111.705	12H-5	46.6	108.576	114.843	TIE	RGB blue
U1541C	13H-1	109	109.69	114.843	13H-6	74.2	116.922	122.075	TIE	RGB blue
U1541B	13H-3	50.1	115.121	122.075	13H-6	120	120.3	127.254	APPEND	RGB blue
U1541B	14H-1	0	121.1	128.554	14H-6	134	129.85	137.304	APPEND	RGB blue
U1541B	15H-1	0	130.6	138.554	15H-5	138	137.98	145.934		

Figure F54. Spliced composite records of red-green-blue (RGB) blue, Whole-Round Multisensor Logger gamma ray attenuation (GRA) and magnetic susceptibility (MS), and natural gamma radiation (NGR) vs. composite depth in 50 m intervals, Site U1541. cps = counts per second. (Continued on next page.)

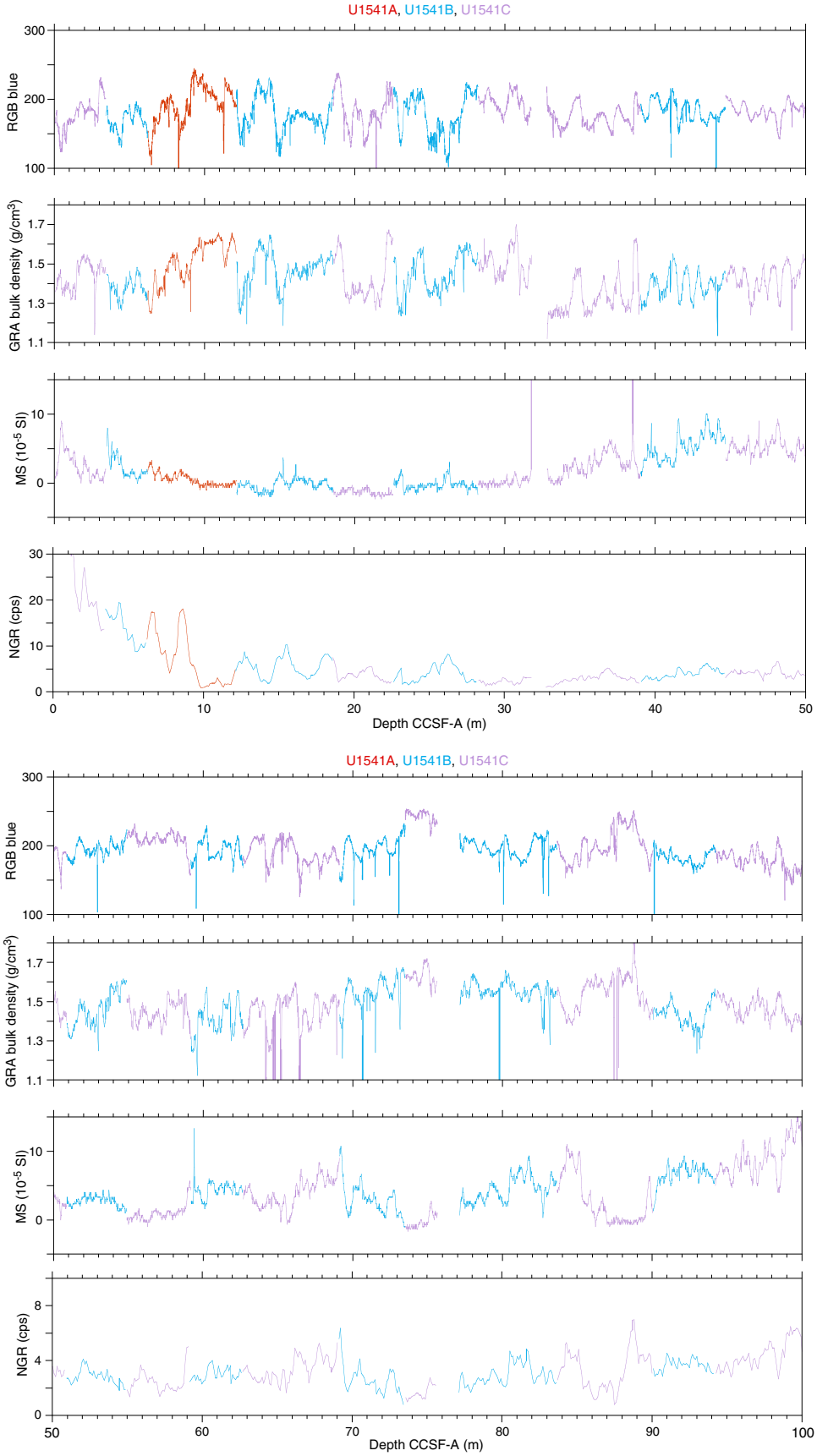

Figure F54 (continued).

Figure F55. Complete spliced composite records of cleaned red-green-blue (RGB) blue, cleaned Whole-Round Multisensor Logger gamma ray attenuation (GRA) and magnetic susceptibility (MS), and natural gamma radiation (NGR), Site U1541. cps = counts per second.

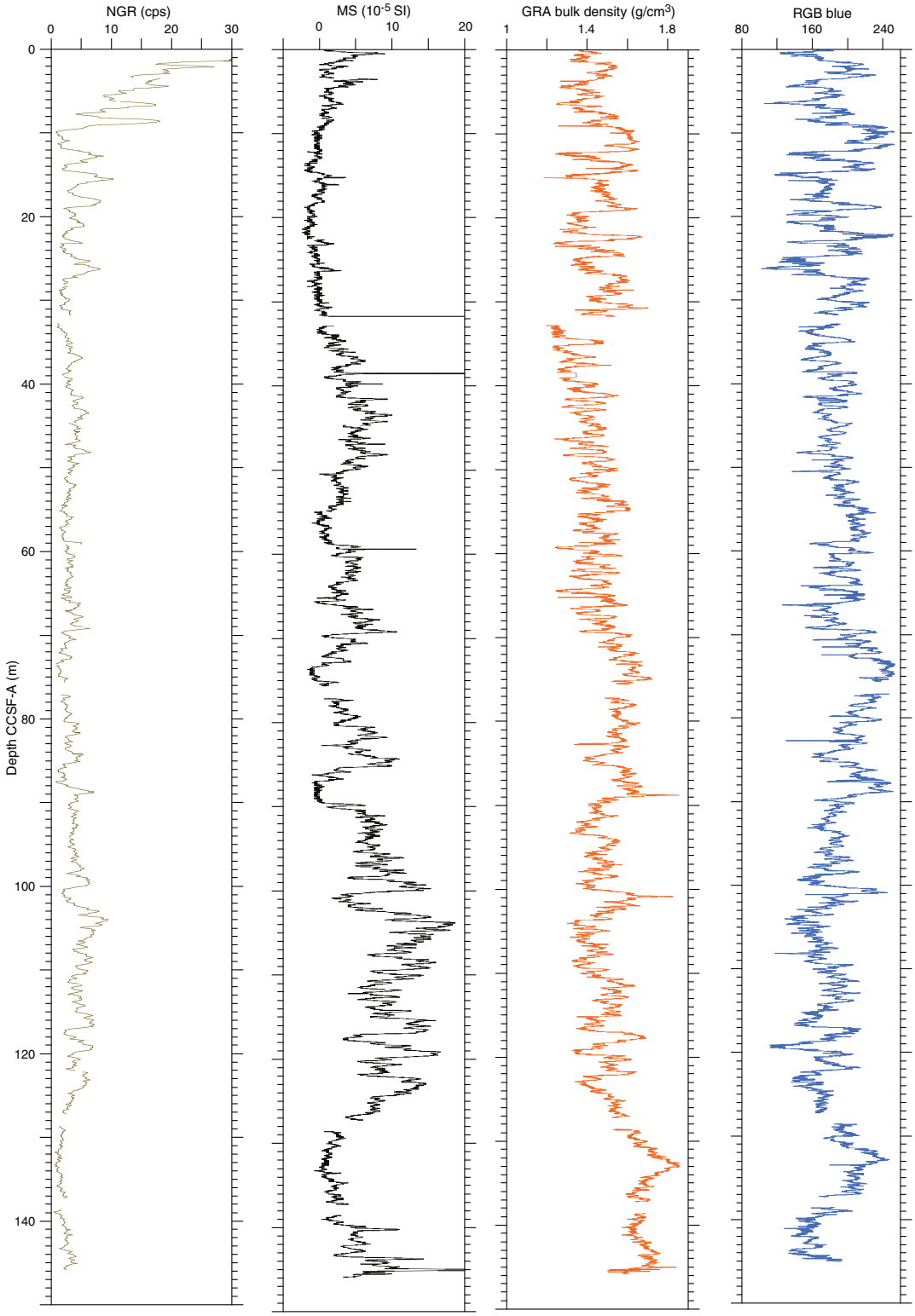

Figure F56. A. Comparison of core depth and composite depth scales in the Site U1541 splice. B. Comparison of the growth of cumulative depth offset and core depth.

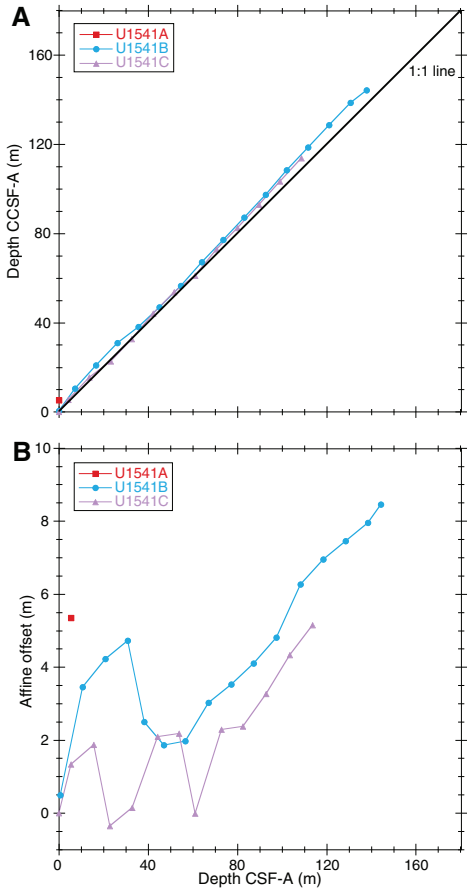

References

Alvarez Zarikian, C.A., Stepanova, A.Y., and Grützner, J., 2009. Glacial–interglacial variability in deep sea ostracod assemblage composition at IODP Site U1314 in the subpolar North Atlantic. *Marine Geology,* 258(1–4):69–87. **https://doi.org/10.1016/j.margeo.2008.11.009**

Alvarez Zarikian, C.A., 2015. Cenozoic bathyal and abyssal ostracods beneath the South Pacific Gyre (IODP Expedition 329 Sites U1367, U1368 and U1370). *Palaeogeography, Palaeoclimatology, Palaeoecology,* 419:115–142. **https://doi.org/10.1016/j.palaeo.2014.07.024**

Bremer, M.L., and Lohmann, G.P., 1982. Evidence for primary control of the distribution of certain Atlantic Ocean benthic foraminifera by degree of carbonate saturation. *Deep-Sea Research, Part A: Oceanographic Research Papers*, 29(8):987–998. **https://doi.org/10.1016/0198-0149(82)90022-X**

Bylinskaya, M.E., 2004. Range and stratigraphic significance of the *Globorotalia crassaformis plexus*. *Journal of Iberian Geology*, 31(1):51–63.

Calvert, S.E., and Pedersen, T.F., 1994. Sedimentary geochemistry of manganese; implications for the environment of formation of manganiferous black shales. *Economic Geology,* 91(1):36–47. **http://dx.doi.org/10.2113/gsecongeo.91.1.36**

Cande, S.C., and Kent, D.V., 1995. Revised calibration of the geomagnetic polarity timescale for the Late Cretaceous and Cenozoic. *Journal of Geophysical Research: Solid Earth,* 100(B4):6093–6095. **https://doi.org/10.1029/94JB03098**

Censarek, B., and Gersonde, R., 2002. Miocene diatom biostratigraphy at ODP Sites 689, 690, 1088, 1092 (Atlantic sector of the Southern Ocean). *Marine Micropaleontology,* 45(3–4):309–356. **https://doi.org/10.1016/S0377-8398(02)00034-8**

Chaisson, W.P., and Pearson, P.N., 1997. Planktonic foraminifer biostratigraphy at Site 925: middle Miocene–Pleistocene. *In* Shackleton, N.J., Curry, W.B., Richter, C., and Bralower, T.J. (Eds.), *Proceedings of the Ocean Drilling Program, Scientific Results,* 154: College Station, TX (Ocean Drilling Program), 3–31. **http://dx.doi.org/10.2973/odp.proc.sr.154.104.1997**

Ciesielski, P.F., 1975. Biostratigraphy and paleoecology of Neogene and Oligocene silicoflagellates from cores recovered during Antarctic Leg 28, Deep Sea Drilling Project. *In* Hayes, D.E., Frakes, L.A., et al., *Initial Reports of the Deep Sea Drilling Project,* 28: Washington, DC (U.S. Government Printing Office), 625–691. **https://doi.org/10.2973/dsdp.proc.28.117.1975**

Cody, R.D., Levy, R.H., Harwood, D.M., and Sadler, P.M., 2008. Thinking outside the zone: high-resolution quantitative diatom biochronology for the Antarctic Neogene. *Palaeogeography, Palaeoclimatology, Palaeoecology,* 260(1–2):92–121. **https://doi.org/10.1016/j.palaeo.2007.08.020**

Corliss, B.H., 1979. Quaternary Antarctic bottom-water history: deep sea benthonic foraminiferal evidence from the southeast Indian Ocean. *Quaternary Research,* 12(2):271–289. **https://doi.org/10.1016/0033-5894(79)90062-0**

Corliss, B.H., 1985. Microhabitats of benthic foraminifera within deep-sea sediments. *Nature,* 314(6010):435–438. **https://doi.org/10.1038/314435a0**

Das, M., Singh, R.K., Vats, N., Holbourn, A., Mishra, S., Farooq, S.H., and Pandey, D.K., 2018. Changes in the distribution of Uvigernidae species over the past 775 kyr: implications for the paleoceanographic evolution of the Japan Sea. *Palaeogeography, Palaeoclimatology, Palaeoecology*, 507:201–213. **https://doi.org/10.1016/j.palaeo.2018.07.019**

De Vleeschouwer, D., Dunlea, A.G., Auer, G., Anderson, C.H., Brumsack, H., de Loach, A., Gurnis, M., et al., 2017. Quantifying K, U, and Th contents of marine sediments using shipboard natural gamma radiation spectra measured on DV *JOIDES Resolution*. *Geochemistry, Geophysics, Geosystems,* 18(3):1053–1064. **https://doi.org/10.1002/2016GC006715**

Dunlea, A.G., Murray, R.W., Harris, R.N., Vasiliev, M.A., Evans, H., Spivack, A.J., and D'Hondt, S., 2013. Assessment and use of NGR instrumentation on the *JOIDES Resolution* to quantify U, Th, and K concentrations in marine sediment. *Scientific Drilling,* 15:57–63. **https://doi.org/10.2204/iodp.sd.15.05.2013**

Eagles, G., 2006. Deviations from an ideal thermal subsidence surface in the southern Pacific Ocean. *Terra Antarctica Reports,* 12:109–118.

Fontanier, C., Jorissen, F.J., Chaillou, G., Anschutz, P., Grémare, A., and Griveaud, C., 2005. Live foraminiferal faunas from a 2800 m deep lower canyon station from the Bay of Biscay: faunal response to focusing of refractory organic matter. *Deep-Sea Research, Part I: Oceanographic Research Papers*, 52(7):1189–1227. **https://doi.org/10.1016/j.dsr.2005.01.006**

Frenguelli, J., 1949. Diatomeas fósiles de los yacimientos chilenos de Tiltil y Mejillones. *Darwiniana*, 9(1):97–157. **https://www.jstor.org/stable/23211723**

Gage, J.D., and Tyler, P.A., 1991. *Deep-Sea Biology: A Natural History of Organisms at the Deep-Sea Floor.* Cambridge, UK (Cambridge University Press) **https://doi.org/10.1017/CBO9781139163637**

German, C.R., and Von Damm, K.L., 2003. Hydrothermal processes. *Treatise on Geochemistry*, 6:181–222. **https://doi.org/10.1016/B0-08-043751-6/06109-0**

Gersonde, R., 1990. Taxonomy and morphostructure of Neogene diatoms from the Southern Ocean, ODP Leg 113. *In* Barker, P.F., Kennett, J.P., et al., *Proceedings of the Ocean Drilling Program, Scientific Results,* 113: College Station, TX (Ocean Drilling Program), 791–802. **https://doi.org/10.2973/odp.proc.sr.113.128.1990**

Gersonde, R., 2011. The Expedition of the Research Vessel "*Polarstern*" to the Polar South Pacific Sea in 2009/2010 (ANT-XXVI/2 - BIPOMAC). *Berichte zur Polar und Meeresforschung,* 632. **http://epic.awi.de/29941/**

Gradstein, F.M., Ogg, J.G., Schmitz, M.D., and Ogg, G.M. (Eds.), 2012. *The Geological Time Scale 2012:* Amsterdam (Elsevier). **https://doi.org/10.1016/C2011-1-08249-8**

Gupta, A.K., Singh, R.K., and Verma, S., 2013. Deep-sea palaeoceanographic evolution of the eastern Indian Ocean during the late Oligocene–Pleistocene: species diversity trends in benthic foraminifera. *Current Science,* 104(7):904–910. **http://www.currentscience.ac.in/Volumes/104/07/0904.pdf**

Harwood, D.M., and Maruyama, T., 1992. Middle Eocene to Pleistocene diatom biostratigraphy of Southern Ocean sediments from the Kerguelen Plateau, Leg 120. *In* Wise, S.W., Jr., Schlich, R., et al., *Proceedings of the Ocean Drilling Program, Scientific Results,* 120: College Station, TX (Ocean Drilling Program), 683–733. **https://doi.org/10.2973/odp.proc.sr.120.160.1992**

Hensen, C., Duarte, J.C., Vannucchi, P., Mazzini, A., Lever, M.A., Terrinha, P., Géli, L., Henry, P., et al., 2019. Marine transform faults and fracture zones: a joint perspective integrating seismicity, fluid flow and life. *Frontiers in Earth Science*, 7:39. **https://doi.org/10.3389/feart.2019.00039**

Hilgen, F.J., Lourens, L.J., and Van Dam, J.A., 2012. The Neogene period. With contributions by A.G. Beu, A.F. Boyes, R.A. Cooper, W. Krijgsman, J.G. Ogg, W.E. Piller, and D.S. Wilson. *In* Gradstein, F.M., Ogg, J.G., Schmitz, M.D., and Ogg, G.M. (Eds.), *The Geologic Time Scale:* Oxford, United Kingdom (Elsevier), 923–978. **https://doi.org/10.1016/B978-0-444-59425-9.00029-9**

Hornibrook, N.d.B., 1981. *Globorotalia* (planktic Foraminiferida) in the late Pliocene and early Pleistocene of New Zealand. *New Zealand Journal of Geology and Geophysics,* 24(2):263–292. **https://doi.org/10.1080/00288306.1981.10422717**

Hornibrook, N.d.B., and Jenkins, D.G., 1994. DSDP 594, Chatham Rise, New Zealand—late Neogene planktonic foraminiferal biostratigraphy revisited. *Journal of Micropalaeontology,* 13(2):93–101. **https://doi.org/10.1144/jm.13.2.93**

Hyndman, R.D., Erickson, A.J., and Von Herzen, R.P., 1974. Geothermal measurements on DSDP Leg 26. *In* Davies, T.A., Luyendyk, B.P., et al., *Initial Reports of the Deep Sea Drilling Project,* 26: Washington, DC (U.S. Govt. Printing Office), 451–463. **https://doi.org/10.2973/dsdp.proc.26.113.1974**

Jacobel, A.W., McManus, J.F., Anderson, R.F., and Winckler, G., 2017. Repeated storage of respired carbon in the equatorial Pacific Ocean over the last three glacial cycles. *Nature Communications*, 8:1727. **https://doi.org/10.1038/s41467-017-01938-x**

Jenkins, D.G., 1993. Cenozoic southern mid- and high-latitude biostratigraphy and chronostratigraphy based on planktonic foraminifera. *In* Kennett, J.P., and Warnke, D.A. (Eds.), *The Antarctic Paleoenvironment: A Perspective on Global Change: Part Two.* Antarctic Research Series, 60:125–144. **https://agupubs.onlinelibrary.wiley.com/doi/abs/10.1002/9781118668061.ch7**

Jonkers, L., De Nooijer, L.J., Reichart, G.-J., Zahn, R., and Brummer, G.-J.A., 2012. Encrustation and trace element composition of *Neogloboquadrina dutertrei* assessed from single chamber analyses - implications for paleotemperature estimates. *Biogeosciences*, 9(11):4851–4860. **https://doi.org/10.5194/bg-9-4851-2012**

Jutzeler, M., White, J.D.L., Talling, P.J., McCanta, M., Morgan, S., Le Friant, A., and Ishizuka, O., 2014. Coring disturbances in IODP piston cores with implications for offshore record of volcanic events and the Missoula megafloods. *Geochemistry, Geophysics, Geosystems,* 15(9):3572–3590. **https://doi.org/10.1002/2014GC005447**

Kennett, J.P., and Srinivasan, M.S., 1983. *Neogene Planktonic Foraminifera: A Phylogenetic Atlas:* Stroudsburg, PA (Hutchinson Ross).

Lamy, F., Winckler, G., Alvarez Zarikian, C.A., and the Expedition 383 Scientists, 2021. Supplementary material, **https://doi.org/10.14379/iodp.proc.383supp.2021**. *Supplement to* Lamy, F., Winckler, G., Alvarez Zarikian, C.A., and the Expedition 383 Scientists, *Dynamics of the Pacific Antarctic Circumpolar Current.* Proceedings of the International Ocean Discovery Program, 383: College Station, TX (International Ocean Discovery Program). https://doi.org/10.14379/iodp.proc.383.2021

Locarnini, R.A., Mishonov, A.V., Antonov, J.I., Boyer, T.P., Garcia, H.E., Baranova, O.K., Zweng, M.M., and Johnson, D.R., 2010. World Ocean Atlas 2009 (Volume 1): Temperature. *In* Levitus, S. (Ed.), *NOAA Atlas NESDIS 68:* Washington, DC (U.S. Government Printing Office). **ftp://ftp.nodc.noaa.gov/pub/WOA09/DOC/woa09_vol1_text_figures.pdf**

Meyers, P.A., 1994. Preservation of elemental and isotopic source identification of sedimentary organic matter. *Chemical Geology,* 114(3–4):289–302. **https://doi.org/10.1016/0009-2541(94)90059-0**

Meyers, P.A., 1997. Organic geochemical proxies of paleoceanographic, paleolimnologic, and paleoclimatic processes. *Organic Geochemistry,* 27(5–6):213–250. **https://doi.org/10.1016/S0146-6380(97)00049-1**

Pitman, W.C., and Heirtzler, J.R., 1966. Magnetic anomalies over the Pacific-Antarctic Ridge. *Science,* 154(3753):1164–1171. **https://doi.org/10.1126/science.154.3753.1164**

Pribnow, D., Kinoshita, M., and Stein, C., 2000. *Thermal Data Collection and Heat Flow Recalculations for Ocean Drilling Program Legs 101–180:* Hanover, Germany (Institute for Joint Geoscientific Research, Institut für Geowissenschaftliche Gemeinschaftsaufgaben [GGA]). **http://www-odp.tamu.edu/publications/heatflow/ODPReprt.pdf**

Richter, C., Acton, G., Endris, C., and Radsted, M., 2007. *Technical Note 34: Handbook for Shipboard Paleomagnetists.* Ocean Drilling Program. **https://doi.org/10.2973/odp.tn.34.2007**

Riesselman, C.R., 2012. *Fragilariopsis tigris* sp. nov., a new late Pliocene Antarctic continental shelf diatom with biostratigraphic promise. *Micropaleontology*, 58(4):367–376. **https://www.jstor.org/stable/24413299**

Schönfeld, J., 2006. Taxonomy and distribution of the *Uvigerina peregrina plexus* in the tropical to northeastern Atlantic. *Journal of Foraminiferal Research*, 36(4):355–367. **https://doi.org/10.2113/gsjfr.36.4.355**

Schrader, H.-J., 1973. Cenozoic diatoms from the northeast Pacific, Leg 18. *In* Kulm, L.D., von Huene, R., et al., *Initial Reports of the Deep Sea Drilling Project*, 18: Washington, DC (U.S. Government Printing Office), 673–797. **https://doi.org/10.2973/dsdp.proc.18.117.1973**

Scott, G.H., Kennett, J.P., Wilson, K.J., and Hayward, B.W., 2007. *Globorotalia puncticulata*: population divergence, dispersal and extinction related to Pliocene–Quaternary water masses. *Marine Micropaleontology*, 62(4):235–253. **https://doi.org/10.1016/j.marmicro.2006.08.007**

Singh, R.K. and Gupta, A.K., 2004. Late Oligocene–Miocene paleoceanographic evolution of the southeastern Indian Ocean: evidence from deep-sea benthic foraminifera (ODP Site 757). *Marine Micropaleontology*, 51(1–2):153–170. **https://doi.org/10.1016/j.marmicro.2003.10.003**

Singh, R.K., and Gupta, A.K., 2010. Deep-sea benthic foraminiferal changes in the eastern Indian Ocean (ODP Hole 757B): their links to deep Indonesian (Pacific) flow and high latitude glaciation during the Neogene. *Episodes*, 33(2):74–82.

Singh, R.K., and Gupta, A.K., 2005. Systematic decline in benthic foraminiferal species diversity linked to productivity increases over the last 26 Ma in the Indian Ocean. *Journal of Foraminiferal Research,* 35(3):219–227. **http://dx.doi.org/10.2113/35.3.219**

Singh, R.K., Gupta, A.K., and Das M., 2012. Paleoceanographic significance of deep-sea benthic foraminiferal species diversity at southeastern Indian Ocean Hole 752A during the Neogene. *Palaeogeography, Palaeoclimatology, Palaeoecology*, 361–362:94–103. **https://doi.org/10.1016/j.palaeo.2012.08.008**

Soetaert, K., Hofmann, A.F., Middelburg, J.J., Meysman, F.J.R., and Greenwood, J., 2007. The effect of biogeochemical processes on pH. *Marine Chemistry,* 106(1–2):380–401. (Reprint) **http://dx.doi.org/10.1016/j.marchem.2007.06.008**

Steinhardt, J., de Nooijer, L.L., Brummer, G.-J., and Reichart, G.-J., 2015. Profiling planktonic foraminiferal crust formation. *Geochemistry, Geophysics, Geosystems*, 16(7):2409–2430. **https://doi.org/10.1002/2015GC005752**

Stepanova, A., and Lyle, M., 2014. Deep-sea ostracoda from the eastern equatorial Pacific (ODP Site 1238) over the last 460 ka. *Marine Micropaleontology*, 111:100–107. **https://doi.org/10.1016/j.marmicro.2014.06.003**

Suto, I., and Uramoto, G.-I., 2015. Data report: diatom biostratigraphy of IODP Site U1371 in the South Pacific Ocean. *In* D'Hondt, S., Inagaki, F., Alvarez Zarikian, C.A., and the Expedition 329 Scientists, *Proceedings of the Integrated Ocean Drilling Program*, 329: Tokyo (Integrated Ocean

Drilling Program Management International, Inc.). **https://doi.org/10.2204/iodp.proc.329.203.2015**

Tsutsui, H., Takahashi, K., Nishida, N., and Nishiwaki, S., 2009. Intraspecific morphological variation with biometry of *Distephanus speculum* (Silicoflagellata). *Marine Micropaleontology*, 72(3–4):239–250. **https://doi.org/10.1016/j.marmicro.2009.06.003**

Ullermann, J., Lamy, F., Ninnemann, U., Lembke-Jene, L., Gersonde, R., and Tiedemann, R., 2016. Pacific-Atlantic Circumpolar Deep Water coupling during the last 500 ka. *Paleoceanography and Paleoclimatology,* 31(6):639–650. **https://doi.org/10.1002/2016PA002932**

Verma, S., Gupta, A.K., and Singh, R.K., 2013. Variations in deep-sea benthic foraminifera at ODP Hole 756B, southeastern Indian Ocean: evidence for changes in deep ocean circulation. *Palaeogeography, Palaeoclimatology, Palaeoecology*, 376:172–183. **https://doi.org/10.1016/j.palaeo.2013.02.034**

Wade, B.S., Pearson, P.N., Berggren, W.A., and Pälike, H., 2011. Review and revision of Cenozoic tropical planktonic foraminiferal biostratigraphy and calibration to the geomagnetic polarity and astronomical time scale. *Earth-Science Reviews,* 104(1–3):111–142. **https://doi.org/10.1016/j.earscirev.2010.09.003**

Wei, K.-Y., 1994. Stratophenetic tracing of phylogeny using SIMCA pattern recognition technique: a case study of the late Neogene planktonic foraminifera *Globoconella* clade. *Paleobiology*, 20(1):52–65. **https://doi.org/10.1017/S0094837300011131**

Wetzel, A., and Uchman, A., 2012. Hemipelagic and pelagic basin plains. *In* Knaust, D., and Bromley, R.G. (Eds.), *Developments in Sedimentology* (Volume 64): *Trace Fossils as Indicators of Sedimentary Environments:* Amsterdam (Elsevier), 673–701. **https://doi.org/10.1016/B978-0-444-53813-0.00022-8**

Whatley, R.C., Downing, S.E., Kesler, K., and Harlow, C.J., 1986. The ostracod genus Poseidonamicus from the Cainozoic of D.S.D.P. sites in the S.W. Pacific. *Revista Española de Micropaleontology*, 18:387–400.

Winckler, G., Lamy, F., Alvarez Zarikian, C.A., Arz, H.W., Basak, C., Brombacher, A., Esper, O.M., Farmer, J.R., Gottschalk, J., Herbert, L.C., Iwasaki, S., Lawson, V.J., Lembke-Jene, L., Lo, L., Malinverno, E., Michel, E., Middleton, J.L., Moretti, S., Moy, C.M., Ravelo, A.C., Riesselman, C.R., Saavedra-Pellitero, M., Seo, I., Singh, R.K., Smith, R.A., Souza, A.L., Stoner, J.S., Venancio, I.M., Wan, S., Zhao, X., and Foucher McColl, N., 2021a. Expedition 383 methods. *In* Lamy, F., Winckler, G., Alvarez Zarikian, C.A., and the Expedition 383 Scientists, *Dynamics of the Pacific Antarctic Circumpolar Current.* Proceedings of the International Ocean Discovery Program, 383: College Station, TX (International Ocean Discovery Program). **https://doi.org/10.14379/iodp.proc.383.102.2021**

Winckler, G., Lamy, F., Alvarez Zarikian, C.A., Arz, H.W., Basak, C., Brombacher, A., Esper, O.M., Farmer, J.R., Gottschalk, J., Herbert, L.C., Iwasaki, S., Lawson, V.J., Lembke-Jene, L., Lo, L., Malinverno, E., Michel, E., Middleton, J.L., Moretti, S., Moy, C.M., Ravelo, A.C., Riesselman, C.R., Saavedra-Pellitero, M., Seo, I., Singh, R.K., Smith, R.A., Souza, A.L., Stoner, J.S., Venancio, I.M., Wan, S., Zhao, X., and Foucher McColl, N., 2021b. Site U1540. *In* Lamy, F., Winckler, G., Alvarez Zarikian, C.A., and the Expedition 383 Scientists, *Dynamics of the Pacific Antarctic Circumpolar Current.* Proceedings of the International Ocean Discovery Program, 383: College Station, TX (International Ocean Discovery Program). **https://doi.org/10.14379/iodp.proc.383.104.2021**

Yasuhara, M., Hunt, G., Okahashi, H., and Brandão, S.N., 2013. The '*Oxycythereis*' problem: taxonomy and paleobiogeography of deep-sea ostracod genera *Pennyella* and *Rugocythereis*. *Palaeontology*, 56(5):1045–1080. **https:/doi.org/10.1111/pala.12035**

Zielinski, U., and Gersonde, R., 2002. Plio–Pleistocene diatom biostratigraphy from ODP Leg 177, Atlantic sector of the Southern Ocean. *Marine Micropaleontology,* 45(3–4):225–268. **https://doi.org/10.1016/S0377-8398(02)00031-2**